The Pennsylvania State University

The Graduate School

Department of Chemistry

FUNDAMENTAL STUDIES OF MOLECULAR DEPTH PROFILING WITH TOF-SIMS AND CLUSTER IONS

A Dissertation in

Chemistry

by

Caiyan Lu

Submitted in Partial Fulfillment
of the Requirements
for the Degree of

Doctor of Philosophy

December 2010

The dissertation of Caiyan Lu was reviewed and approved* by the following:

Nicholas Winograd
Evan Pugh Professor of Chemistry.
Dissertation Advisor
Chair of Committee

Barbara Garrison
Shapiro Professor of Chemistry
Head of the Department of Chemistry

Christine Dolan Keating
Associate Professor of Chemistry

Qiming Zhang
Distinguished Professor of Electrical Engineering

*Signatures are on file in the Graduate School

ABSTRACT

Cluster ion beams opened up new capabilities for molecular depth profiling with time-of-flight secondary ion mass spectrometry (ToF-SIMS). The thesis work presented here is aimed at understanding the fundamentals of molecular depth profiling and improving the performance of ToF-SIMS with C_{60}^+ projectiles on 3-dimensional (3-D) characterization of organic and biological materials. Ionization effects in depth profiling of trehalose films are investigated to elucidate the influence of water and salt contents on the formation of molecular ions under C_{60}^+ bombardment. An Irganox standard obtained from NPL with delta layers is used to evaluate the reliability and reproducibility of depth profiling through organic samples. A new delta layer system constructed with lipids and fatty acids is formed via the Langmuir-Blodgett (LB) technique. This sample is used to optimize depth profiling parameters, such as, sample temperature, primary ion beam energy and incident angles, as well as, determine the depth resolution of biological molecules. The results indicate that the depth resolution is predominately influenced by ion beam induced mixing at the organic-organic interfaces and not an artifact of topography. Overall, the optimal experimental parameters for biological depth profiling and 3-D imaging are at cryogenic temperature with a low kinetic energy C_{60}^+ beam at a glancing angle. A different experimental strategy is tested on a ~400 nm LB multilayer thin film using both Au^+ and C_{60}^+ beams. Bombardment by Au^+ projectiles results in significant damage and extremely low sputter efficiency on the LB film. The following sputtering by a C_{60}^+ beam is able to remove the damage and recover the molecular ion signals.

TABLE OF CONTENTS

LIST OF FIGURES

LIST OF TABLES

ACKNOWLEDGEMENTS

I want to express my deeply-felt thanks to my thesis advisor, Professor Nicholas Winograd, for giving me the opportunities to work on such exciting and intellectually stimulating projects. I will always be thankful for his encouragement and inspiring guidance throughout my Ph.D. study. I would also like to thank my collaborator Professor Barbara Garrison for her thoughtful advice and support during these years. My appreciation also goes to other faculty members, Professor Christine Dolan Keating and Professor Qiming Zhang, for serving on my committee. I owe special thanks to Professor Andreas Wucher, for all the inspiring ideas and insightful discussions. His work ethic, excitement about science, and creative thinking influenced me so much.

I wish to thank the present and past members of the Winograd group, as they are wonderful people to work with. I appreciate their help and support over the years, especially Dr. Juan Cheng, Dr. Shawn Parry, Dr. Joseph Kozole, Dr. Zihua Zhu, Dr. Leiliang Zheng, Dr. David Willingham, Dr. Michael Kurczy, Dr. Alan Piwowar, Daniel Brenes, Dan Mao, Melissa Passarelli, Andrew Kucher, Lauren Jackson, Jordan Lerach, Jay Tarolli, and Kan Shen. Specially, I would like to thank our staff assistant Sabrina Glasgow for her kindly help in the past six years.

Lastly, I want to thank my parents, Xianying Li and Chuanyin Lu. Their tremendous support and unconditional love has been, and will always be, inspiring me. To them, I dedicate this thesis.

Chapter 1

Introduction

Time-of-flight secondary ion mass spectrometry (ToF-SIMS) is a powerful analytical technique for the characterization of solid materials. In the past several years, the development of cluster ion sources has improved the performance of SIMS analysis on organic materials in many ways, such as the observed reduction of chemical damage[1-4], enhanced sensitivity[5-6], increased secondary ion yield[5,7] and expanded mass range[6]. One of the most important properties of cluster ion sources is that sputter depth profiling has been found to be successful on many organic and biological thin films to provide in-depth molecular information, whereas this was not possible with atomic beams.[5,7-14] In addition, using cluster ToF-SIMS, three-dimensional (3-D) mass spectral imaging is becoming a promising method which can reveal the chemical distribution of the subsurface from biological cells and tissues. This thesis is focused on the fundamental aspects of molecular depth profiling and aims to understand the key factors influencing the quality of depth profiling and 3-D imaging. This introduction chapter will provide an overview of ToF-SIMS principles and applications, a brief summary of cluster ion sources and the concept of sputter depth profiling, as well as the instrument set-up and sample preparation process used in this thesis.

1.1 Overview of TOF-SIMS

The ionization process of SIMS distinguishes it from other mass spectrometry methods. Unlike electrospray ionization (ESI) mass spectrometry, which requires sample vaporization, SIMS uses direct desorption by ion bombardment to produce ions. An important advantage of SIMS is that no matrix is needed compared to matrix-assisted laser desorption ionization (MALDI), so solid materials are able to be analyzed without prior sample preparations. Therefore, SIMS has become a well-established surface analytical technique widely used in materials characterization.

In ToF-SIMS, an energetic primary ion beam is used to raster over the sample surface. The bombardment by primary ions causes various species to be emitted from the outer most layers, including positive ions, negative ions, electrons, clusters and neutrals. By applying a specific voltage to the sample, either positive or negative secondary ions can be extracted and then transferred to a field-free time-of-flight (ToF) analyzer. In the ToF, the ions are separated depending upon their mass-to-charge ratios. Eventually, the ions will impact at the detector, and the signals will be processed and collected as a mass spectrum. The efficiency of ion detection is quite high due to the high transmission of ions and parallel mass-detection capability of the ToF analyzer.[2]

Imaging with ToF-SIMS is performed by scanning a pulsed focused primary ion beam across the sample surface in a pixel-by-pixel pattern to acquire individual mass spectrum at each pixel. The mass spectra are then summed up by the software to produce a mass spectral image and the chemical distribution of the region of interest can be illustrated in imaging mode. In many cases, the lateral resolution can be achieved at

~100 nm range with a liquid metal ion gun (LMIG)[3]. This is a great advantage over MALDI imaging which has a lateral resolution in the range of tens of micrometers. Because of its surface sensitivity and submicrometer imaging capability, SIMS is one of the widely used techniques to characterize samples in diverse fields, such as semiconductors, polymers, organic thin films, and even single biological cells.[15-16]

However, there are two unfavorable intrinsic features with SIMS due to the destructive bombardment process using the traditional atomic ion sources. The first issue is the extensive fragmentation of intact molecules of interest during the ion-solid interaction. Since the energy of the primary ions is much higher than typical chemical bonds in the sample, the bombardment of the surface by atomic primary ions results in complicated mass spectra composed of atomic and molecular species in the low mass range.[17] ToF-SIMS biological imaging with Ga^+ and In^+ guns has suffered from the poor ionization efficiency of molecular ions and the lack of sufficient ion intensity to provide useful chemical information about biological molecules. The other disadvantage of using atomic ion sources is the chemical damage accumulation induced by the ion beam bombardment. In order to maintain the surface chemistry, a rule is generally followed that less than 1% of the top surface layer of atoms or molecules receives an ion impact.[18] Therefore, for a majority of organic materials the ion fluence has to be kept below 10^{12} ions/cm^2 which is generally accepted as the static limit.[19] Organic materials are usually analyzed in so-called static SIMS mode and molecular information is only attainable at the near surface region with this restraint.

In contrast, another mode of analysis, dynamic SIMS, utilizes high ion fluence of atomic ions to etch away inorganic materials continuously with rapid erosion rate and to

trace the elemental information underneath the surface, which is called depth profiling. This type of experiment has been widely used in the semiconductor industry. However, this method is not useful for biological and organic materials. Prior to the introduction of cluster ion sources, analysis with an ion fluence over static limit and sputter depth profiling of organic molecules had been deemed to be impossible because no molecular information could be preserved.

There have been several approaches to expand the capability of SIMS analysis for organic and biological samples. Without major instrument modification, the sensitivity can be enhanced by improving the ionization efficiency. It is well-known that SIMS has significant matrix effects, such as ionization enhancement or suppression caused by the matrix species. Under some circumstances, beneficial matrix effects can be employed to aid in the ionization of specific species.[18] Recently, it was reported that the usage of ionic liquids as SIMS matrices was able to improve the detection limit on large biological molecules without complicating mass spectra.[20] Since ions represent only a small portion of desorbed species in the SIMS process, another way to increase ionization efficiency is to use a laser beam to ionize the neutral molecules emitted after bombardment by projectiles, a process known as post ionization.[18,21-22] Another type of sample preparation method is microsectioning, such as cryosectionings or freeze fracture. They are utilized in the analysis of biological samples to acquire the molecular information inside cells and tissues.[23-27]

Many of the limitations of ToF-SIMS have been overcome with the introduction of cluster ion sources, such as SF_5^+, Bi_3^+ and C_{60}^+. Cluster ion sources are capable of providing more useful molecular information of organic and biological samples by

analyzing them in "as received" condition since they can produce higher sputter yield, simplified mass spectra over an extended mass range.[3] Most importantly, with the low chemical damage accumulation induced by cluster ion beams, subsurface analysis can be performed by switching between sputter cycles and analysis cycles. This makes molecular depth profiling and 3-D imaging feasible. Currently, a lot of research efforts are focused on the methodology development of dynamic imaging and fundamental studies of cluster ToF-SIMS. The current research progress will be discussed in the following sections.

1.2 Development of Cluster SIMS

SF_6^0 showed the potential of cluster ion sources about twenty years ago with increased ionization efficiency and decreased sample damage when compared to Cs^+ projectiles[1], although it was replaced by SF_5^+ afterward.[28] High sputter yield was achieved by SF_5^+ without a significant increase of damage cross section. However, its big beam spot-size (~20 μm) and short lifetime compromised its performance on SIMS imaging and it was not widely accepted by the SIMS community.[29] A substantial breakthrough occurred when two new types of cluster ion sources became commercially available. One is a gas ion source producing C_{60} ions and the other is an upgraded version of the LMIG forming an ion beam composed of metal clusters, such as Au_3^+ and Bi_3^+.[30-32]

In a C_{60} source, the gaseous C_{60} is generated by heating C_{60} powder over ~400 ^{0}C to form a vapor which is then bombarded with low energy electrons to produce C_{60} ions.

The resulting ions can be C_{60}^{+}, C_{60}^{2+}, or even C_{60}^{3+}. A wien filter is used to select a desired charge state based on the mass-to-charge ratio. The most commonly used C_{60} ion is C_{60}^{+}, which is able to be focused down to ~1 μm spot size with 20-40 keV kinetic energy. For cluster ion beams using liquid metal ion source (LMIS), a tip coated in a eutectic metal alloy is needed, such as AuGe for Au_n^{+} and Bi for Bi_n^{+}. Cluster metal ions are emitted by applying a strong static electric field to the heated tip. After electrostatic alignment, the mass-selected ions are focused to a bright cluster ion beam with a possible lateral resolution of less than 400 nm.[32] This new generation of cluster ion sources is more reliable and easy to operate. In the past several years, they've become the main stream in ToF-SIMS analysis of organic materials.

One of the advantages of cluster ion sources is the extended mass range. In the earlier studies with atomic primary projectiles, ions with m/z higher than 200 were rarely observed on most organic materials. For example, the analysis of phospholipid molecules containing a phosphocholine head group typically only produced ions at m/z 184 or less.[27] The application of ToF-SIMS imaging was therefore limited by the poor contrast for biological molecules in single cell images. Cluster ion sources opened new opportunities in biological imaging by ToF-SIMS. With Au_3^{+}, Bi_3^{+} and C_{60}^{+} beams, the useful yields of molecular ions from some materials can be improved by a few orders of magnitude, especially for high mass ions ($m/z \geq 500$). Additionally, the increased yields do not compromise the spatial resolution. A submicrometer lateral resolution is routine with these ion sources. These advantages make cluster ToF-SIMS a powerful tool to map the spatial distribution of biological molecules in biological tissues and single cells. Since neither tagging molecules nor a matrix is required, the interference from the sample

preparation is minimized and the native information of the biological process can be revealed. Among the various biological molecules, lipids are of particular interest in the research field of SIMS because they are involved in many biological processes and the masses of lipids fit the mass range of cluster SIMS analysis. So far, using cluster SIMS, distributions of various lipids have been spatially identified in muscle, brain, intestine, aorta, kidney and liver tissues by utilizing high mass ions, which were not accessible with Ga^+ or In^+ probe.[33-40] Lipids and vitamins are also identifiable in freeze-dried or freeze-fractured single cells. For example, ToF-SIMS with gold clusters has observed vitamin E's unique localization in neuronal membranes using the peak at m/z 430.[41]

Utilizing the spatial mass spectral information, ToF-SIMS imaging is a fast way to assay chemical arrays. A successful example is the characterization of solid-phase synthesized combinatorial libraries using C_{60}^+ projectiles.[6] The C_{60}^+ primary ion beam also appears to be more efficient at desorbing and ionizing molecules from soft polymer substrates with enhanced useful yields of molecular ions of peptides. ToF-SIMS has even demonstrated high performance in analyzing microelectrode and DNA arrays, providing a useful technique for highthroughput analysis.[42-43]

Cluster projectiles not only enhance the performance of ToF-SIMS on static analysis, but also expand the analysis of organic materials into another direction, molecular depth profiling and 3-D imaging.

1.3 Molecular Depth Profiling and 3-D Imaging

A few of the earliest examples of organic depth profiling was performed by Gillen *et al.* at the National Institute of Standards and Technology (NIST).[5] With an SF_5^+ fluence up to 1×10^{15} ions/cm^2, well beyond the static limit, researchers were able to observe the molecular ion signal of glutamate at m/z 148, which indicates SF_5^+ is superior to Ga^+ for molecular depth profiling.[5] Similar success was achieved on depth profiles of other polymer materials, including a 4-acetamidophenol-doped poly(lactic acid) film.[44] The polyester structure of the biodegradable polymers allows for the facile scission of main chain by cluster ions, making this type of polymer feasible to depth profile. They investigated the effects of projectile nuclearity on depth profiling of glutamate film using C_n^- (n = 1-10) primary ions produced from a modified cesium source.[8] The results demonstrated that the secondary ion yield of molecular ions can be significantly enhanced up to 800 times using larger clusters. As shown in Figure **1-1**,[45] it was observed that a well-resolved molecular depth profile can be obtained only when the number of atoms n is larger than 6.

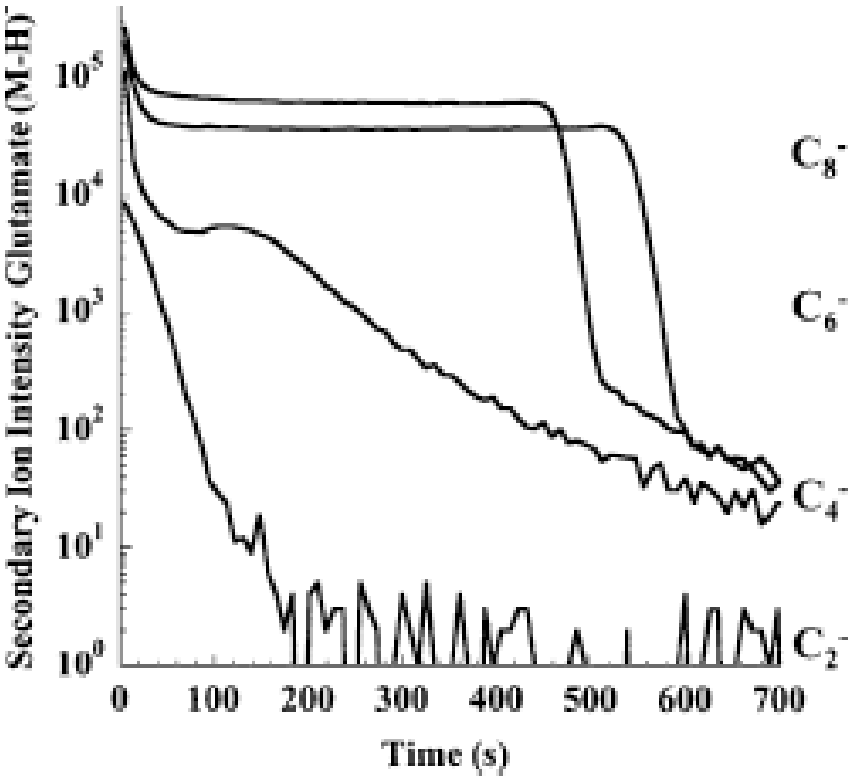

Figure **1-1**: Molecular ion signal $[M-H]^-$ at m/z 146 representing a glutamate film on silicon as a function of sputtering time using 3-keV C_n^- projectile ions.

C_{60}^+ has become the most commonly used cluster ion source for depth profiling after its debut in 2003[30], due to its user-friendliness and reliability. Most importantly, for most interested samples, it exhibits a larger enhancement of sputter yield compared to SF_5^+. Both experimental data and computer simulations have proven that the projectiles size has a critical influence on the desorption process of molecules from the surface. Molecular dynamics (MD) computer simulation is an effective approach to elucidate the interaction of primary ions on various solid surfaces at the atomic level. A MD simulation cross section view of Ga and C_{60} bombardment of a silver surface is shown in

Figure **1-2**, demonstrating the completely different nature of energy deposition process for atomic and cluster ions.[46] As shown in the left image, the 15-keV Ga projectile penetrates deeper into the silver crystal and induces a collision cascade of moving atoms along its movement. In contrast, due to the size effect, the C_{60} breaks apart upon the impact and most of carbon atoms are backscattered to the vacuum, leaving a mesoscale crater. A significant amount of the projectile's energy is deposited closer to the surface, resulting in efficient desorption of many particles with less damage and mixing at a deeper depth.

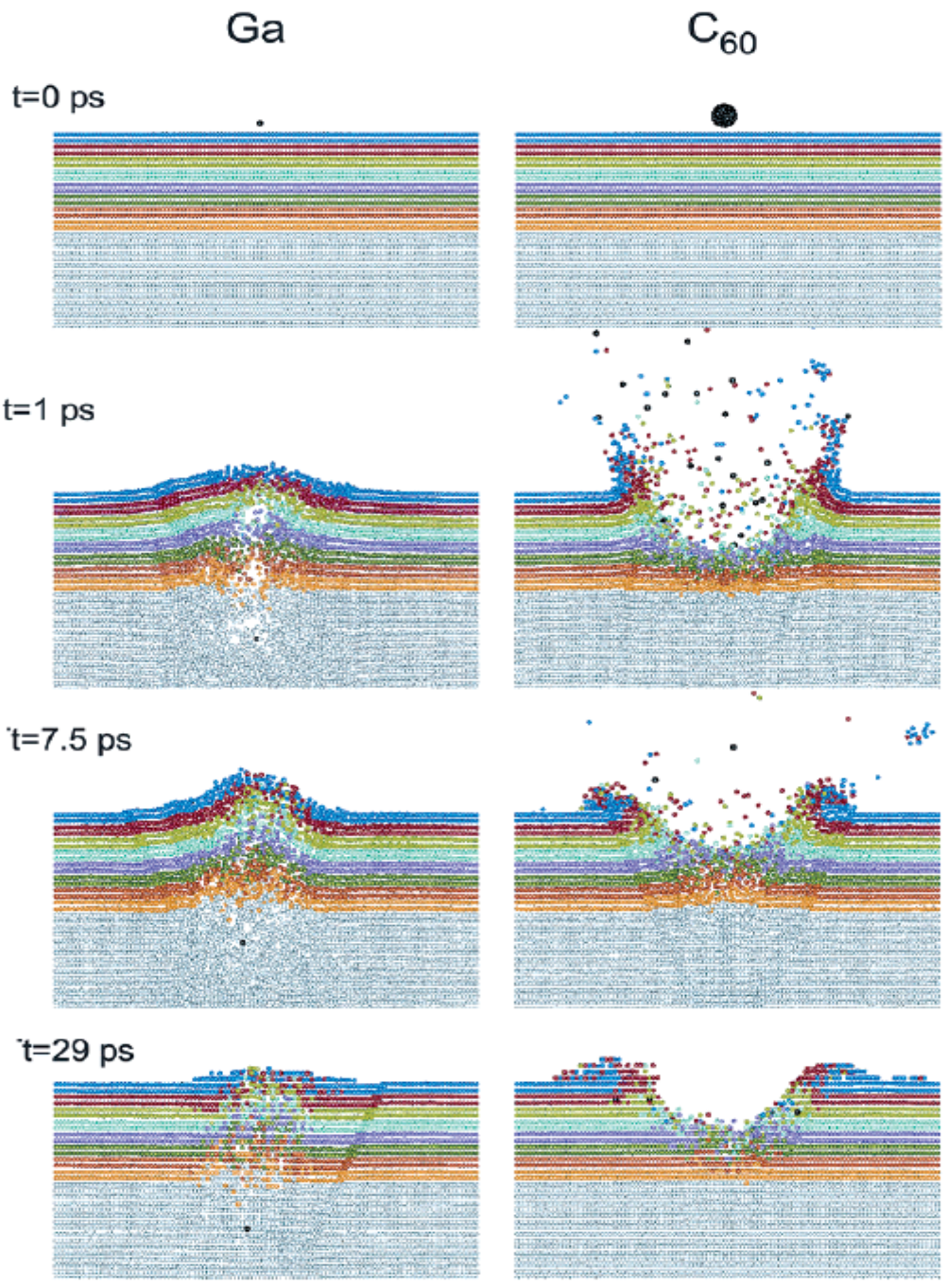

Figure **1-2**: Cross-section view of the temporal evolution of a typical collision event leading to the ejection of atoms due to 15-keV Ga and 15-keV C_{60} bombardment of a Ag surface at normal incidence. The dimensions of the solid are $10 \times 10 \times 10$ nm^3. The Ag atoms are colored by original layers in the solid. The projectiles are in black.

Molecular depth profiling has been studied on a wide range of biomolecules, polymers and organic thin films with C_{60}^+ cluster ions.[7,12-14,47] A successful example of a depth profile is presented in Figure **1-3,** which was obtained from a peptide doped trehalose film using a 20-keV C_{60}^+ beam.[7] The depth profile of the molecular ion consists of an initial exponential decay, a plateau at steady state and a fast signal decrease when reaching the substrate. The ion fluence can be converted to a depth scale by inspection of the crater with a stylus profilometer, an atomic force microscope (AFM), or an optical interferometer. An analytical erosion model has been created to describe the basic form of the molecular ion intensity as a function of ion fluence using characteristic parameters, including molecular sputtering yield, damage cross section, and the thickness of a surface layer altered by the projectiles.[4] The quality of depth profile can be quantitatively evaluated by the above parameters and cleanup efficiency.

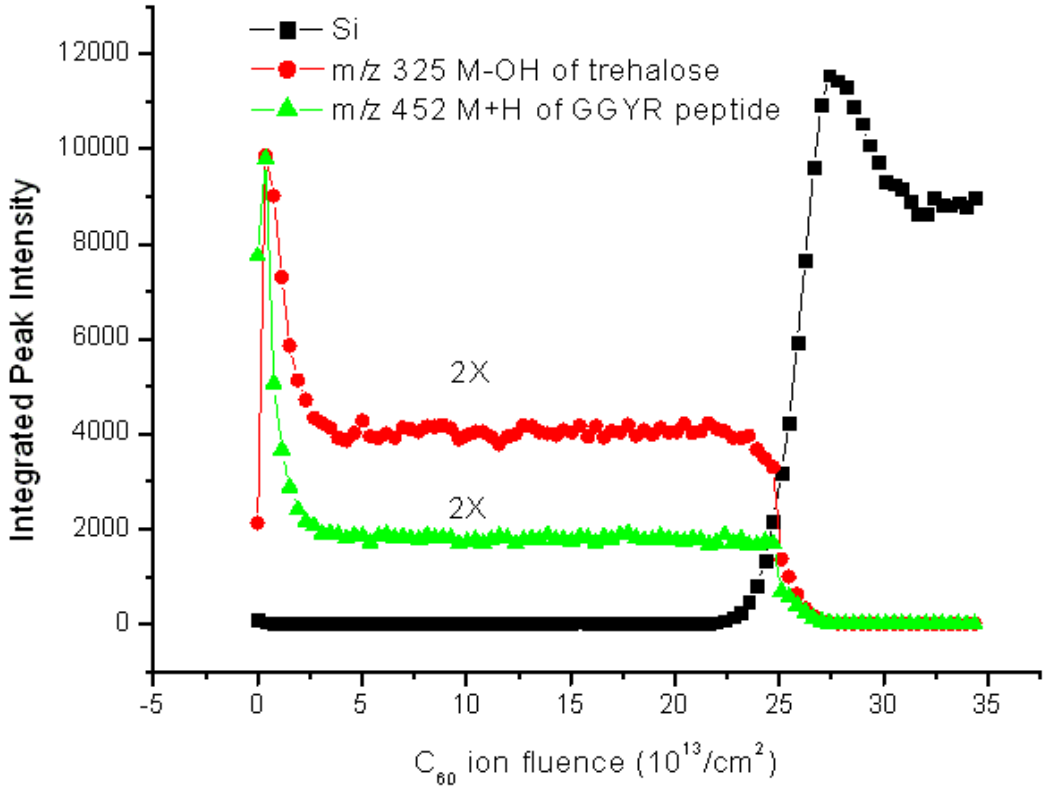

Figure **1-3**: Molecular depth profiles of peptide doped trehalose film prepared by spin coating.

Another key parameter of depth profiling is depth resolution. For a single component film, the apparent depth resolution is evaluated from the interface width by measuring the depth corresponding to 84%-16% of the maximum signal from the film or the substrate.[7] Delta layer is a negligibly thin layer embedded in a relatively thick matrix, which provides a direct measurement of the real depth resolution. It has been widely used as a reference material in the semiconductor industry. The National Physical Laboratory (NPL) in the UK constructed a widely useful organic delta layer system for quantitative analysis of C_{60}^+ depth profiles of organic materials.[14] The results from the

Irganox delta layer system indicate a degradation of depth resolution and a diminished signal intensity with the increasing C_{60}^+ fluence associated with topography build-up by ion beam sputtering.

Reported data illustrate that the experimental conditions affect the outcome of molecular depth profiling. Among commercially available projectiles, C_{60}^+ is reported to be the best choice among all the cluster projectiles.[48] Beam energy and impact angle of C_{60}^+ both play important roles controlling the energy deposition. Experimentally it has been determined that sputter yield increases linearly with beam energy,[14,49] while the best interface width and cleanup efficiency was found between 20-40 keV[49]. Studies of vapor deposited cholesterol films show that bombardment with 40-keV C_{60}^+ at a glancing angle produces the highest sputter yield, highest cleanup efficiency and best interface width, which agrees with the observations on alternating Langmuir Blodgett multilayer thin film.[50] In some cases, lowering the sample temperature helps to prevent the slow decay of molecular ion signal during sputtering in order to achieve the real steady state instead of quasi-steady state.[10,50] Sample rotation is a routine method to reduce the surface roughness in inorganic depth profiling, which has also been recently applied to molecular depth profiling of the Irganox delta layer sample by Sjovall *et al.*.[51] From their study, it was observed that rotating the Irganox sample at 14 Hz appears to be an effective way to maintain depth resolution and sputter yield.

Achievements in molecular depth profiling of model systems encourage the exploration of 3-D imaging on real biological systems. The idea of 3-D SIMS imaging is to utilize a pulsed beam to acquire a mass spectral image of the sample surface in a pixel-by-pixel fashion, followed by applying a DC beam to erode away several nanometers of

materials. Then, the image is taken again, characterizing the material at a deeper depth. By switching between the imaging mode and the sputter mode several times, a series of mass spectral images are obtained. 3-D rendering of the sputtered volume can be constructed if characteristic masses in each image can be correctly located at the corresponding depths. For a homogeneous sample with a uniform sputter rate, simply piling up the images sequentially from top to bottom will build a real 3-D image. However, mass spectral images obtained from real biological cells and tissues are not easy to compile into a 3-D imaging because of the differential sputter rate from the heterogeneous samples. Therefore, a more accurate depth calibration at each pixel is required. Currently, AFM is the most practical way to correct the depth scale. Wucher *et al.* established a protocol for 3-D imaging combining SIMS dynamic images with AFM images obtained on a heterogeneous model system.[52] In the future, the real-time crater measurement during depth profiling may be accomplished by optical techniques.[17] Among the attempts of 3-D imaging of single cells, some groups use a dual beam strategy, with C_{60}^+ as the sputter beam and Bi_3^+ as the analysis beam.[53] Bi_3^+ is able to provide high lateral resolution for small cells, however its inherent problem is that only low mass ions are available to identify biomolecules, such as m/z 184 and m/z 86 from a phosphocholine head group, which severely limits its usefulness. Fletcher *et al.* demonstrated the first 3-D image of single cells using a high lateral resolution C_{60}^+ source (~5 μm) as both the sputter source and the data acquisition source.[54] Mass spectral signals up to m/z 960 were used to characterize the 3-D distribution of membrane lipids. Interestingly, a number of etch craters were measured by AFM and the differential sputter rate appears to be inconsequential for the experiment.

1.4 Instruments and Methods

1.4.1 ToF-SIMS instrument

The ToF-SIMS used for the original data presented in this thesis is a home-built instrument, the details of which were described in previously published report.[55] The instrument has been continuously upgraded with state-of-the-art components since its inception. It is currently equipped with a 25-keV Au LMIS and a 40-keV C_{60} source, mounted on the analysis chamber at 45^0 and 40^0 incident angles, respectively. The majority of the work presented in this thesis was collected using the C_{60} ion gun. It has selectable apertures and the C_{60}^+ beam can be finely focused to 1 μm to enhance the imaging resolution. Depth profile experiments can be automatically operated by the software with customized settings, such as sputter size, data acquisition size, sputter time, number of sputter cycles, scanning mode, etc. Another feature of this instrument is the high performance sample cooling system. The sample stage and the transfer arm are able to be cooled to 100 K in a short time using liquid nitrogen as the coolant, which is specially suited for handling frozen biological samples.

1.4.2 AFM

A Nanopics 2100 AFM (KLA-Tencor, CA) was used to collect the topographical information for this thesis. It is a unique type of AFM which bridges the gap between a conventional AFM and a profiler. It has the same resolution as the conventional AFM in the z direction. However, its scanning area is able to be expanded up to 1000 μm^2, 20

times larger than the conventional AFM, fulfilling the needs of measuring sputtered craters. It has two operating modes: contact mode for robust materials or large scanning area, and tapping mode for soft materials or small scanning area. The characterization of craters was done in contact mode, and the evaluation of surface roughness was performed using tapping mode.

1.4.3 Preparation of Langmuir-Blodgett thin films

Langmuir-Blodgett (LB) films are formed by amphiphilic molecules at the air-water interface. Fatty acids and lipids all consist of a hydrophilic side and a hydrophobic side. These types of molecules will orient themselves at the air-water interface to minimize free energy, resulting in a monolayer film with the hydrophilic parts facing the water side and the hydrophobic parts towards the air side.

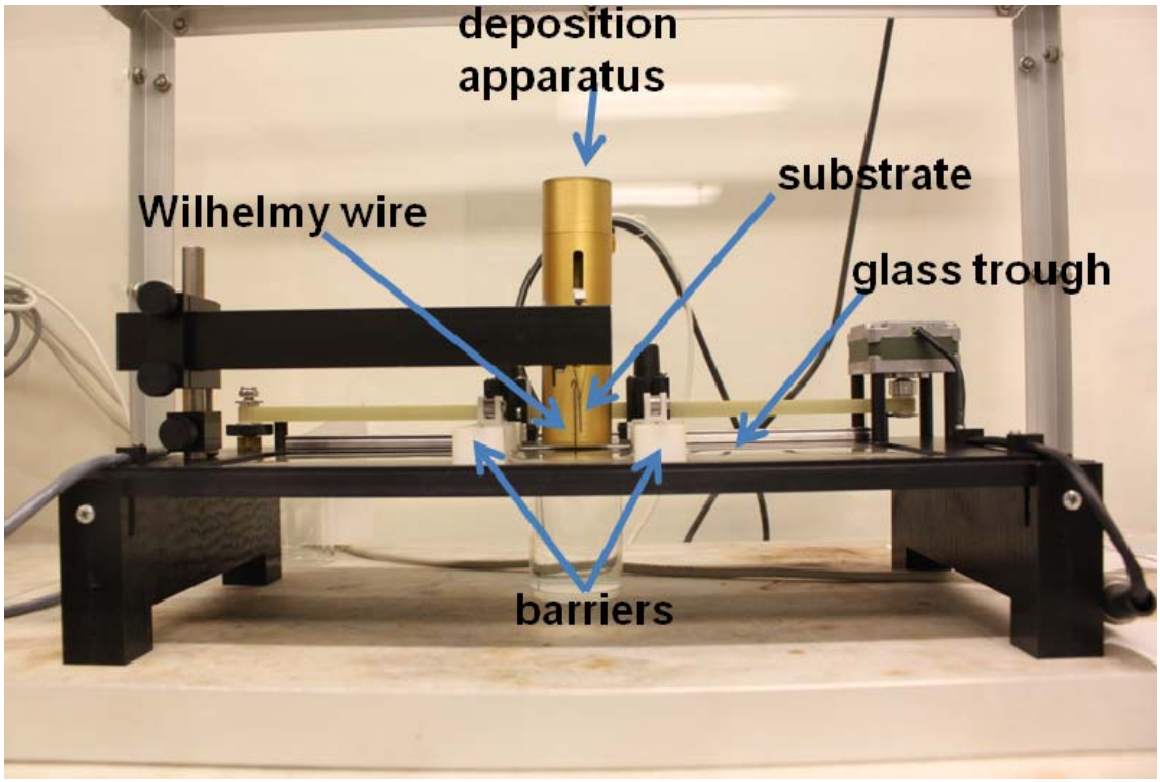

Figure **1-4**: Picture of a Kibron µTrough S-LB (Kibron, Helsinki, Finland) used for LB film preparation.

A Langmuir-Blodgett trough is required to prepare such monolayers. As shown in Figure **1-4,** a Kibron µTrough S-LB (Kibron, Helsinki, Finland) was used in this thesis work. The glass trough with Teflon edges holds 70 mL of the subphase (water or aqueous subphase). For sample manufacture, the lipids and fatty acids are first dissolved in a volatile water-insoluble solvent, such as chloroform, methanol, iso-propanol, hexane, or combinations of these solvents. To introduce the sample materials, a small of amount of the solution is applied on the subphase by a micro syringe, forming a monolayer at the air-water interface. After solvent evaporation, the monolayer is compressed by two Teflon barriers at a steady rate driven by a computer-controlled motor. During

compression, the surface pressure (mN/m) is monitored by a Wihelmy wire connected to the computer, providing a plot of surface pressure as a function of area per molecule. This plot is called a surface isotherm, and it indicates many of the important properties of the monolayer film formation. As the monolayer is compressed, the isotherm will pass through a few different regions, which depend upon the physical and chemical properties of the molecules, the subphase temperature, and the subphase composition. Figure **1-5** is an example of the isotherm for a fatty acid. At a large molecule area, the monolayer is in a highly disordered phase referred to as the gaseous phase (G). With increased compression, the gaseous phase transitions to the liquid state (L), which is less disordered than the gas phase. Under further compression the monolayer reaches a highly ordered state referred to as the solid state (S). At the solid state, an ordered monolayer can be deposited onto a solid substrate. By dipping in and pulling out the substrate through the air-water interface as demonstrated in Figure **1-6**, multiple layers can be sequentially deposited to form multilayer LB film.

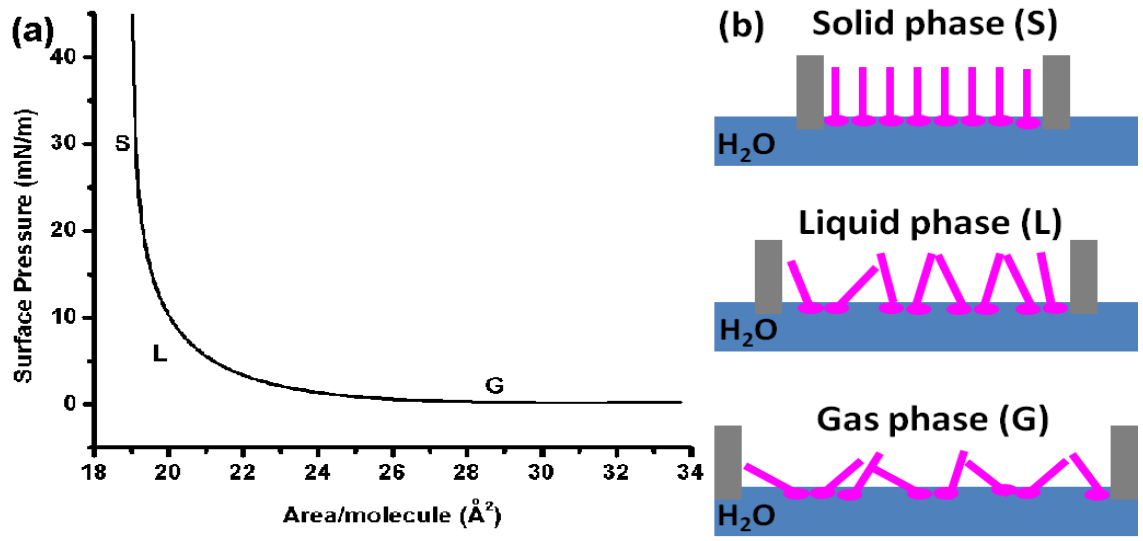

Figure **1-5**: (a) Schematic isotherm of fatty acid. (b) Orientation of fatty acid molecules at air-water interface.

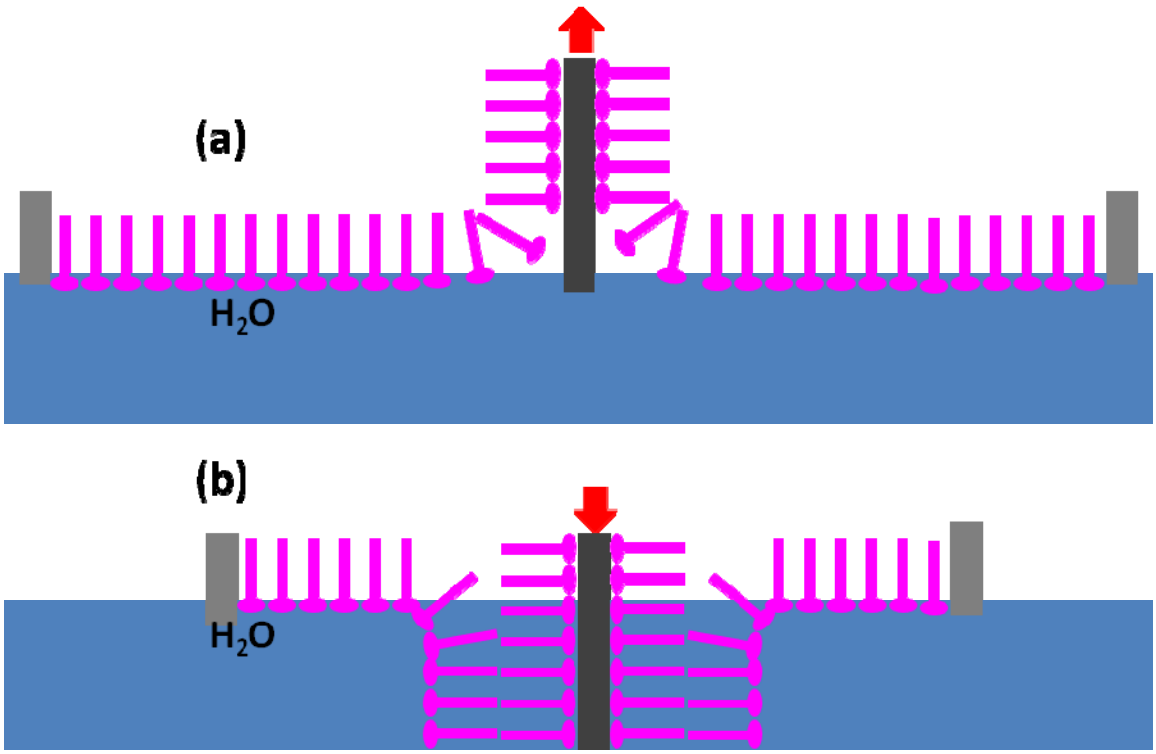

Figure **1-6**: Schematics of successive LB film deposition on solid substrate

The LB monolayer formation technique is a well-established and sophisticated method to control interfacial molecules orientation and packing. The LB films based on lipids and fatty acids closely mimic the structure of biological membranes and have been widely studied as cell membrane models. Information about lipid domain, lipid interaction and lipid/protein interactions can be obtained from high resolution SIMS images.[56-61] In previous studies, multilayer LB films were analyzed by depth profile experiments with a C_{60}^+ probe. Its alternating structure can be clearly characterized by the molecular ion signals, suggesting the feasibility of 3-D mass spectral imaging on the similar biological materials.[13,50,62]

1.5 Thesis Overview

The overall objective of this thesis is to investigate the fundamentals of molecular depth profiling and to maximize the performance of cluster ToF-SIMS for 3-D characterization of organic and biological materials.

Chapter 2 examines the ionization effects in molecular depth profiling using a trehalose film doped with peptide as a platform. The water content in the film affects the formation of $[M+H]^+$ ions due to the libration of protons from water molecules by C_{60}^+ bombardment. The presence of salt has a complicated influence on the formation of molecular ions, which could be either enhancement or supression on the ionization efficiency of molecular ions, depending upon the basicity of the molecules. An Irganox delta layer sample is studied in Chapter 3. The depth resolution of molecular depth profiling is quantitatively evaluated with a 40-keV C_{60}^+ beam. In Chapter 4 and 5, a new

model system of delta layer based on LB multilayer film is constructed and used to investigate the depth resolution of biological molecules. The results indicate that the depth resolution is mainly controlled by mixing at organic-organic interface, suggesting that depth profiling and 3-D imaging experiments should be carried at cryogenic temperature with a C_{60}^+ beam of low kinetic energy at a glancing angle in order to obtain the best results. In chapter 6, a different experimental strategy is tested on a ~400 nm LB multilayer thin film using Au^+ and C_{60}^+ beams. Bombardment by Au^+ projectiles results in significant damage and low sputter efficiency on the film, which could be attributed to the open structure of LB film. The following sputtering by a C_{60}^+ beam is able to remove the damage and recover the molecular ion signal. Finally, several future directions are discussed in Chapter 7, aimed to expand the applications of molecular depth profiling by ToF-SIMS with cluster ions.

1.6 References

(1) Appelhans, A. D.; Delmore, J. E. *Anal. Chem.* **1989**, *61*, 1087.

(2) Castner, D. G. *Nature* **2003**, *422*, 129.

(3) Winograd, N. *Anal. Chem.* **2005**, *77*, 142a.

(4) Cheng, J.; Wucher, A.; Winograd, N. *J. Phys. Chem. B* **2006**, *110*, 8329.

(5) Gillen, G.; Roberson, S. *Rapid Commun. Mass Spectrom.* **1998**, *12*, 1303.

(6) Xu, J. Y.; Szakal, C. W.; Martin, S. E.; Peterson, B. R.; Wucher, A.; Winograd, N. *J. Am. Chem. Soc.* **2004**, *126*, 3902.

(7) Cheng, J.; Winograd, N. *Anal. Chem.* **2005**, *77*, 3651.

(8) Gillen, G.; King, L.; Freibaum, B.; Lareau, R.; Bennett, J.; Chmara, F. *Journal of Vacuum Science & Technology a-Vacuum Surfaces and Films* **2001**, *19*, 568.

(9) Mahoney, C. M.; Roberson, S.; Gillen, G. *Appl. Surf. Sci.* **2004**, *231-2*, 174.

(10) Mahoney, C. M.; Fahey, A. J.; Gillen, G. *Anal. Chem.* **2007**, *79*, 828.

(11) Mahoney, C. M.; Fahey, A. J.; Gillen, G.; Xu, C.; Batteas, J. D. *Anal. Chem.* **2007**, *79*, 837.

(12) Kozole, J.; Wucher, A.; Winograd, N. *Anal. Chem.* **2008**, *80*, 5293.

(13) Zheng, L. L.; Wucher, A.; Winograd, N. *J. Am. Soc. Mass Spectrom.* **2008**, *19*, 96.

(14) Shard, A. G.; Green, F. M.; Brewer, P. J.; Seah, M. P.; Gilmore, I. S. *J. Phys. Chem. B* **2008**, *112*, 2596.

(15) Benninghoven, A. *Appl. Surf. Sci.* **2003**, *203*, 1.

(16) Walker, A. V. *Anal. Chem.* **2008**, *80*, 8865.

(17) Winograd, N.; Garrison, B. J. *Annual Review of Physical Chemistry, Vol 61* **2010**, *61*, 305.

(18) Vickerman, J. C.; Briggs, D. *ToF-SIMS: Surface Analysis by Mass Spectrometry*; IM Publication and Surface-Spectra Limited, 2001.

(19) Sichtermann, W.; Benninghoven, A. *Int. J. Mass Spectrom. Ion Processes* **1981**, *40*, 177.

(20) Fitzgerald, J. J. D.; Kunnath, P.; Walker, A. V. *Anal. Chem.* **2010**, *82*, 4413.

(21) Winograd, N. *Anal. Chem.* **1993**, *65*, A622.

(22) Wood, M.; Zhou, Y.; Brummel, C. L.; Winograd, N. *Anal. Chem.* **1994**, *66*, 2425.

(23) Colliver, T. L.; Brummel, C. L.; Pacholski, M. L.; Swanek, F. D.; Ewing, A. G.; Winograd, N. *Anal. Chem.* **1997**, *69*, 2225.

(24) Cannon, D. M.; Pacholski, M. L.; Winograd, N.; Ewing, A. G. *J. Am. Chem. Soc.* **2000**, *122*, 603.

(25) Roddy, T. P.; Cannon, D. M.; Ostrowski, S. G.; Winograd, N.; Ewing, A. G. *Anal. Chem.* **2002**, *74*, 4020.

(26) Roddy, T. P.; Cannon, D. M.; Meserole, C. A.; Winograd, N.; Ewing, A. G. *Anal. Chem.* **2002**, *74*, 4011.

(27) Ostrowski, S. G.; Van Bell, C. T.; Winograd, N.; Ewing, A. G. *Science* **2004**, *305*, 71.

(28) Kotter, F.; Benninghoven, A. *Appl. Surf. Sci.* **1998**, *133*, 47.

(29) Winograd, N.; Postawa, Z.; Cheng, J.; Szakal, C.; Kozole, J.; Garrison, B. J. *Appl. Surf. Sci.* **2006**, *252*, 6836.

(30) Wong, S. C. C.; Hill, R.; Blenkinsopp, P.; Lockyer, N. P.; Weibel, D. E.; Vickerman, J. C. *Appl. Surf. Sci.* **2003**, *203*, 219.

(31) Davies, N.; Weibel, D. E.; Blenkinsopp, P.; Lockyer, N.; Hill, R.; Vickerman, J. C. *Appl. Surf. Sci.* **2003**, *203*, 223.

(32) Touboul, D.; Kollmer, F.; Niehuis, E.; Brunelle, A.; Laprevote, O. *J. Am. Soc. Mass Spectrom.* **2005**, *16*, 1608.

(33) Touboul, D.; Brunelle, A.; Halgand, F.; De La Porte, S.; Laprevote, O. *J. Lipid Res.* **2005**, *46*, 1388.

(34) Debois, D.; Brunelle, A.; Laprevote, O. *Int. J. Mass Spectrom.* **2007**, *260*, 115.

(35) Borner, K.; Malmberg, P.; Mansson, J. E.; Nygren, H. *Int. J. Mass Spectrom.* **2007**, *260*, 128.

(36) Malmberg, P.; Borner, K.; Chen, Y.; Friberg, P.; Hagenhoff, B.; Mansson, J. E.; Nygren, H. *Bba-Mol Cell Biol L* **2007**, *1771*, 185.

(37) Touboul, D.; Roy, S.; Germain, D. P.; Chaminade, P.; Brunelle, A.; Laprevote, O. *Int. J. Mass Spectrom.* **2007**, *260*, 158.

(38) Debois, D.; Bralet, M. P.; Le Naour, F.; Brunelle, A.; Laprevote, O. *Anal. Chem.* **2009**, *81*, 2823.

(39) Brunelle, A.; Laprevote, O. *Anal. Bioanal. Chem.* **2009**, *393*, 31.

(40) Tahallah, N.; Brunelle, A.; De La Porte, S.; Laprevote, O. *J. Lipid Res.* **2008**, *49*, 438.

(41) Monroe, E. B.; Jurchen, J. C.; Lee, J.; Rubakhin, S. S.; Sweedler, J. V. *J. Am. Chem. Soc.* **2005**, *127*, 12152.

(42) Chen, C.; Nagy, G.; Walker, A. V.; Maurer, K.; McShea, A.; Moeller, K. D. *J. Am. Chem. Soc.* **2006**, *128*, 16020.

(43) Lee, C. Y.; Harbers, G. M.; Grainger, D. W.; Gamble, L. J.; Castner, D. G. *J. Am. Chem. Soc.* **2007**, *129*, 9429.

(44) Mahoney, C. M.; Roberson, S. V.; Gillen, G. *Anal. Chem.* **2004**, *76*, 3199.

(45) Wucher, A.; Winograd, N. *Anal. Bioanal. Chem.* **2010**, *396*, 105.

(46) Postawa, Z.; Czerwinski, B.; Szewczyk, M.; Smiley, E. J.; Winograd, N.; Garrison, B. J. *J. Phys. Chem. B* **2004**, *108*, 7831.

(47) Shard, A. G.; Brewer, P. J.; Green, F. M.; Gilmore, I. S. *Surf. Interface Anal.* **2007**, *39*, 294.

(48) Cheng, J.; Kozole, J.; Hengstebeck, R.; Winograd, N. *J. Am. Soc. Mass Spectrom.* **2007**, *18*, 406.

(49) Wucher, A.; Cheng, J.; Winograd, N. *J. Phys. Chem. C* **2008**, *112*, 16550.

(50) Zheng, L. L.; Wucher, A.; Winograd, N. *Anal. Chem.* **2008**, *80*, 7363.

(51) Sjovall, P.; Rading, D.; Ray, S.; Yang, L.; Shard, A. G. *J. Phys. Chem. B* **2010**, *114*, 769.

(52) Wucher, A.; Cheng, J.; Winograd, N. *Anal. Chem.* **2007**, *79*, 5529.

(53) Nygren, H.; Hagenhoff, B.; Malmberg, P.; Nilsson, M.; Richter, K. *Microsc Res Techniq* **2007**, *70*, 969.

(54) Fletcher, J. S.; Lockyer, N. P.; Vaidyanathan, S.; Vickerman, J. C. *Anal. Chem.* **2007**, *79*, 2199.

(55) Braun, R. M.; Blenkinsopp, P.; Mullock, S. J.; Corlett, C.; Willey, K. F.; Vickerman, J. C.; Winograd, N. *Rapid Commun. Mass Spectrom.* **1998**, *12*, 1246.

(56) Sostarecz, A. G.; Cannon, D. M.; McQuaw, C. M.; Sun, S. X.; Ewing, A. G.; Winograd, N. *Langmuir* **2004**, *20*, 4926.

(57) Sostarecz, A. G.; McQuaw, C. M.; Ewing, A. G.; Winograd, N. *J. Am. Chem. Soc.* **2004**, *126*, 13882.

(58) McQuaw, C. M.; Sostarecz, A. G.; Zheng, L. L.; Ewing, A. G.; Winograd, N. *Langmuir* **2005**, *21*, 807.

(59) McQuaw, C. M.; Zheng, L. L.; Ewing, A. G.; Winograd, N. *Langmuir* **2007**, *23*, 5645.

(60) Zheng, L.; McQuaw, C. M.; Ewing, A. G.; Winograd, N. *J. Am. Chem. Soc.* **2007**, *129*, 15730.

(61) Baker, M. J.; Zheng, L.; Winograd, N.; Lockyer, N. P.; Vickerman, J. C. *Langmuir* **2008**, *24*, 11803.

(62) Zheng, L. L.; Wucher, A.; Winograd, N. *Appl. Surf. Sci.* **2008**, *255*, 816.

Chapter 2

Ionization Effects in Molecular Depth Profiling of Trehalose Films using Buckminsterfullerene (C_{60}) Cluster Ions

 This paper was submitted as a proceeding paper for SIMS XVII and has been expanded for further clarification.

2.1 Introduction

Secondary ion mass spectrometry (SIMS) is finding more applications in chemical imaging of biological samples.[1] With the development of cluster ion sources, it has been shown that it is possible to identify the lateral distribution of molecular species on and within the surface of cells and tissues.[2-7] Therefore, SIMS bioimaging can be expanded from two-dimensional (2-D) analysis to three-dimensional (3-D) analysis.

One of the challenges in mass spectrometry bioimaging is obtaining useful biological molecular information in a complicated environment, which contains a large number of various molecular and atomic species. The matrix of biological samples has a great influence on the ionization of analytes.[8] Studies have shown that the yield of protonated species can be enhanced in hydrated environment by C_{60} bombardment.[9-10] In particular, it has been suggested that the formation efficiency of secondary molecular ions $[M+H]^+$ or specific fragments derived from these may correlate with the liberation of

protons by bombardment-induced dissociation of water molecules.[10] Enhancement or suppression of $[M+H]^+$ is also partially a result of competition for protons between sputtered analytes, depending upon their gas phase basicity.[11]

Biological salts have a significant effect on the ion formation in both SIMS and matrix-assisted laser desorption ionization (MALDI) experiments.[4,8,12-14] The presence of cations has been observed to aid in the cationization of molecular ions in MALDI experiments. Alkali, alkali earth or transition metals have been added into some samples to help to form high molecular weight polymeric ions in SIMS analysis.[15-16] On the other hand, salts in biological samples can also have some negative influence, such as suppression of protonated ions.[15-16] Depth profiling of brain tissue by a 40-keV C_{60} primary ion beam shows a rapid loss of molecular signals from lipid and protein fragments during sputtering, accompanied by the increase of signals from sodium and potassium adducts of phosphate and protein fragments.[4] Sample washing protocols have been established to eliminate salt-related suppression effect. Washing brain tissue sample with an ammonium formate solution effectively reduces salt level and improves molecular ion peak intensities..[4]

Thus far, the role salt plays in the ionization process is not fully understood. In order to investigate salt effects Piwowar *et al.* doped thin films of arginine with a series of alkali chlorides.[17] The acquired data indicates that salt-related adducts are detrimental to molecular ion signals. It is speculated that the decrease in molecular ion signal is caused by ion neutralization involving the counter anions. In that experiment, the molecular ion intensity loss to chloride-neutralization was recovered using sample washing techniques previously described and newly established cryogenic protocols.

Analyzing the sample in frozen-hydrated state and performing SIMS analysis at liquid nitrogen temperature resulted in enhanced secondary ion yield and a significant amelioration of the salt-related suppression effects.

Our previous work has shown that spin-coated trehalose films doped with peptides are a reliable platform for depth profiling analysis. These films have been used to establish valuable parameters for 3-D imaging experiments.[18] In the future these parameters will be useful in the analysis and characterization of biomaterials. In this experiment, trehalose films doped with peptides are used as a model system to study ionization effects during C_{60} sputtering. The study shows that the formation of protonated molecular species is strongly influenced by the films water content. Also, the addition of salts greatly influences the total molecular ion intensity of the trehalose matrix and peptide dopant in a very different way.

2.2 Experimental Section

Trehalose, peptide Gly-Gly-Tyr-Arg (GGYR) and sodium chloride (NaCl) were purchased from Sigma-Aldrich Co. (St. Louis, MO) and used without further purification. The water used in preparation of all aqueous solutions was purified by a Nanopure Diamond Life Science Ultrapure Water System (Barnstead International, Dubuque, IA) and had a resistivity of at least 18.2 MΩ-cm. Pre-sliced 5 mm × 5 mm single crystal (100) silicon wafers were supplied by Ted Pella Inc. (Redding, CA). The film preparation process has been described elsewhere.[18] An aqueous solution of 0.5 M trehalose and 0.005 M GGYR was used to make salt-free film. Films doped with sodium chloride were

prepared by a series of trehalose peptide solutions containing various concentrations of NaCl.

The depth profile experiments were performed in a ToF-SIMS instrument equipped with a 40-keV C_{60} source (IOG 40-60, Ionoptika; Southampton, U.K.) at a 40^0 angle relative to the surface normal. For depth profiling, the C_{60}^+ ion beam was operated in DC mode to erode through the film at an area of 350 μm × 450 μm in 3 s intervals. Between erosion cycles, ToF mass spectra were acquired at an area of 250 μm × 350 μm inside the sputtered region using the pulsed C_{60}^+ projectile beam at an ion fluence of 10^{10} ions/cm^2. The crater depths were measured by a KLA-Tencor Nanopics 2100 atomic force microscopy (AFM) in contact mode.

2.3 Results and Discusstion

2.3.1 Ionization effects of water molecules

We begin the discussion of ionization effects by looking at the initial stages of a depth profile obtained on a clean, salt-free trehalose film. The profile obtained in our earlier work[18], as shown in Figure **2-1** (a), reveals an initial increase in the quasimolecular ion signal $[M\text{-}OH]^+$ of trehalose at m/z 325.1 and the molecular ion signal $[M+H]^+$ of peptide dopant GGYR at m/z 452.2. Both of these ions are formed through the protonation of the parent molecules. The quasimolecualr ion $[M\text{-}OH]^+$ is a product of molecular species formed when the protonated trehalose molecule loses a water molecule.

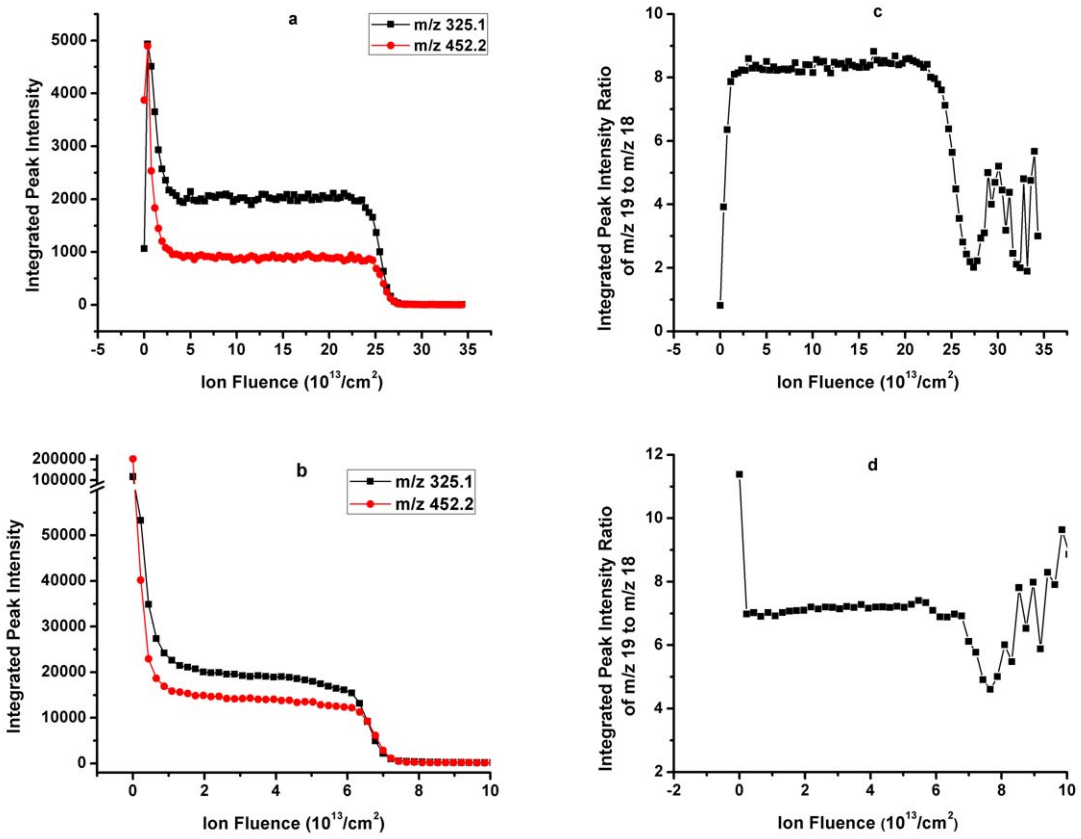

Figure **2-1**: Molecular ion signals of the trehalose (m/z 325.1) and peptide dopant molecule (m/z 452.2) from film A and B are plotted vs. ion fluence in (a) and (b). Signal ratios of protonated (m/z 19) and non-protonated (m/z 18) water molecules from Film A and B are plotted vs. C_{60}^{+} ion fluence in (c) and (d).

As explained elsewhere in this volume[19], the initial transient is attributed to an increase of the ionization efficiency superimposed by an exponential decay of the molecule ejection yield induced by damage accumulation. As seen in Figure **2-1** (b), however, this effect is not always observed, even though the films analyzed in both cases have been deposited in the same way. To investigate the cause of this deviation, we take the signal intensity ratio of protonated (m/z 19) and non-protonated (m/z 18) water molecules as an indicator for the availability of free protons liberated by the ion bombardment, which may promote

the formation of the observed molecular ions.[9-10] As shown in Figure **2-1** (c), it is indeed found that the increased ionization efficiency in film A is correlated with an *increase* of the 19/18 ratio by roughly a factor of 10. In contrast, a much less pronounced variation is observed for film B, and at the same time the 19/18 ratio is found to *decrease* (see Figure 1(d)). This finding is consistent with the fact that the ionization efficiency does not seem to increase in this case. Looking at the total intensity at m/z 18 and 19 compared to that of both the molecular ions at the beginning of the profile and the Si signal at m/z 28 measured after removal of the entire film, one finds that film A contains about a factor of 5-10 more water than film B. Apparently, the water content of the deposited trehalose film critically influences the surface variation of the ionization efficiency, supporting the notion that the bombardment induced dissociation of water might be a means to enhance the formation of protonated molecular ions.

2.3.2 Salt effects on ion formation

In order to examine how biological salt affect depth profiling, NaCl (1% by weight) was added to the peptide doped trehalose solution before the films were prepared. The salt-doped trehalose film was subjected to the same depth profile analysis used for the salt-free film.

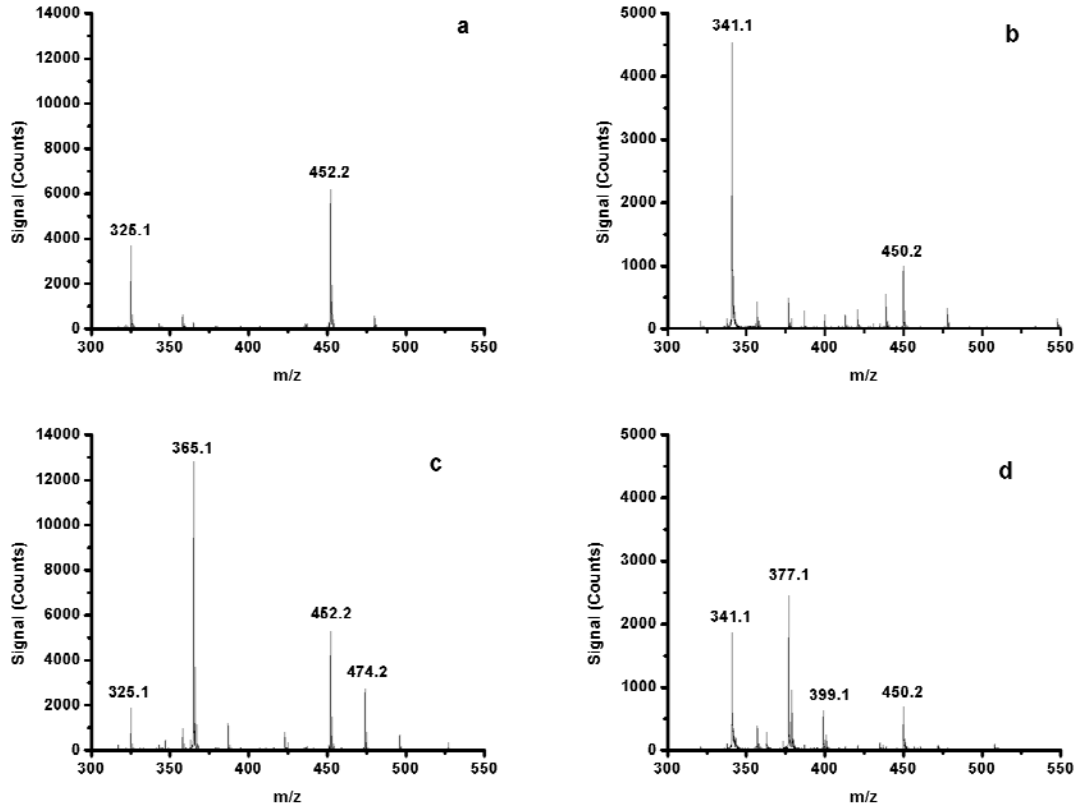

Figure **2-2**: ToF-SIMS positive ion spectrum (a) and negative ion spectrum (b) taken at the surface of salt-free GGYR trehalose film; ToF-SIMS positive ion spectrum (c) and negative ion spectrum (d) taken at the surface of 1% NaCl doped GGYR trehalose film.

The presence of NaCl drastically changes the ions formed and detected. Sodium adducts of trehalose and GGYR are found in the spectra obtained from the salt-doped film. This phenomenon is also commonly observed in MALDI experiments from biological samples. Besides the sodium adducts, anion adduct peaks are also observed. The positive and negative spectra taken at the surface of salt-free and salt-doped films are shown in Figure **2-2** for a comparison**.** On the salt-free film, the quasimolecular ion $[M\text{-}OH]^+$ of trehalose at m/z 325.1 and the molecular ion $[M+H]^+$ of GGYR at m/z 452.2 are the dominating

peaks in the positive spectrum, and $[M-H]^-$ of trehalose and GGYR at m/z 341.1 and 450.2, respectively, are the highest peaks in the negative spectrum. On the salt-doped film, the sodium adduct ion $[M+Na]^+$ of trehalose at m/z 365.1 is the most significant peak in the positive spectrum. A significant decrease in the trehalose $[M-OH]^+$ and GGYR $[M+H]^+$ ions are also observed. Also detected was the sodium adduct of GGYR $[M+Na]^+$ at m/z 474.2. The negative spectrum of the salt-doped film exhibits the similar features. The molecular ions $[M-H]^-$ of trehalose and GGYR are suppressed with the addition of salt while sodium and chloride adducts of trehalose appear in the same spectrum, such as $[M-2H+Na]^-$ at m/z 363.1, $[M+Cl]^-$ at m/z 377.1 and $[M-H+Na+Cl]^-$at m/z 399.1. The peaks related to cation and anion adducts are listed in Table **2-1** with their assigned formula.

Table **2-1**: Proposed structure of the salt adducts

m/z	**ion**	**m/z**	**ion**
365.1	Trehalose $[M+Na]^+$	399.1	Trehalose $[M-H+Na+Cl]^-$
363.1	Trehalose $[M-2H+Na]^-$	423.1	Trehalose $[M+2Na+Cl]^+$
377.1	Trehalose $[M+Cl]^-$	474.2	GGYR $[M+Na]^+$
387.1	Trehalose $[M-H+2Na]^+$	495.1	GGYR $[M+H-CH_3+Na+Cl]^+$

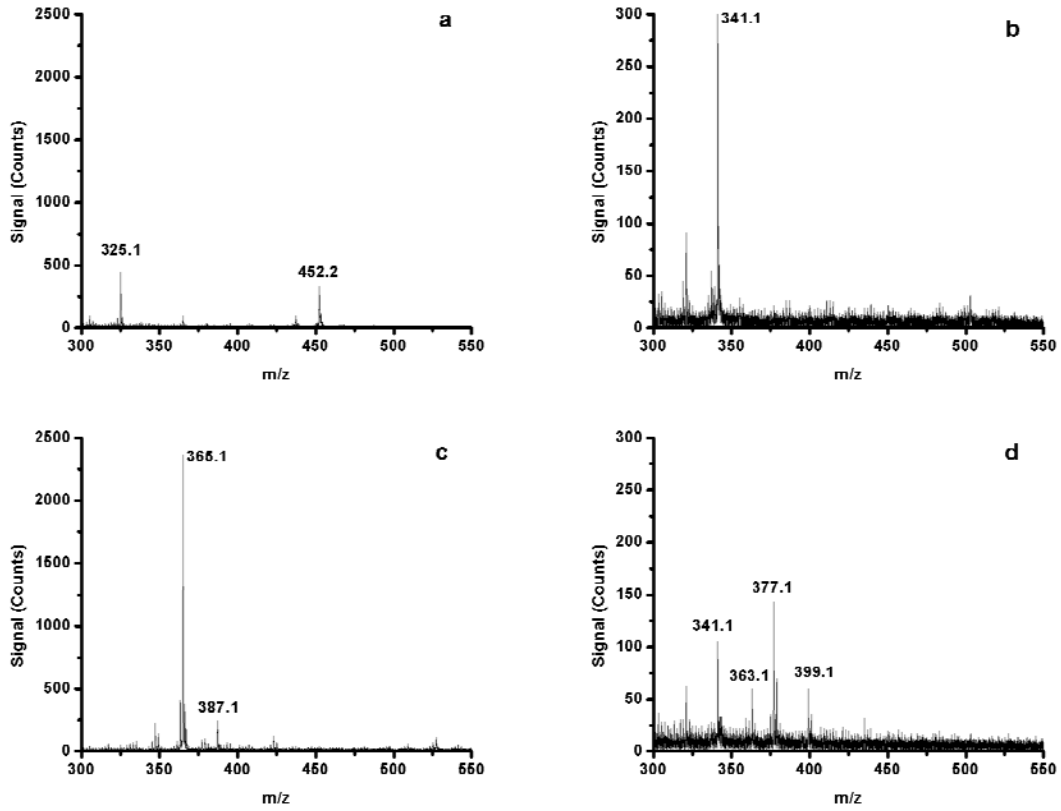

Figure **2-3**: ToF-SIMS positive ion spectrum (a) and negative ion spectrum (b) of salt-free GGYR trehalose film after sputtered with a fluence of 2.0×10^{13} ions/cm^2; ToF-SIMS positive ion spectrum (c) and negative ion spectrum (d) of 1% NaCl doped GGYR trehalose film after sputtered with a fluence of 2.0×10^{13} ions/cm^2.

We also examined the mass spectral data after the surface layer was removed and after the molecular ion signal reached steady-state. The data reveals that the bulk of the film has a different mass spectrum from the one acquired on the surface. The positive and negative spectra of salt-free and 1% NaCl doped film after sputtering with a fluence of 2.0×10^{13} ions/cm^2 are shown in Figure **2-3**. The positive spectrum of the unsalted film (Figure **2-3** (a)) is still dominated by trehalose $[M\text{-}OH]^+$ and GGYR $[M+H]^+$. In the negative spectrum (Figure **2-3** (b)), only trehalose $[M\text{-}H]^-$ at 341.1 is found and GGYR

$[M-H]^-$ disappears after bombardment with a high fluence of C_{60}^+. On the salt-doped film, the molecular ion signals of trehalose and GGYR drop more than on the surface in the positive spectrum, while the sodium and chloride adducts from trehalose completely dominate the spectra in the same high mass region. As shown in Figure **2-3** (c), $[M+Na]^+$ of trehalose at m/z 365.1 is the most significant signal and $[M-H+2Na]^+$ is also been detected at m/z 387.1. A form of chloride adduct is found at m/z 423.1 as $[M+2Na+Cl]^+$. The negative ion spectrum (Figure **2-3** (d)) is mainly dominated by the trehalose signals, including the molecular ion $[M-H]^-$ and various sodium and chloride adducts, such as $[M-2H+Na]^-$, $[M+Cl]^-$, and $[M-H+Na+Cl]^-$.

The depth profiles of molecular ion signals are shown in Figure **2-4** for the salt-free and 1% NaCl doped film. The sputtered crater's depth was measured with an AFM and the C_{60}^+ sputter rates of both films were calculated. Although it has been observed that peptide doped trehalose films have a significantly lower sputter yield than pure trehalose films[18], NaCl doesn't seem to have the same effect and the sputter yield remains practically the same after 1% NaCl is added. As shown in Figure **2-4**, similar depth profiles are obtained from the salt-free film and 1% NaCl doped film. The signal intensities of $[M-OH]^+$ and $[M+H]^+$, however, are both suppressed by the same amount upon the addition of NaCl. At the beginning of the depth profile, the molecular ion signals are reduced by a factor of 2, while in the steady state the signals are suppressed by a factor of 10. Since the ratio between initial and steady state signal reflects the cleanup efficiency[20], i.e., the ratio between the number of sputtered and damaged molecules per projectile impact, this finding indicates that the presence of NaCl must enhance the damage cross section during the ion bombardment.

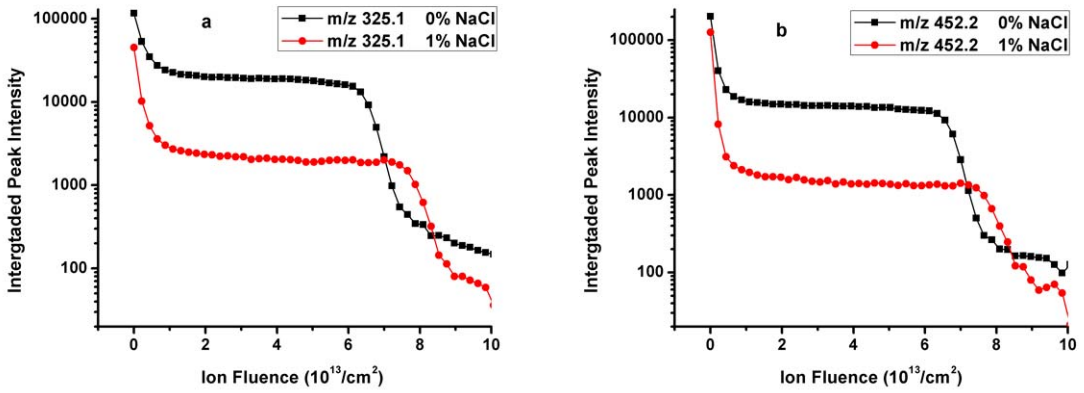

Figure **2-4**: Depth profiles of trehalose film doped with GGYR and 0% and 1% NaCl. Secondary ion intensities of trehalose at m/z 325.1 and GGYR at m/z 452.2 are plotted vs. C_{60}^+ ion fluence respectively in (a) and (b).

As we discussed earlier, the addiction of NaCl immediately changed the ion formation path of trehalose and GGYR molecules. Although sodium adduct peak of $[M+Na]^+$ is found for both trehalose and GGYR, the presence of NaCl induces different behavior of the trehalose and GGYR peptide signals. With NaCl present, the total secondary ion intensity of trehalose quasimolecular ions $[M-OH]^+$ and sodium adducts $[M+Na]^+$ is enhanced more than three times mainly by the prominent formation of $[M+Na]^+$, as shown in Figure **2-5** (a). The existence of $[M+Na]^+$ of GGYR is also detected, but its intensity from salt-doped film is only 10% of the intensity of $[M+H]^+$ from salt-free film. Consequently, the total secondary ion intensity of GGYR $[M+H]^+$ and $[M+Na]^+$ is found to decrease by more than 70% in the salt-doped film (see Figure **2-5** (b)). Based on this observation, the trehalose molecule is more likely to bind with sodium ion compared to the GGYR peptide.

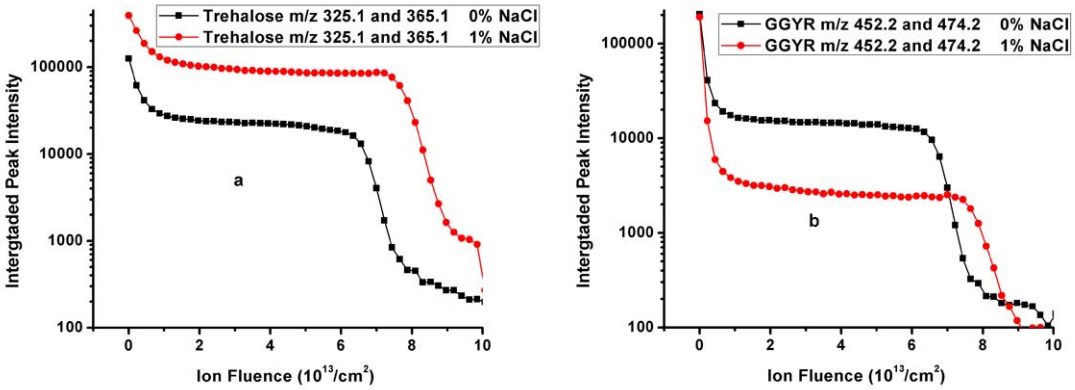

Figure **2-5**: Total secondary ion intensities of trehalose molecular ions $[M\text{-}OH]^+$ at m/z 325.1 and sodium adducts $[M+Na]^+$ at m/z 365.1 from the films doped with 0% and 1% NaCl are plotted vs. C_{60}^+ ion fluence in (a). Total secondary ion intensities of GGYR molecular ions $[M+H]^+$ at m/z 452.2 and sodium adducts $[M+Na]^+$ at m/z 474.2 from the films doped with 0% and 1% NaCl are plotted vs. C_{60}^+ ion fluence in (b).

As observed in both SIMS and MALDI experiments, the formation of sodium attached ions is dependent upon the chemical structure of the analyte molecule.[21] Structurally trehalose has eight hydroxyl groups available to interact with available sodium cations. The addition of NaCl indeed helps the overall ionization of trehalose by forming sodium adducts. On the other hand, GGYR has a lower affinity to sodium adduction due to its weak basicity. As a result, very few sodium adducts were observed in the spectrum. The loss of the protonated molecular ion $[M+H]^+$ from salt adduction is less than the overall decrease in GGYR ionization. Therefore, the cationization is not the only attributing factor to the observed loss of GGYR molecular ions. Based on experimental results obtained on arginine film, it has been proved that the arginine molecular ions are neutralized by chloride counter-anions.[17] One might therefore speculate, that the GGYR molecular ion may also exhibit a similar behavior and have a

higher binding efficiency for Cl^- instead of Na^+. That would neutralize the $[M+H]^+$ and reduce the observed molecular ion signal.

2.3.3 Effects of salt concentration

The concentration of salt in the trehalose film influences the systems ionization efficiency as well. Total molecular ion signals, protonated and adducted, obtained with varying concentrations of doped NaCl are shown in Figure **2-6.** The total secondary ion intensity of trehalose is the sum of $[M-OH]^+$ at 325.1, $[M+Na]^+$ at m/z 365.1, $[M-H+2Na]^+$ at m/z 387.1 and $[M+2Na+Cl]^+$at m/z 423.1. Films doped with 0.001% and 0.01% NaCl experience a less than 9% fluctuation in the total trehalose intensity. More obvious enhancement on the total ionization of trehalose is observed on the films doped with 0.1% NaCl and higher concentrations. At the film surface, the total molecular ion intensity of trehalose is doubled by the addition of 0.1% NaCl and tripled by the addition of 1% and 2% NaCl. Overall the enhancement effect seems to be saturated at higher NaCl concentrations. The films doped with 10% NaCl shows about the same degree of enhancement of the total molecular ion intensity at the surface as the 0.1% NaCl film. The signal at steady state is slightly different from the results obtained at the film surface. The trehalose molecular ion signal dependence on NaCl concentration after sputtering with a fluence of 2.0×10^{13} ions/cm^2 is shown in Figure **2-6** (b). The ionization enhancement is maximized at 1%. Although the presence of sodium cation is able to enhance the ionization of basic molecules in small amounts, excessive amounts of salt can be detrimental to the signal.

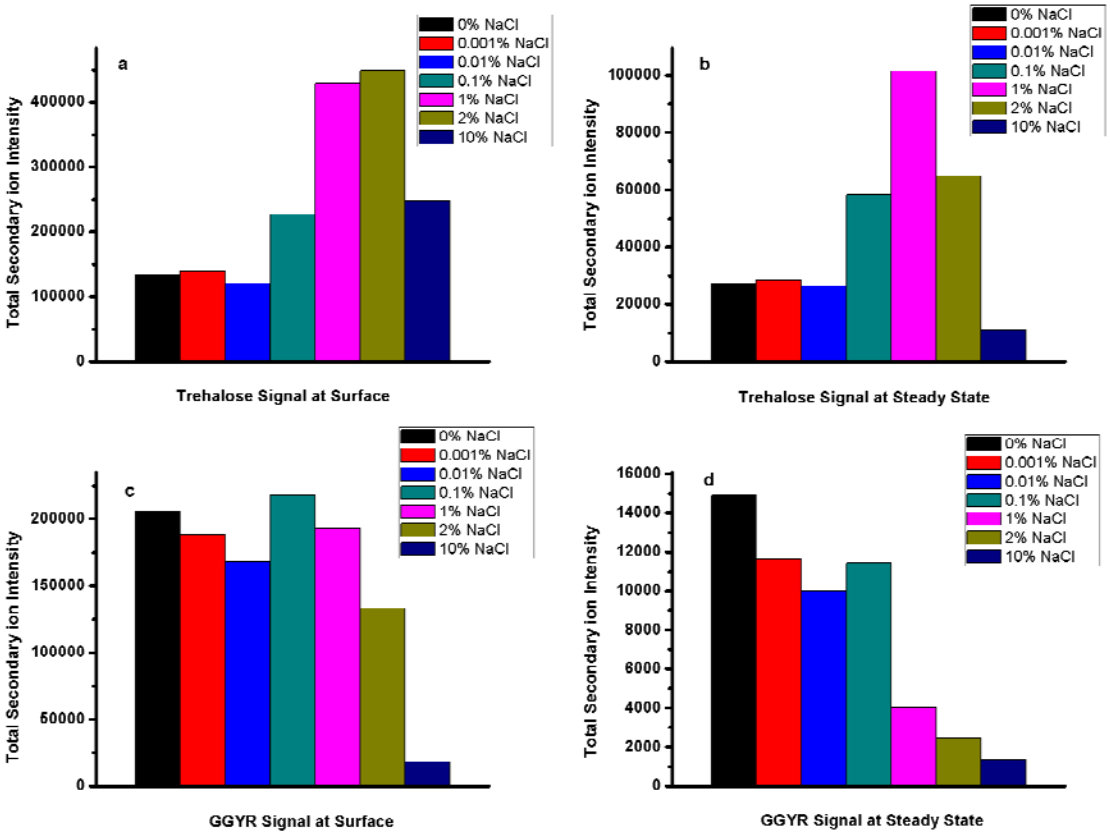

Figure **2-6**: Total molecular ion intensities of trehalose measured at the film surface (a) and after sputtering with a C_{60}^+ fluence of 2.0×10^{13} ions/cm^2 (b); total molecular ion intensities of GGYR at the film surface (c) and after sputtering with a C_{60}^+ fluence of 2.0×10^{13} ions/cm^2 (d). Intensities at m/z 325.1, m/z 365.1, m/z 387.1 and m/z 423.1 are added to calculate the total intensity of trehalose. Intensities at m/z 452.2, m/z 474.2 and m/z 495.1 are used to obtain total intensity of GGYR.

We already observed the addition of 1% NaCl suppresses the ionization of GGYR molecules. Here we use $[M+H]^+$ at m/z 452.2, $[M+Na]^+$ at m/z 474.2 and $[M+H-CH_3+Na+Cl]^+$ at 495.1 to calculate the total secondary ion intensity of GGYR. At the surface, the suppression effect is most significant at the highest salt level, 10% NaCl. At steady state, the suppression of GGYR molecular ion is observed at all concentrations of NaCl. The suppression of GGYR molecular ion is most severe in the films doped with

0.1% and higher concentrations of NaCl. For the molecules with low cationization efficiency, such as GGYR, it is necessary to reduce the salt level in order to preserve the molecular ion information.

2.4 Conclusions

Using peptide doped trehalose film as a model system, we have shown that the molecular ionization efficiency is affected by the water content of the sample film. This behavior is attributed to the enhanced availability of protons due to ion bombardment induced dissociation of water molecules. The presence of salt in the film affects the ionization of different organic molecules in completely different ways. In the case of trehalose, the total ionization efficiency of the ejected molecules is enhanced by forming sodium adducts, while a strong decrease of the molecular ionization efficiency is observed for the GGYR peptide in a trehalose matrix.

2.5 Acknowledgement

The authors would like to thank Dr. Juan Cheng for her contributions to the presented research. Financial support from the National Institute of Health under grant no. 2R01 EB002016-16 and the National Science Foundation under grant no. CHE-0908226 are acknowledged.

2.6 References

(1) Winograd, N. *Anal. Chem.* **2005**, *77*, 142a.

(2) Fletcher, J. S.; Lockyer, N. P.; Vaidyanathan, S.; Vickerman, J. C. *Anal. Chem.* **2007**, *79*, 2199.

(3) Nygren, H.; Malmberg, P. *Trends Biotechnol.* **2007**, *25*, 499.

(4) Jones, E. A.; Lockyer, N. P.; Vickerman, J. C. *Anal. Chem.* **2008**, *80*, 2125.

(5) McDonnell, L. A.; Heeren, R. M. A. *Mass Spectrom. Rev.* **2007**, *26*, 606.

(6) Parry, S.; Winograd, N. *Anal. Chem.* **2005**, *77*, 7950.

(7) Fletcher, J. S.; Rabbani, S.; Henderson, A.; Blenkinsopp, P.; Thompson, S. P.; Lockyer, N. P.; Vickerman, J. C. *Anal. Chem.* **2008**, *80*, 9058.

(8) Chen, W. Y.; Chen, Y. C. *Anal. Chem.* **2007**, *79*, 8061.

(9) Weibel, D. E.; Lockyer, N.; Vickerman, J. C. *Appl. Surf. Sci.* **2004**, *231-2*, 146.

(10) Conlan, X. A.; Lockyer, N. P.; Vickerman, J. C. *Rapid Commun. Mass Spectrom.* **2006**, *20*, 1327.

(11) Jones, E. A.; Lockyer, N. P.; Kordys, J.; Vickerman, J. C. *J. Am. Soc. Mass Spectrom.* **2007**, *18*, 1559.

(12) Knochenmuss, R.; Zenobi, R. *Chem Rev* **2003**, *103*, 441.

(13) Knochenmuss, R.; McCombie, G.; Faderl, M. *J. Phys. Chem. A* **2006**, *110*, 12728.

(14) Knochenmuss, R. *Analyst* **2006**, *131*, 966.

(15) Fujii, T. *Mass Spectrom. Rev.* **2000**, *19*, 111.

(16) Zhang, J.; Zenobi, R. *J. Mass Spectrom.* **2004**, *39*, 808.

(17) Piwowar, A. M.; Lockyer, N. P.; Vickerman, J. C. *Anal. Chem.* **2009**, *81*, 1040.

(18) Cheng, J.; Winograd, N. *Anal. Chem.* **2005**, *77*, 3651.

(19) Willingham, D.; Brenes, D. A.; Wucher, A.; Winograd, N. *J. Phys. Chem. C* **2010**, *114*, 5391.

(20) Wucher, A.; Cheng, J.; Winograd, N. *J. Phys. Chem. C* **2008**, *112*, 16550.

(21) Hanton, S. D.; Clark, P. A. C.; Owens, K. G. *J. Am. Soc. Mass Spectrom.* **1999**, *10*, 104.

Chapter 3

Organic Depth Profiling of an Irganox Delta Layer by Cluster Ion Beams

This project is part of VAMAS TW 2, 2009 Sub-project A3(d) Static SIMS Interlaboratory Study: organic depth profiling by cluster ion beams.

3.1 Introduction

In recent years, the development of cluster ions has led to revolutionary opportunities for secondary ion mass spectrometry (SIMS). Compared to atomic ion sources, bombardment by cluster ion beams generates high sputter yield, while producing little chemical damage accumulation.[1-3] Materials at the surface can be removed by a cluster ion beam without causing substantial damage to underlying materials. As a result, it is possible to study complex organic sample at the surface, and, through sputtering, acquire the in-depth molecular information layer-by-layer in a process termed depth profiling.

Depth profile experiments have been performed with cluster ion beams on various organic samples under different experimental conditions. Reported data have shown that the depth profile obtained from biodegradable poly(lactic acid) is able to maintain stable secondary ion signals with the increase of the SF_5^+ fluence.[4] Successful depth profiles have also been achieved on spin-coated trehalose films at room temperature with a C_{60}^+ beam.[5] The sputter yield was found to be affected by the composition of the film, as the

addition of 1% (by mole) peptide significantly changed the sputter yield. The effect of kinetic energy was investigated over the range of 20 to 120 keV and the results show that an impact energy between 20–40 keV provides the best depth resolution and the highest cleanup efficiencies.[6] However, for some organic materials, like poly(methyl methacrylate) and aluminum tris(hydroxyquinolate), the secondary ion signals gradually degrade during the depth profiling and a real steady state is never reached at room temperature.[7-8] This degradation was proposed to be related to the decrease of the sputter yield and the build-up of surface roughness.[8-10]

To quantitatively investigate the key parameters of depth profiling, the National Physical Lab (NPL) in the UK constructed an organic delta layer system using two different materials, Irganox 1010 and Irganox 3114.[11] Thin layers of Irganox 3114 (~3 nm) were deposited between thick layers of Irganox 1010 (~55 nm or ~90 nm), assembling a structure similar to the inorganic delta layers commonly applied as reference materials in dynamic SIMS. Irganox delta layers prepared by vapor deposition appear to be reproducible, homogeneous, and planar. Therefore, they serve as a suitable reference material to evaluate the reliability and reproducibility of organic depth profiling. Depth resolution and sputter yield can be directly determined on this system. The depth profile results obtained with a C_{60}^+ beam at 5-30 keV illustrate that depth resolution and sputter yield are both dependent upon ion fluence. In addition, it is revealed that surface roughening is mainly responsible for the degradation of secondary ion signal and sputter yield.[11]

In the work presented here, Irganox delta layer samples containing 4 Irganox 3114 marker layers are subjected to depth profile analysis with a 40-keV C_{60}^+ beam.

Successful depth profiles are acquired, and the repeatability of organic depth profiling is evaluated by multiple runs under the same conditions. The effect of incident angle is also investigated, showing that a larger incident angle is preferred to improve the quality of depth profiles.

3.2 Experimental Section

The samples were prepared by NPL and the preparation procedure has been described in detail elsewhere.[11-12] Briefly, a single crystal (100) silicon wafer was cut to ~10 mm × 10 mm squares which were used as substrates. After soaked overnight in isopropanol and dried by nitrogen flow, the silicon wafers were put in an Edwards AUTO 360 vacuum coater for physical vapor deposition. Layers of Irganox 1010 and Irganox 3114 were alternatively evaporated onto the silicon wafers while the thickness of each layer was monitored by a quartz crystal microbalance (QCM). Two similar samples were analyzed in this work and their structures are shown in Table **3-1**. The samples were stable for up to six months at room temperature. Exposure to light can cause some degradation of the outer most Irganox 1010 layer after this time period, however, the degradation is negligible if the sample is kept in the dark. The coating area is 8 mm × 8 mm, and the SIMS depth profile analysis was performed within a 6 mm × 6 mm area in the center of the coated region.

Depth profile experiments were performed in a ToF-SIMS instrument equipped with a fullerene cluster ion source (IOG 40-60, Ionoptika; Southampton, U.K.), mounted at a 40^0 angle relative to the surface normal. Details of this instrumentation have been

described elsewhere.[5,13] The source was operated with a focused (~7 μm diameter) 40-keV C_{60}^+ ion beam. For depth profiling, the C_{60}^+ ion beam was operated alternatively between data acquisition and sputter erosion cycles. A DC beam was used to erode through a 400 μm × 500 μm area of the film in 2 s intervals. Between erosion cycles, negative SIMS images were acquired from the same area using a 50 ns pulsed C_{60}^+ beam at an ion fluence of 10^{10} ions/cm^{-2}. ToF mass spectra were retrospectively extracted from the image data from an area of 300 μm × 400 μm inside the sputtered region.

Table **3-1**: Structure of Irganox delta layer samples

Layer*	Type	Sample 1	Sample 2
1	Irganox 1010	47.6 nm	48.2 nm
2	Irganox 3114	3.0 nm	3.0 nm
3	Irganox 1010	48.2 nm	48.8 nm
4	Irganox 3114	3.1 nm	3.1 nm
5	Irganox 1010	95.1 nm	96.2 nm
6	Irganox 3114	3.7 nm	3.8 nm
7	Irganox 1010	95.6 nm	96.7 nm
8	Irganox 3114	3.7 nm	3.8 nm
9	Irganox 1010	95.1 nm	96.2 nm

*Layer 1 is the top layer of the film and layer 9 is the first evaporated layer on the substrate.

The incident angle was adjusted between 30^0 and 60^0 using a customized mount. The dimensions of the craters were measured by a KLA-Tencor Nanopics 2100 atomic force microscope (AFM) after depth profile experiments. The applied incident angle θ was then determined by the size of the crater from $\Delta y=\Delta x/\cos\theta$ (θ is the impact angle of the primary beam relative to the surface normal).

3.3 Results and Discussion

3.3.1 Depth profile analysis

The chemical structures of Irganox 1010 and Irganox 3114 are shown in Figure **3-1**. Their characteristic negative secondary ions, previously identified by a 5~30 keV C_{60} ion source[11], are listed in Table **3-2**. The 40-keV C_{60}^{+} beam is able to detect all these ions, including the molecular ion $[M-H]^-$ of Irganox 1010 at m/z 1175. Four fragment ions are used to characterize the Irganox 3114 marker layers. They are two fragment ions in the high mass region, $C_{33}H_{46}N_3O_5^-$ (m/z 564) and $C_{18}H_{24}N_3O_4^-$ (m/z 346), and two small ions, CN^-(m/z 26) and CNO^- (m/z 42). Among them CNO^- gives the highest intensity in the spectrum.

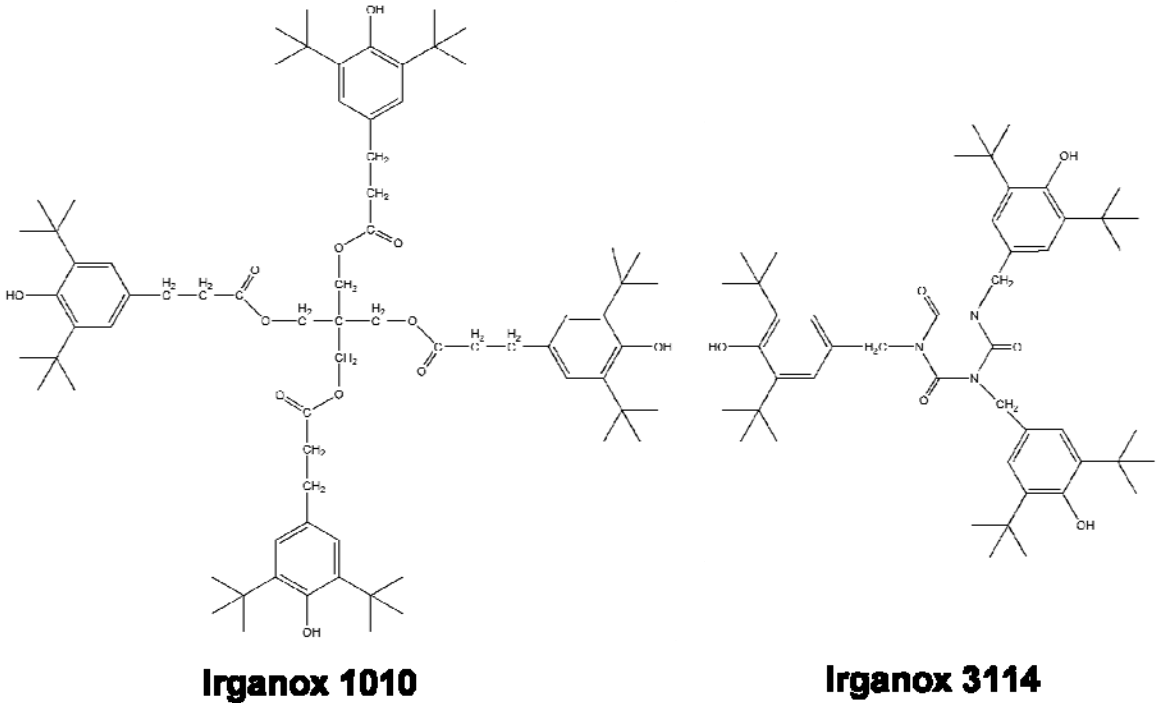

Figure **3-1**: Chemical structure of Irganox 1010 ($C_{73}H_{108}O_{12}$) and Irganox 3114 ($C_{48}H_{69}N_3O_6$).

Table **3-2**: Negative secondary ions from Irganox 1010 and Irganox 3114

Irganox 1010 (matrix material)		Irganox 3114 (marker material)	
m/z	ion	m/z	ion
41	C_2HO^-	26	CN^-
59	$C_2H_3O_2^-$	42	CNO^-
175	$C_{12}H_{15}O^-$	346	$C_{18}H_{24}N_3O_4^-$
231	$C_{16}H_{23}O^-$	564	$C_{33}H_{46}N_3O_5^-$
277	$C_{17}H_{25}O_3^-$		
1175	$C_{73}H_{107}O_{12}^-$		

The depth profiles are shown in Figure **3-2**. As illustrated in Figure **3-2** (a-b), the first two marker layers are clearly detected using all four characteristic ions, which are

depicted as two peaks consisting of an exponential leading edge and an exponential trailing edge. However, the signal maximum of the second marker layer is less than 45% of the first one. The signal decline becomes more severe at higher ion fluence. When it reaches the third marker layer, the signal intensity drops by more than 87% and the peak becomes much wider. As a result, the signal from the forth marker layer appears as a small hump and can hardly be recognized due to its low intensity. Signal decline has also been observed with the fragment ions of Irganox 1010 as seen in Figure **3-2** (c). After the initial rise, which can be explained as an ionization fluctuation at the surface[14], the signals of Irganox 1010 fragment ions continue to decrease with the increasing ion fluence and no steady state is reached. This phenomenon can be attributed to chemical damage and/or sputter yield change.

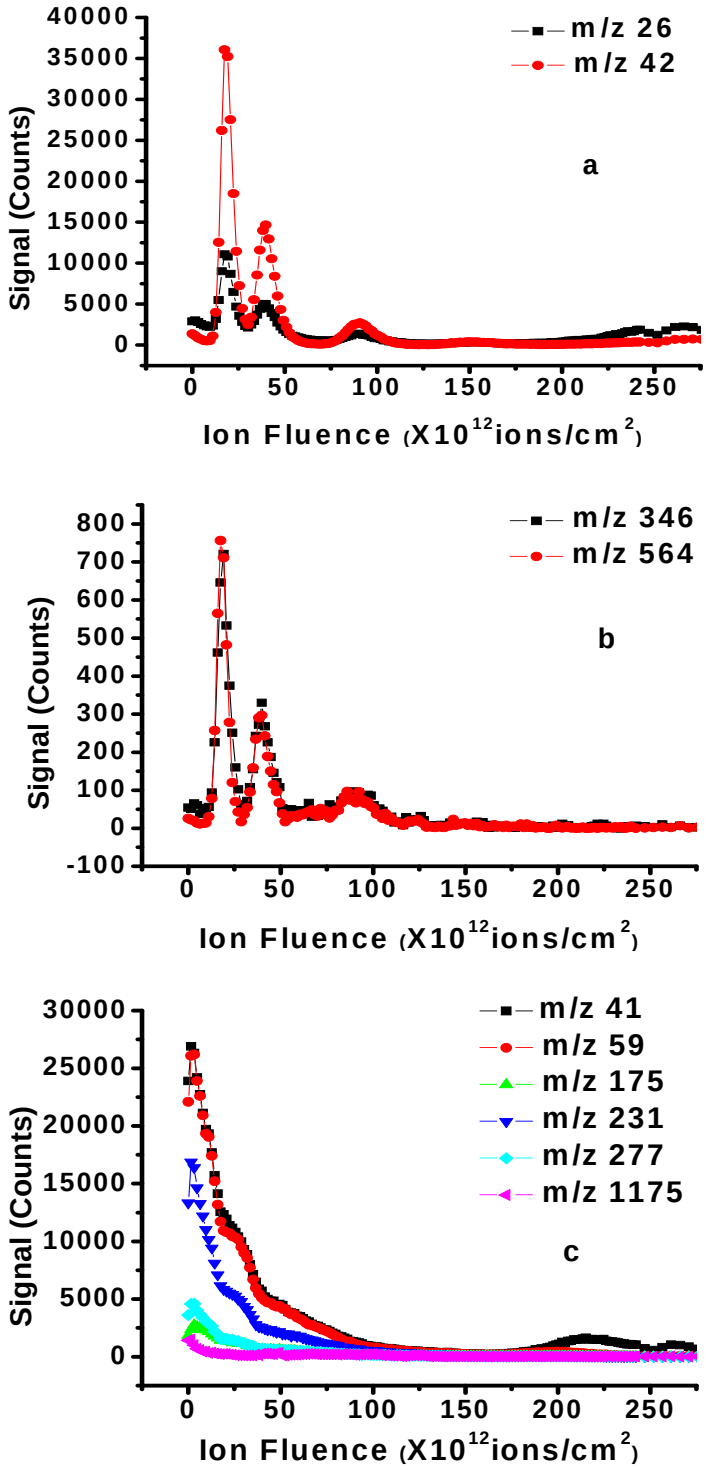

Figure **3-2**: Depth profiles of Irganox delta layer representing (a) low mass ions from Irganox 3114; (b) high mass ions from Irganox 3114; (c) ions from matrix Irganox 1010.

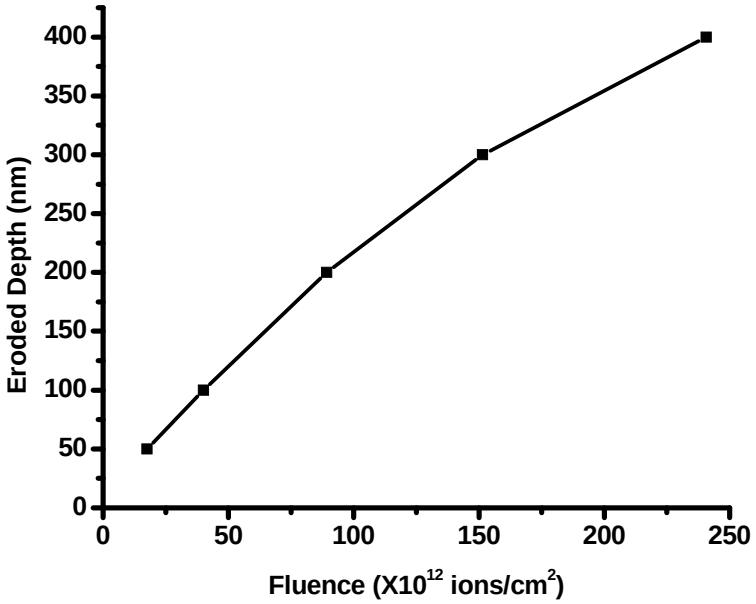

Figure **3-3**: Eroded depth vs. primary ion fluence during depth profiling through a ~400 nm Irganox delta layer sample.

With the layer thickness known, the sputter yield can be evaluated by the ion fluence used to reach each marker layer and the Si substrate. In Figure **3-3**, the eroded depth is plotted against the primary ion fluence at which peak maxima for Irganox 3114 and the substrate interface are found. If the sputter yield was constant, a linear plot should be observed. It is not the case for the data obtained here. The ion fluence required to remove the second 50-nm layer of Irganox 1010 is 30% more than that for the first one. In other words, the average sputter yield drops by 22% for the second Irganox 1010 layer. Moreover, the decrease of sputter yield is more pronounced at a deeper depth. The average sputter yield for the forth layer of Irganox 1010 is only about 55% of the

third one. Apparently, the decrease of the secondary ion signals is related to the decline of the sputter yield.

Since each layer thickness is known, the ion fluence can be converted to a depth scale. The measured full width half maximum (FWHM) from depth profiles is used to represent the depth resolution. The depth resolution measured at the depths of 50 nm and 100 nm using $C_{33}H_{46}N_3O_5^-$ (m/z 564) are 16.8 nm and 20.8 nm. NPL attributed the degradation of the depth resolution to the development of topography.[11]

3.3.2 Repeatability of organic depth profiling

We performed three depth profiling analyses on the same sample on three different days, using the same experimental set up. The repeatability of organic depth profiling is evaluated by three parameters: depth resolution as determined by FWHM, sputter yield, and fluence-integrated raw intensity of the marker layers. Table **3-3** lists the relative standard deviation (RSD) of the parameters representing depth profiling characteristics using the first two distinguishable marker layers.

Table **3-3**: Repeatability of depth profiling characteristics

	RSD		
	FWHM	Sputter Yield	Integrated Peak Intensity
1st marker layer	4%	3%	31%
2nd marker layer	6%	2%	46%

The FWHM value exhibits high repeatability with an RSD of 4%. Since the depth scale is calibrated by layer thickness, the FWHM value is independent and not affected by the measurements of the beam current and the rastering area. Hence, the achieved RSD is better than 10%, which represents good repeatability in the measured depth resolution. The sputter yield also gives excellent repeatability with an RSD less than 5%. The sputter yield calculation is based on the value of beam current, which can only be acquired before and after the depth profile experiment. The small variation of the sputter yield could be caused by the fluctuation in the beam current. The best RSD of integrated intensity is 31%. Although the repeatability of intensity is poor, this does not compromise the measurements of depth resolution and sputter yield as shown in Table **3-3**. The value of the integrated peak intensity is complicated by beam current measurement, the stability of the ion source, and the linearity and reproducibility of the MCP detector. We have already observed that the raw signal intensity changes significantly from day to day, which is mainly caused by the poor reproducibility of the MCP detector. Further optimization of the detector may improve the reproducibility of the intensity value.

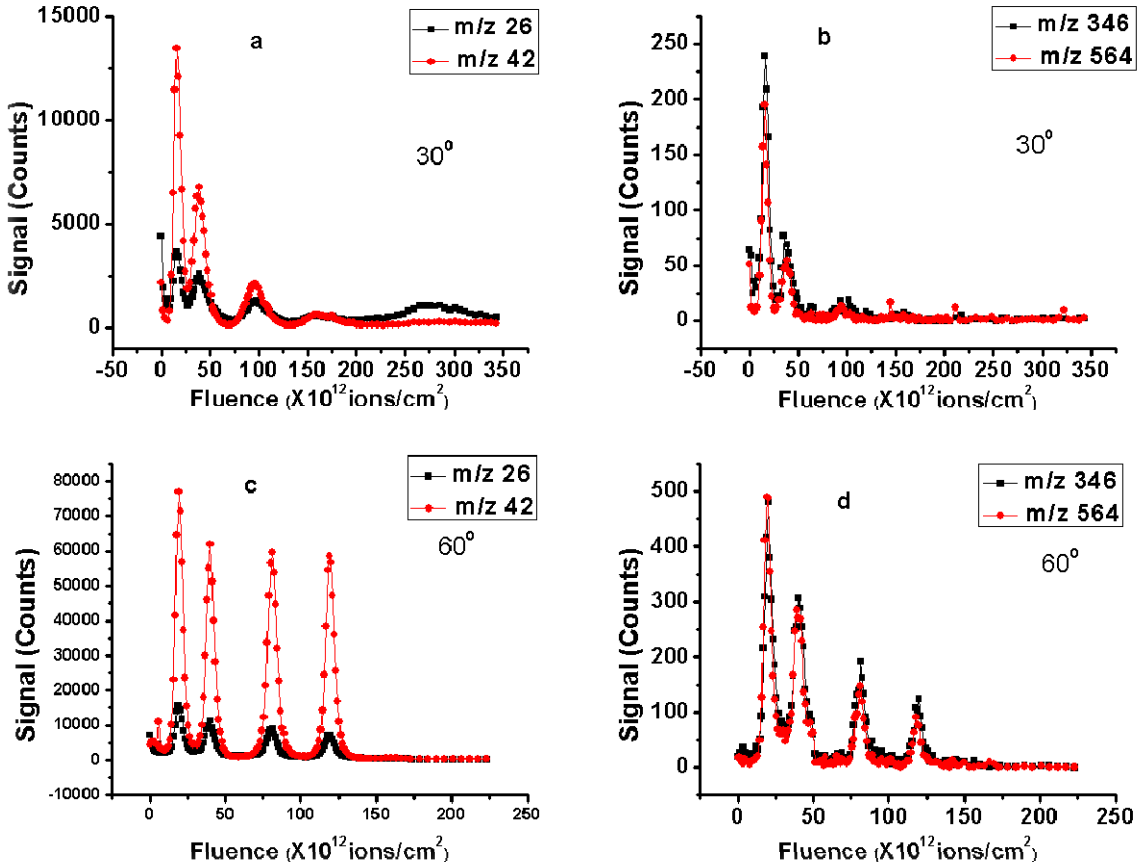

Figure **3-4**: Depth profiles of Irganox delta layer sample at 30^0 (a and b) and 60^0 (c and d) incident angle.

3.3.3 Optimization by incident angle

It is known that the incident angle has an influence on the energy deposition of the primary ions. Molecular dynamics (MD) simulation and experimental data have shown that a grazing angle is able to improve the quality of depth profiling.[15-19] Using a customized sample holder, we can adjust the incident angle of the C_{60}^+ beam on the sample. The depth profiles acquired at 30^0 and 60^0 incident angles are shown in

Figure **3-4**. Comparing Figure **3-4** with Figure **3-2**, we can clearly see that the larger incident angle leads to less signal decay with the increasing ion fluence. This effect is more obvious for low mass ions. Compared to the signal intensity from the first marker layer, the signal maxima of CNO^-(m/z 42) are preserved by 80%, 78% and 76% on the next three marker layers, which is demonstrated by four well-resolved peaks with similar heights in Figure **3-4** (c). Although more signal decline is observed for high mass ions, all marker layers are able to be successfully detected using all four characteristic ions of Irganox 3114 at a 60^0 incident angle.

As discussed earlier, the decrease of sputter yield is one of the causes of secondary ion signal decay. Less signal decay observed at a larger incident angle suggests less decrease of sputter yield, which is verified by the data shown in Figure **3-5**. The eroded depth of the Irganox film by a C_{60}^+ beam at a 60^0 incident angle is plotted against the C_{60}^+ fluence in Figure **3-5**. The exhibited linearity indicates that a constant sputter yield is achieved at a 60^0 incident angle.

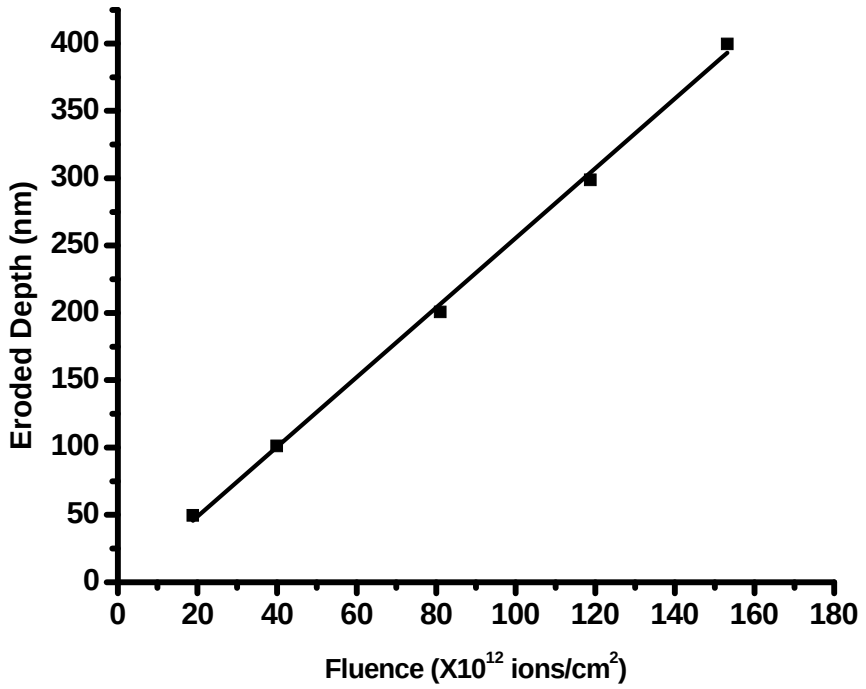

Figure **3-5**: Eroded depth vs. primary ion fluence during depth profiling through ~400 nm Irganox delta layer sample at a 60^0 incident angle.

Increasing incident angle also improved the depth resolution. At a 30^0 incident angle, the FWHM of $C_{33}H_{46}N_3O_5^-$ (m/z 564) from first two marker layers are 19.0 nm and 22.4 nm, worse than the value acquired at a 40^0 incident angle. While with a 60^0 incident angle, the FWHM at the same eroded depth are improved to 14.3nm and 16.9 nm.

3.4 Conclusions

Here we have demonstrated that successful depth profiles of the Irganox delta layer system can be achieved using a 40-keV C_{60}^+ source as both sputter and analysis beam. The advantage of having the C_{60}^+ source as the analysis beam is its ability to

detect molecular ions in high mass region. The observation of molecular ion $[M-H]^-$ of Irganox 1010 at m/z 1175 is unique to the C_{60}^+ source as it has never been seen by atomic beams. For the sample studied, the delta layers located at 50 nm, 100 nm and 200 nm are successfully detected, although the FWHM, signal intensity, and sputter yield are found to decrease with the ion fluence under the daily experimental conditions. The depth profile experiments are reproducible and the results are repeatable for the measurements of depth resolution and sputter yield, which are critical parameters for organic depth profile experiments. Hence, the depth profile analysis of organic materials using a C_{60}^+ source is a reliable technique, providing valuable information to 3-D mass spectral imaging. Currently, research effort is focused on the improvement of depth profiling and 3-D imaging. Optimization of experimental conditions is one of the methods employing currently available instruments. Sample cooling[12,19] and rotation[12] have also been reported to be effective. Here we have shown that depth resolution and prevention of signal decay can be achieved by applying a larger incident angle for the sputtering of an Irganox delta layer system.

3.5 Acknowledgement

Financial support from the National Institute of Health under grant no. 2R01 EB002016-16, the National Science Foundation under grant no. CHE-0908226 and the Department of Energy grant no. DE-FG02-06ER15803 are acknowledged. The authors are grateful to Alex Shard for providing the delta-layer sample.

3.6 References

(1) Castner, D. G. *Nature* **2003**, *422*, 129.

(2) Winograd, N. *Anal. Chem.* **2005**, *77*, 142a.

(3) Walker, A. V. *Anal. Chem.* **2008**, *80*, 8865.

(4) Mahoney, C. M.; Roberson, S. V.; Gillen, G. *Anal. Chem.* **2004**, *76*, 3199.

(5) Cheng, J.; Winograd, N. *Analytical Chemistry* **2005**, *77*, 3651.

(6) Wucher, A.; Cheng, J.; Winograd, N. *J. Phys. Chem. C* **2008**, *112*, 16550.

(7) Mahoney, C. M.; Fahey, A. J.; Gillen, G. *Anal. Chem.* **2007**, *79*, 828.

(8) Shard, A. G.; Brewer, P. J.; Green, F. M.; Gilmore, I. S. *Surf. Interface Anal.* **2007**, *39*, 294.

(9) Mahoney, C. M.; Fahey, A. J.; Gillen, G.; Xu, C.; Batteas, J. D. *Appl. Surf. Sci.* **2006**, *252*, 6502.

(10) Mahoney, C. M.; Fahey, A. J.; Gillen, G.; Xu, C.; Batteas, J. D. *Anal. Chem.* **2007**, *79*, 837.

(11) Shard, A. G.; Green, F. M.; Brewer, P. J.; Seah, M. P.; Gilmore, I. S. *J. Phys. Chem. B* **2008**, *112*, 2596.

(12) Sjovall, P.; Rading, D.; Ray, S.; Yang, L.; Shard, A. G. *J. Phys. Chem. B* **2010**, *114*, 769.

(13) Braun, R. M.; Blenkinsopp, P.; Mullock, S. J.; Corlett, C.; Willey, K. F.; Vickerman, J. C.; Winograd, N. *Rapid Commun. Mass Spectrom.* **1998**, *12*, 1246.

(14) Cheng, J.; Wucher, A.; Winograd, N. *J. Phys. Chem. B* **2006**, *110*, 8329.

(15) Kozole, J.; Willingham, D.; Winograd, N. *Appl. Surf. Sci.* **2008**, *255*, 1068.

(16) Ryan, K. E.; Smiley, E. J.; Winograd, N.; Garrison, B. J. *Appl. Surf. Sci.* **2008**, *255*, 844.

(17) Garrison, B. J.; Postawa, Z.; Ryan, K. E.; Vickerman, J. C.; Webb, R. P.; Winograd, N. *Anal. Chem.* **2009**, *81*, 2260.

(18) Kozole, J.; Wucher, A.; Winograd, N. *Anal. Chem.* **2008**, *80*, 5293.

(19) Zheng, L. L.; Wucher, A.; Winograd, N. *Anal. Chem.* **2008**, *80*, 7363.

Chapter 4

Fundamental Studies of Molecular Depth Profiling Using Organic Delta-layers as Model Systems

This chapter has been reproduced with permission from C. Lu, A. Wucher and N. Winograd, *Surface and Interface Analysis* (2010). This paper was submitted as a proceeding paper for SIMS XVII and has been expanded for further clarification.

4.1 Introduction

Cluster projectiles have expanded potential applications of secondary ion mass spectrometry (SIMS) for materials characterization.[1] By combining molecular depth profiling with SIMS imaging, 3-D imaging is feasible, which will provide valuable information about biological samples.[2-3] Hence, it is important to investigate the factors affecting achievable depth resolution, especially for organic-organic interfaces. Since Langmuir-Blodgett (LB) films have a well-defined structure and sharp interfaces between layers, we have employed multilayer films of barium arachidate (AA) and barium dimyristoyl phosphatidate (DMPA) to study the fundamentals of molecular depth profiling.[4-5] Here we synthesize a 4.4 nm layer of DMPA embedded in two ~50 nm multilayer stacks of AA on a bare silicon wafer to create a delta-layer model system for characterization with a C_{60}^+ probe. As demonstrated by Shard *et al*.[6-8], such systems are ideally suited to investigate the depth profiling characteristics of organic films in the

same way as has been done for many years in inorganic sputter depth profiling. The measured depth response function is analyzed in terms of quasi-exponential leading and trailing edges connected by a central Gaussian function as suggested by Dowsett.[9] In order to determine the influence of bombardment induced topography formation on the measured depth resolution, the surface roughness is studied both at the original film and after sputter erosion down to the delta layer. Comparison of the surface topography data with the measured depth response function shows that ion induced mixing at the organic-organic interface is the dominate factor determining the apparent depth resolution for this system.

4.2 Experimental Section

The preparation of the LB films has been described in detail elsewhere.[5] A single crystal (100) silicon wafer was used as the substrate. The substrates were treated with ozone for 10 min and rinsed with high purity water several times to ensure hydrophilicity of the Si/SiO_2 surface. A Kibron μTrough S-LB (Helsinki, Finland) was used for multilayer LB film preparation. A bilayer of DMPA was embedded between two stacks of AA, 51 nm and 54 nm respectively. The film thickness was measured by a KLA-Tencor Nanopics 2100 atomic force microscope (AFM). The films are stable in ambient conditions for over 6 months as indicated by their color, mass spectra and depth profiles. The surface roughness after sputter depth profiling was measured by AFM operated in tapping mode. Topography images were taken within 15 min, 30 min, 1 hour and 1 day

sequentially after the depth profile analysis and no significant difference in topography was found as a function of time after sputtering.

Sputter depth profiling was performed in a ToF-SIMS instrument equipped with a fullerene cluster ion source (IOG 40-60, Ionoptika; Southampton, U.K.), directed at a 40^0 angle relative to the surface normal. Details of this instrumentation have been described elsewhere.[10] The source was operated with a focused (~7 μm diameter) 40-keV C_{60}^+ ion beam. For depth profiling, the C_{60}^+ ion beam was operated in DC mode to erode through the film at an area of 400 μm × 500 μm in 3s intervals. Between erosion cycles, SIMS images with 256 × 256 pixels were acquired from the same area using the pulsed C_{60}^+ projectile beam at an ion fluence of 10^{10} ions/cm^{-2}, and ToF mass spectra were retrospectively extracted from the image data from an area of 300 μm × 400 μm inside the sputtered region.

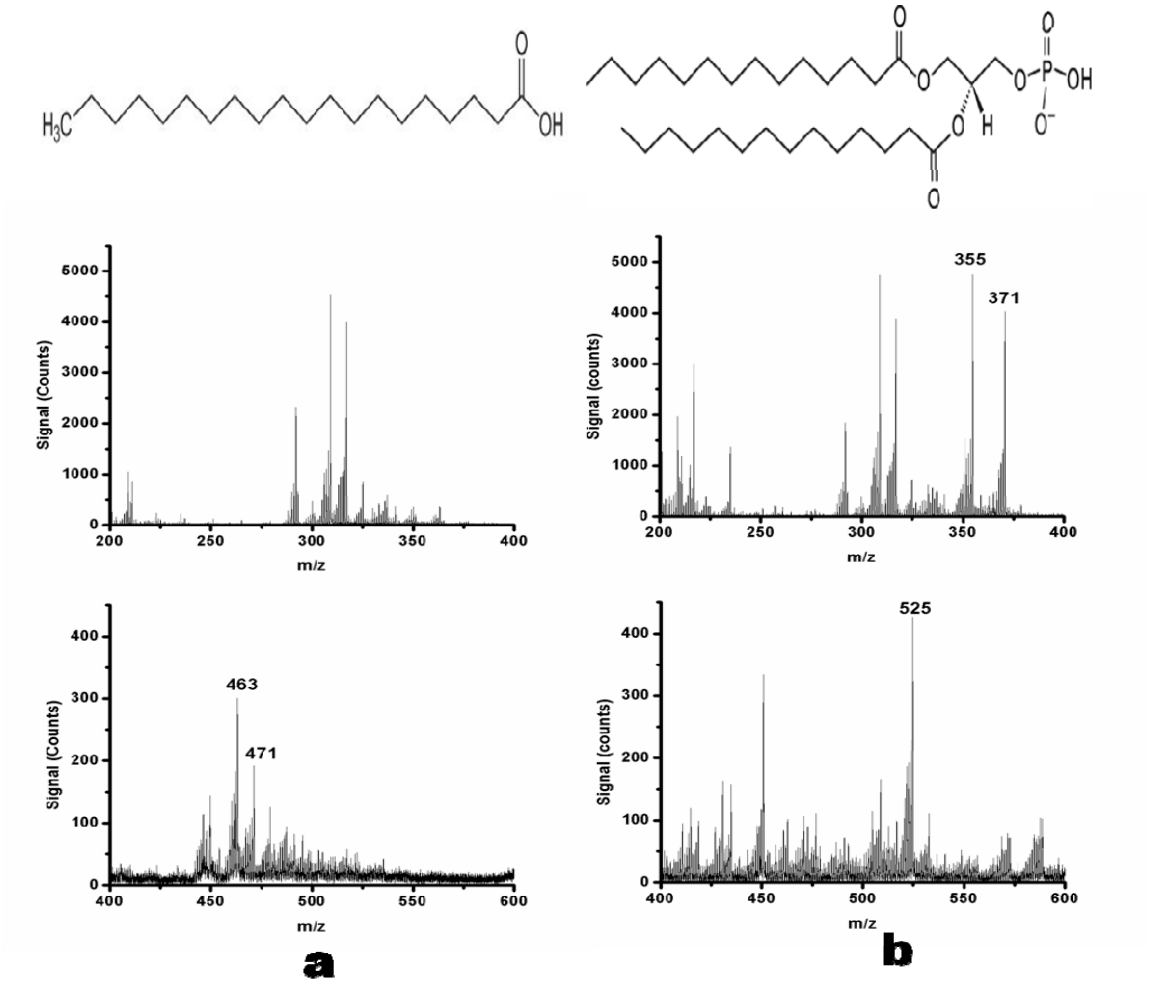

Figure **4-1**: Chemical structures and C_{60}^{+}-SIMS spectra of (a) AA and (b) DMPA.

4.3 Results and Discussion

4.3.1 Characterization of LB delta layer by depth profiling

The chemical structure and mass spectra of AA and DMPA are shown in Figure **4-1**. As with our previous studies on this system[4], the molecule specific signals at m/z 463 and 525 were used to represent the AA and DMPA films, respectively. In

addition, fragment ion peaks were analyzed at m/z 355 and 371 which are found to be specific for DMPA as well. The dependence of relevant secondary ion signals on the fluence of the eroding C_{60}^{+} ion beam is shown in Figure **4-2**. As described earlier, the peaks detected at the DMPA specific masses contain contributions arising from AA as well.[4] To correct for any interfering intensity, the ratio of m/z 355, 371 and 525 respectively to the m/z 463 peak was averaged in the region where no DMPA is present. Corrected intensities of DMPA were calculated by subtracting background from AA using these ratios and the m/z 463 signal while profiling through the DMPA film.

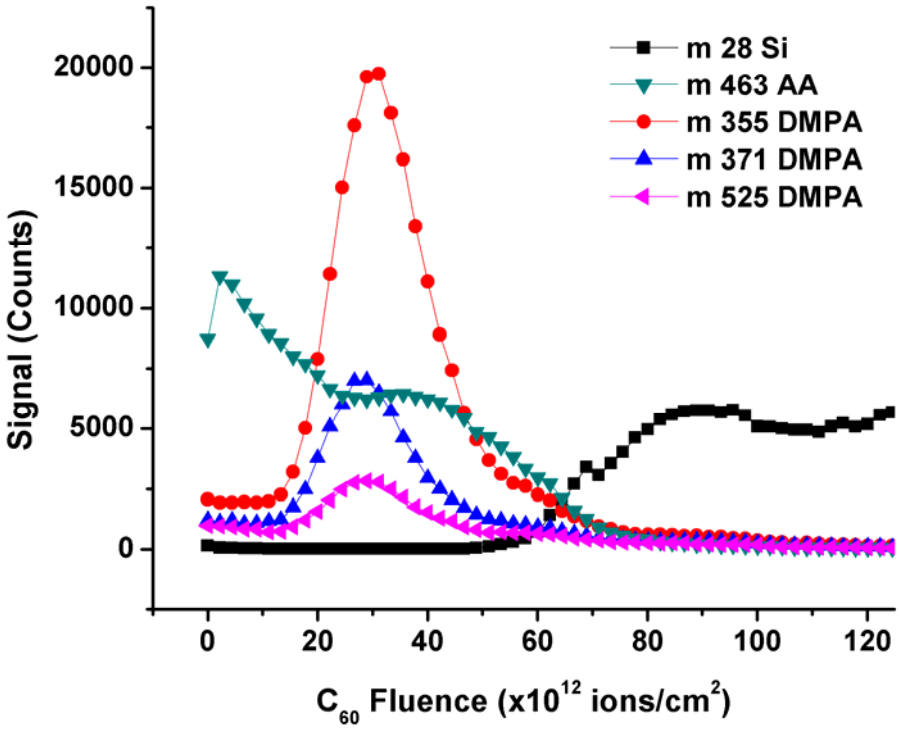

Figure **4-2**: Secondary ion signals representing AA and DMPA vs. fluence of the eroding C_{60}^{+} ion beam.

In order to convert the projectile ion fluence into eroded depth, a protocol was invoked which involves a linear interpolation of the erosion rate between values determined for pure AA and DMPA films, respectively. The momentary erosion rate was calculated as in Eq. **4.1**

$$\frac{dz}{df} = \frac{S_{DMPA}}{S_{DMPA}^{\max}} \frac{dz}{df}\Big|_{DMPA} + \left(1 - \frac{S_{DMPA}}{S_{DMPA}^{\max}}\right) \frac{dz}{df}\Big|_{AA} \qquad \text{[Eq. 4.1]}$$

using the background-corrected DMPA signal (m/z 525) along with its maximum value in the delta layer. From the previously determined ratio between the erosion rates $\dot{z}_{DMPA} / \dot{z}_{AA}$ =0.75, under the bombardment conditions applied here yields Eq. **4.2,**

$$\frac{dz}{df} = \left(1 - 0.25 \frac{S_{DMPA}}{S_{DMPA}^{\max}}\right) \frac{dz}{df}\Big|_{AA} \qquad \text{[Eq. 4.2]}$$

which was used to determine the pure AA erosion rate value from the known film thickness and the fluence needed to erode the entire film. The interface to the underlying Si substrate was identified by the point where the AA signal had decreased to 50% of its value throughout the removal of the DMPA-doped film.

The background subtracted signals characterizing the DMPA delta layer are shown as a function of eroded depth in Figure **4-3**. For better comparison, the signals have been normalized to their respective maximum. As expected from the film deposition process, the signal maxima are found at a depth of about 56 nm. The half width of the signal response function is determined as ~29 nm. This value is much larger than the real width of the delta layer (4.4 nm) and therefore characterizes the depth resolution of the experiment.

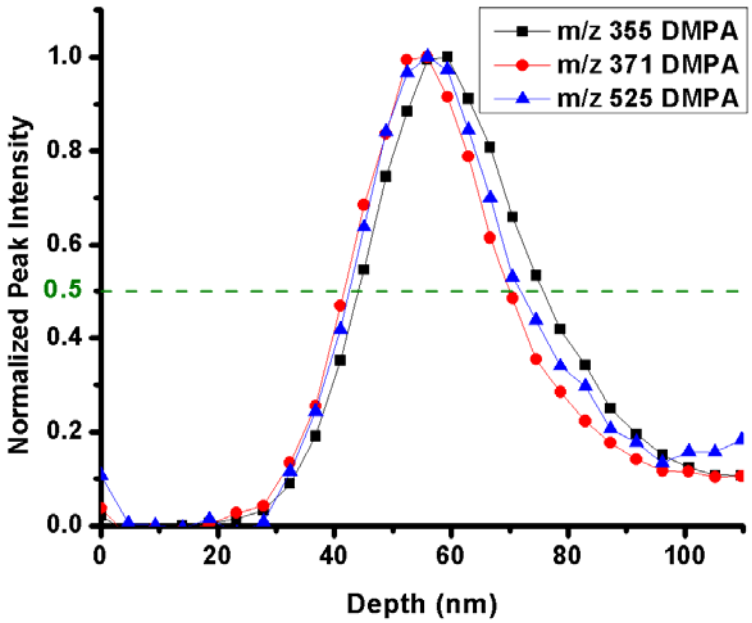

Figure **4-3**: Secondary ion signals representing the DMPA delta layer normalized to the respective signal maxima (after subtraction of AA induced background) vs. eroded depth.

It is interesting to note that neither the maxima nor the half width of the three signals representing the DMPA layer exactly coincide. As shown in Table **4-1**, there is a trend that the signal peaks at larger depth and exhibits a smaller half width with decreasing size of the characteristic molecular fragment. We speculate that the reason for this behavior is that fragment signals may lag behind the molecular ion signal, since a threshold ion fluence may be required to build up the damage that produce the detected fragment ions once the delta layer is reached.

Table **4-1**: Characteristic parameters characterizing the depth response function for a 4.4-nm DMPA delta layer embedded in an AA matrix. All values given in nm.

m/z	max	FWHM	λ_g	λ_d	σ	z_0
355	57.5	28.4	4.8	17.0	8.3	53.9
371	55.9	29.4	4.8	15.0	7.5	51.3
525	54.1	31.4	5.0	16.9	7.4	51.8
ave	55.8 ± 1.7	29.7 ± 1.5	4.9 ± 0.1	16.3 ± 1.1	7.7 ± 0.5	52.3 ± 1.4

4.3.2 Quantitative analysis by Dowsett's function

In order to analyze the depth response function in more detail, a logarithmic plot of DMPA signals is shown in Figure **4-4**. It is seen that the signal response contains exponential leading and trailing edges connected by a rounded top. Response functions of this kind are generally observed during sputter depth profiling of delta dopant structures in semiconductors.[9] They can be described by Dowsett's semi-empirical function[9] as in Eq. **4.3**

$$R(z') = N\left[\left(1-erf\left(\xi_1\right)\right)\exp\left(\frac{z'}{\lambda_g}+\frac{\sigma^2}{2\lambda_g{}^2}\right)+\left(1+erf\left(\xi_2\right)\right)\exp\left(\frac{z'}{\lambda_d}-\frac{\sigma^2}{2\lambda_d{}^2}\right)\right] \qquad \text{[Eq. 4.3]}$$

with $\xi_1 = \frac{1}{\sqrt{2}}\left(\frac{z'}{\sigma}+\frac{\sigma}{\lambda_g}\right)$ and $\xi_2 = \frac{1}{\sqrt{2}}\left(\frac{z'}{\sigma}-\frac{\sigma}{\lambda_d}\right)$, where λ_g and λ_d are the leading and trailing edge growth and decay lengths, while σ denotes the standard deviation of a central Gaussian connecting the two exponential functions. The depth z' is referenced to the original position z_0 of the delta layer, which in our case should be located at a depth of 56 nm below the surface.

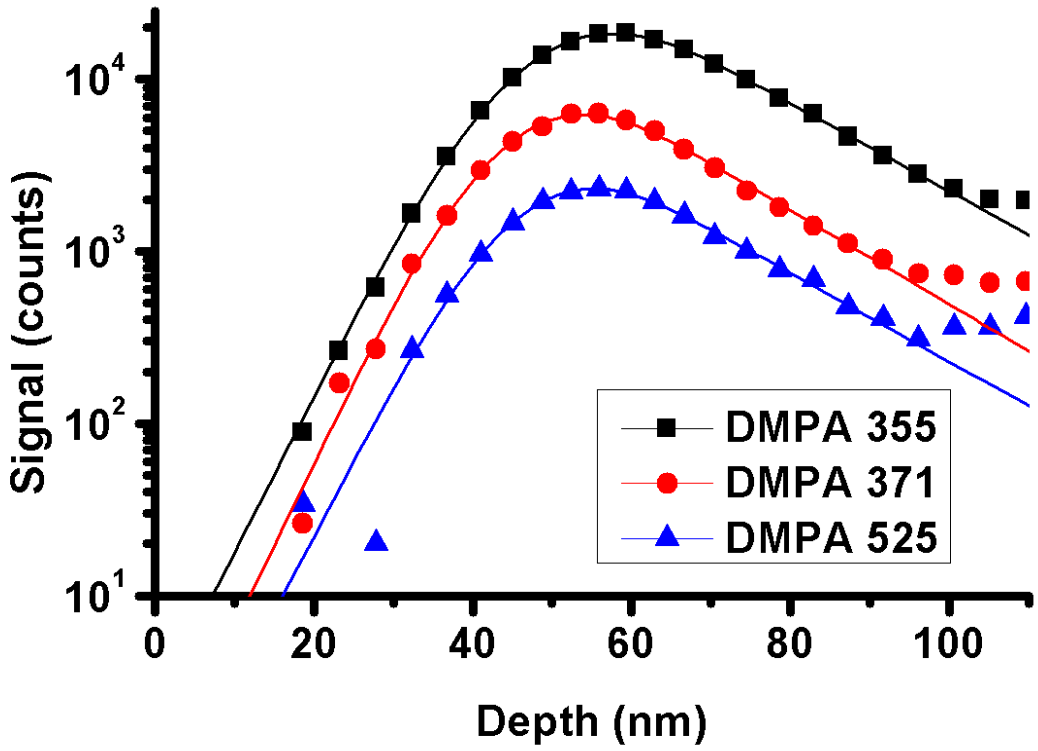

Figure **4-4**: Secondary ion signals representing the DMPA delta layer (after subtraction of AA induced background) vs. eroded depth. The solid lines represent least square fits of the Dowsett delta response function[9] to the data.

In order to extract the parameters λ_g, λ_d and σ for the DMPA delta layer studied here, Eq. **4.3** was fit to the measured signal response. The resulting curves are shown in Figure **4-4**, and the corresponding parameters are listed in Table **4-1**. All three measured DMPA signals yield similar parameters, with the leading edge consistently being steeper than the trailing edge. The leading edge slope is generally believed to reflect the escape depth of the detected sputtered particles.[9, 11] Our data therefore suggest an effective escape depth of ~5 nm, which reflects both the information depth of a static SIMS spectrum and the statistical nature of the sputtering process during ion beam erosion.[12]

The trailing edge is determined by the differential escape rate of dilute analyte molecules (DMPA) in the matrix (AA).[13] One can use the erosion dynamics model[14, 15] to predict Eq. **4.4**

$$\lambda_d = d \cdot \frac{Y^{tot}}{Y_0^a + nd\sigma_D} \qquad \text{[Eq. 4.4]}$$

where n, d and σ_D denote the molecule density, altered layer thickness and damage cross section, Y^{tot} is the total sputter yield (i.e. that of the pure AA matrix), and $Y_0^a \cdot c_s^a$ describes the partial sputter yield of DMPA analyte molecules. In the absence of preferential sputtering (i.e., $Y_0^a = Y^{tot}$), the trailing edge should therefore reflect the altered layer thickness corrected by the cleanup efficiency $\varepsilon = Y^{tot} / nd\sigma_D$ as in Eq. **4.5**.

$$\lambda_d = d \cdot \frac{\varepsilon}{1+\varepsilon} \qquad \text{[Eq. 4.5]}$$

With typical values of $\varepsilon \sim 1$ being reached under C_{60} bombardment, a trailing edge decay length of 16 nm would therefore correspond to an altered layer thickness of the same order, which has indeed been observed.[14]

4.3.3 Evaluation of ion beam induced surface roughening

The central Gaussian reflects a convolution of the original layer thickness and other effects influencing the depth resolution like bombardment induced surface topography.[9] Note that 2.2 nm of the average σ reported in Table **4-1** arise from the intrinsic width of the delta layer, leaving at most 5 nm for surface roughening effects. A topography image taken at the depth corresponding to the DMPA signal maximum is

shown in Figure **4-5**. The rms roughness obtained from this image is indeed about 5 nm. However, this value is only slightly larger than that measured at the original surface (3.5 nm, as in Figure **4-5** (a)), indicating that the bombardment induced roughening effect is actually much smaller. In any case, it is evident that surface microtopography is not the dominating factor determining the depth resolution observed for the system studied here.

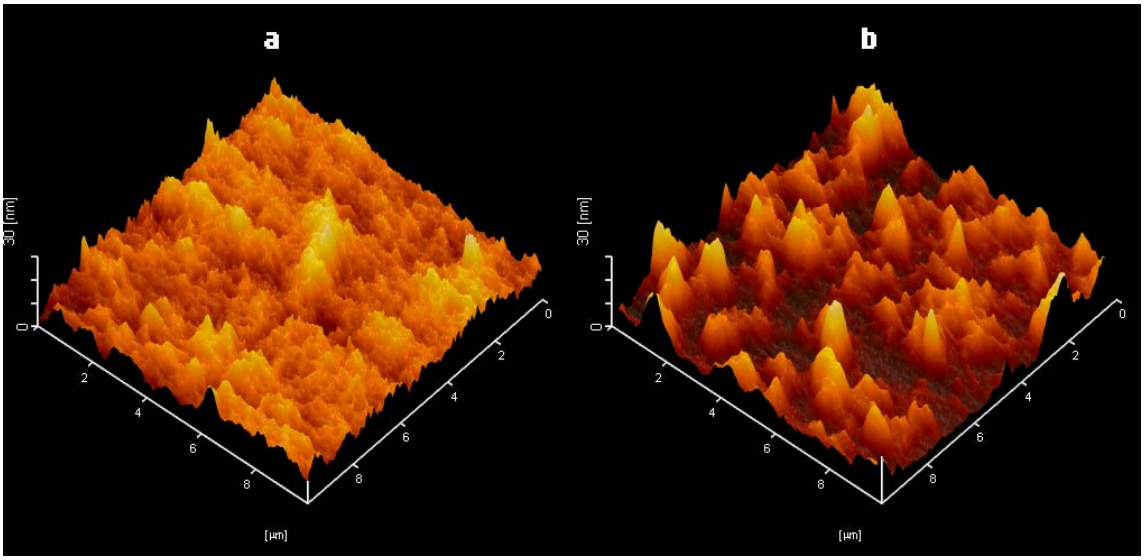

Figure **4-5**: (a) AFM image taken at the original film surface; (b) AFM image of the crater bottom taken at the depth of the signal maxima visible in Figure **4-3**.

4.4 Conclusions

Using LB multilayer stacks, an organic delta layer model system has been designed and depth profiled by a 40-keV C_{60}^+ ion beam. The depth resolution obtained for this system is somewhat larger (28 nm vs 18 nm) than that reported for the irganox delta-layer system which has been examined recently[7] and used as a reference material in a VAMAS interlaboratory study[16]. These differences suggest that the molecular

properties of the organic material are important in controlling the sputtering dynamics and the resulting ion beam mixing. The LB model is particularly interesting since it closely resembles the structure of a biological membrane layer and hence provides some indication of how successful 3-D imaging experiments will be for these types of systems.

4.5 Acknowledgement

Financial support from the National Institute of Health under grant no. 2R01 EB002016-16, the National Science Foundation under grant no. CHE-0908226 and the Department of Energy grant no. DE-FG02-06ER15803 are acknowledged.

4.6 References

(1) Winograd, N. *Anal. Chem.* **2005**, *77*, 142a.

(2) Fletcher, J. S.; Lockyer, N. P.; Vaidyanathan, S.; Vickerman, J. C. *Anal Chem* **2007**, *79*, 2199.

(3) Nygren, H.; Hagenhoff, B.; Malmberg, P.; Nilsson, M.; Richter, K. *Microsc Res Techniq* **2007**, *70*, 969.

(4) Zheng, L. L.; Wucher, A.; Winograd, N. *J. Am. Soc. Mass Spectrom.* **2008**, *19*, 96.

(5) Zheng, L. L.; Wucher, A.; Winograd, N. *Anal. Chem.* **2008**, *80*, 7363.

(6) Shard, A. G.; Brewer, P. J.; Green, F. M.; Gilmore, I. S. *Surf. Interface Anal.* **2007**, *39*, 294.

(7) Shard, A. G.; Green, F. M.; Brewer, P. J.; Seah, M. P.; Gilmore, I. S. *J. Phys. Chem. B* **2008**, *112*, 2596.

(8) Sjovall, P.; Rading, D.; Ray, S.; Yang, L.; Shard, A. G. *J. Phys. Chem. B* **2010**, *114*, 769.

(9) Dowsett, M. G.; Rowlands, G.; Allen, P. N.; Barlow, R. D. *Surf. Interface Anal.* **1994**, *21*, 310.

(10) Cheng, J.; Winograd, N. *Anal. Chem.* **2005**, *77*, 3651.

(11) Andersen, H. H. *Appl Phys* **1979**, *18*, 131.

(12) Krantzman, K. D.; Wucher, A. *J. Phys. Chem. C* **2009**.

(13) Wittmaack, K. *Vacuum* **1984**, *34*, 119.

(14) Cheng, J.; Wucher, A.; Winograd, N. *J. Phys. Chem. B* **2006**, *110*, 8329.

(15) Wucher, A. *Surf. Interface Anal.* **2008**, *40*, 1545.

(16) Shard, A. G.; Foster, R.; Gilmore, I. S.; Lee, J. L. S.; Ray, S.; Yang, L. *Surf. Interface Anal.* **2010**, DOI: 10.1002/sia.3268.

Chapter 5

Molecular Depth Profiling of Buried Lipid Bilayers Using C_{60}-SIMS

This chapter has been submitted as a research article to *Analytical Chemistry*.

5.1 Introduction

Cluster ion beams have begun to play a leading role in organic materials characterization by means of secondary ion mass spectrometry (SIMS) due to the enhanced sputter yield, larger secondary ion yield and lower chemical damage produced by these projectiles. Since cluster ions are able to remove the material without destroying its chemical integrity, molecular depth profiling has been successfully performed on various materials.[1-8] Successive 2-D SIMS molecular images can be obtained after sample erosion to different depths by cluster beams, thereby allowing 3-D mapping of specific molecules. This method is feasible for biological samples and is providing valuable 3-D chemical information in biological tissues and single cells.[9-11]

Construction of 3-D molecular ion images requires that some basic issues be sorted out. Fundamental studies are focused on the ion-solid interaction and the physical properties of the sputtering process. Various experimental conditions have been shown to influence these processes and affect the molecular depth profiles and 3-D imaging results, like temperature of the bombarded sample as well as incident angle and energy of the impinging projectiles. Constant molecular secondary ion signals were observed

during depth profiles of spin coated trehalose[2] and biodegradable polymer films[12] at room temperature, while there are also other samples where the steady state can only be reached at low temperature.[7,13,14] Depth profiles on cholesterol thin films reveal that the incident angle of projectiles changes the energy deposition characteristics and has a significant influence on depth profiles.[8] The kinetic energy of the primary ion beam controls the energy deposition as well. Analysis of the available experimental data has shown that the success of a molecular depth profile experiment is largely determined by a competition between bombardment induced chemical damage on one hand and sputter removal of (damaged or undamaged) material on the other hand. In short, molecule specific secondary ion signals can be maintained and followed during ion erosion if the sputtering process removes most of the material damaged by the ion impact. Comparison between different cluster ions has shown that this "cleanup" mechanism appears to be most efficient for buckminsterfullerene (C_{60}) projectiles.[15-17]

Depth resolution is a key factor to evaluate molecular depth profiling and 3-D imaging. This property can in principle be evaluated from the observed interface width of secondary ion signal characteristics for successive sample layers, or from the signal response to a so-called "delta layer" of negligible width. So far, various depth resolution values measured in different ways have been reported, which range from 3 nm to 30 nm.[2,14,18,19] Probably the best method to characterize the depth resolution is the analysis of a delta layer, i.e., a layer of negligible width embedded in a similar matrix material. Measuring the signal response while profiling across such a layer then directly delivers the depth response function of the method, a concept which has been routinely used in SIMS depth profiling of inorganic material for many years.[20-21] In order to provide a

similar standard for molecular depth profiling, it is therefore highly desirable to design molecular delta layer samples as well. The first successful attempt in this direction was made at NPL (National Physical Laboratory, Middlesex, U.K.), where a delta layer system was designed by alternative vapor deposition of Irganox 1010 (the matrix material) and Irganox 3114 (the delta layer) onto a silicon substrate. This sample has been recently utilized as a standard system in an interlaboratory study on molecular depth profiling, and the results have provided much insight into the factors determining the observed depth resolution. One of the key results of this study has been the observation that both the sputter yield and depth resolution decay with ion fluence. More specifically, atomic force microscopy (AFM) data suggest that surface topography developing during C_{60} ion beam erosion is the main cause of the degradation of depth resolution.[19] It was also demonstrated that sample cooling[14,22] or sample rotation[22] during ion erosion can be effective in reducing these effects and improving the quality of organic depth profiling.

High lateral resolution of SIMS makes 3-D imaging of single cells an appealing application of this technique. Molecular dynamics (MD) simulation of the sputtering of different materials indicates that the molecular structure has a critical influence on the sputtering process.[23] Therefore, it is necessary to investigate the factors affecting achievable depth resolution on different biological materials. Langmuir Blodgett (LB) monolayers made of lipids and fatty acids have been widely studied as cell membrane models and appear to be quite suitable for SIMS analysis.[24-28] Multilayer LB films have well-defined structures and sharp interfaces between layers and have been employed to study the fundamentals of molecular depth profiling.[7,14,29] In this work, we synthesized a 4.4 nm bilayer of barium dimyristoyl phosphatidate (DMPA) embedded in relatively

thick (51~105 nm) multilayer stacks of barium arachidate (AA) on a bare silicon wafer to create a delta-layer model system for the characterization of this type of material as well. As outlined above, such systems are well-suited to investigate the depth profiling characteristics of organic films. The measured depth response function is analyzed in terms of quasi-exponential leading and trailing edges connected by a central Gaussian function as suggested by Dowsett.[20] In order to determine the influence of ion bombardment induced topography formation on the measured depth resolution, the surface roughness is studied both at the original film and after sputter erosion down to different depths. Comparison of the surface rms roughness data with the measured depth response function shows that for this system, surface topography development is of minor importance, while ion induced mixing at the organic-organic interface is the dominating factor determining the apparent depth resolution. Cooling the sample to cryogenic temperature during the analysis is shown to reduce the mixing effects and prevent chemical damage accumulation. The influence of beam energy and incident angle was also investigated and the results show consistent with previous studies, that the best depth resolution is obtained with lower beam energy at glancing impact angle. The delta layer made of a DMPA bilayer closely resembles the structure of a biological membrane and will hopefully provide a useful model for 3-D imaging of single cells.

5.2 Experimental section

Arachidic acid, barium chloride (99.999%), copper (II) chloride, potassium hydrogen carbonate (99.7%) and all solvents were purchased from Sigma-Aldrich

(Allentown, PA). The DMPA was purchased from Avanti Polar Lipids (Alabaster, AL). All chemicals were used without any further purification. Water used in preparation of LB films was obtained from a Nanopure Diamond Life Science Ultrapure Water System (Barnstead International, Dubuque, IA) and had a resistivity of at least 18.2 MΩ·cm.

Single crystal (100) silicon wafers were used as the substrate. The Si substrates were cleaned by ozone for 10 min and then rinsed with high purity water several times to ensure hydrophilicity of the Si/SiO_2 surface. A Kibron μTrough S-LB (Helsinki, Finland) was used for isotherm acquisition and multilayer LB film preparation. Details of the LB film preparation have been described elsewhere.[7] The applied subphase was 70 mL aqueous solution of 10^{-4} M $BaCl_2$, 10^{-3} M $KHCO_3$ and 10^{-7} M $CuCl_2$. $BaCl_2$ was added to the solution to form salt with arachidic acid and DMPA at pH 7 which was controlled by addition of $KHCO_3$. The presence of $CuCl_2$ helped to enhance film stability after construction of a large number of layers. Monolayers of AA and DMPA at the air-water interface were aged for 30 min and compressed at a constant rate of 7 $Å^2$/molecule/min. The monolayer was transferred onto the Si substrate by vertical deposition at the rate of 10 mm/min when the surface pressure was kept constant at 33 mN/m. Approximately 10 min was allotted between successive film deposition cycles for substrate drying. Three types of delta layer samples were prepared. One has a single bilayer of DMPA (4.4 nm) deposited between 51 and 54 nm AA stacks. The second one has two sets of DMPA bilayers (4.4 nm) separately embedded in 305 nm AA stacks. The third one has two blocks of DMPA with different thickness (8.8 nm of 4 DMPA monolayers and 4.4 nm of 2 DMPA monolayers) separated by ~100 nm AA stacks.

The depth profile experiments were performed on a ToF-SIMS instrument, which has been described previously.[7] The sample stage can be cooled to 100 K, so depth profile experiments can be run at liquid nitrogen temperature. A 40-keV C_{60} source (IOG 40-60, Ionoptika; Southampton, U.K.) is mounted to the instrument at an angle of 40^0 with respect to the surface normal. The kinetic energy of the singly charged C_{60}^+ primary ion beam could be varied between 20 and 40 keV. Under typical conditions, the beam current is 150~200 pA and the beam size is 7~10 μm. The incident angle could be altered to 71^0 using a customized wedge-shaped sample block. The mass spectrometer was operated in a delayed extraction mode with 50 ns delay time between the primary ion pulse and the secondary ion extraction pulse. Charge compensation was found to be unnecessary during positive ion SIMS mode due to a charge balance between primary and secondary ion currents. For depth profiling, the C_{60}^+ ion beam was operated in DC mode to erode through the film at an area of $\Delta x \cdot \Delta y$ with $\Delta y = \Delta x/\cos\theta$ and Δx ranging from 300 to 500 μm (θ is the impact angle of the primary beam relative to the surface normal). Between erosion cycles, SIMS images were acquired from the same area using the pulsed C_{60}^+ projectile beam with a total ion fluence below 10^{11} cm^{-2}. A digital raster scheme with 256 × 256 pixels was employed during both the erosion and data acquisition cycles, which corresponds to a pixel step size (1-2 μm) well below the beam width. The ToF mass spectra were retrospectively extracted from various pixel areas of the image data in order to investigate crater edge effects and determine the optimum gating area as described elsewhere.[30] No edge effects were observed at the central area of 192 × 192 pixels inside the sputtered region, therefore mass spectra from these areas were used for depth profile analysis. For the depth profile experiments at a 71^0 incident angle, the

extraction electrical field was distorted because the sample was mounted on a wedge-shaped sample block during data acquisition, resulting in lower secondary ion extraction efficiency. Therefore, when the primary ion beam is rastered over a larger area, only the secondary ions emitted from the central stripe area can be detected. This influence doesn't affect the ion intensity we used for depth profile analysis since the analysis area is within the stripe region.

An AFM (Nanopics 2100, KLA-Tencor, San Jose, CA) was used to characterize the film thickness, the eroded crater depth and the surface roughness. Film thickness and crater depth were measured in contact mode, while surface roughness data were acquired within a 10 μm × 10 μm area in tapping mode. Since the AFM data were measured after the depth profile experiment was completed and the sample was taken out of the vacuum system, surface relaxation after ion bombardment is possible. In order to examine this influence, topography images were taken within 15 min, 30 min, 1 hour and a day sequentially after the depth profile analysis and no significant difference in topography was found during this timescale after sputtering. The thickness of the LB monolayer was determined by a single wavelength (632.8nm, 1-mm spot size, 70^0 angle of incidence) Stokes ellipsometer (Gaertner Scientific Corp., Skokie, IL; mode LSE).

5.3 Results and discussion

Previous work has shown that LB delta layers represent a good model system to study the depth resolution of molecular depth profiling and 3-D imaging experiments of biological materials.[31] The objective of this work is to evaluate factors that determine the

depth resolution and investigate the role of various experimental parameters controlling the sputter process. The molecule specific signals at m/z 355, 371 and 525 are found to be representative peaks of DMPA. The AA film is characterized by a molecule specific signal at m/z 463. The intensities of DMPA were corrected by the method used previously[31] to deduce the signals contributed by AA. All three measured signals from DMPA exhibit a similar shape. Hence, only signals at m/z 355 are shown here for simplicity.

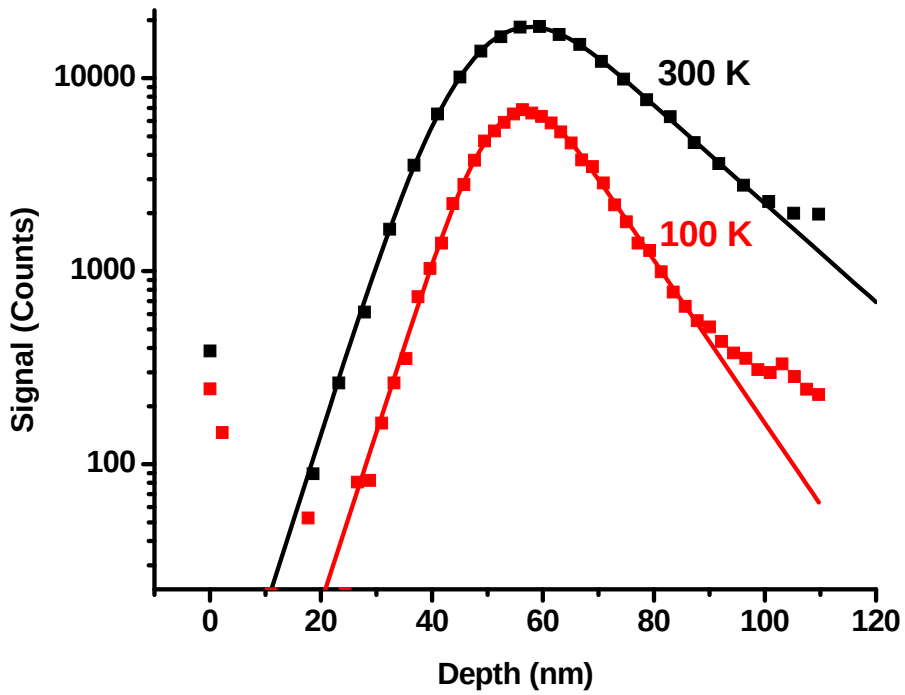

Figure **5-1**: Depth profiles of single delta layer sample at 300 K and 100 K with 40-keV C_{60}^{+} at a 40^{0} incident angle.

5.3.1 Effects of sample temperature

The signal response, i.e., the m/z 355 signal as a function of eroded depth, arising from a single DMPA delta layer is shown in Figure **5-1**. The depth scale was calibrated using the strategy employed previously.[31] In order to elucidate the temperature effect, data obtained at 100 K and 300 K are compared. Both traces exhibit the typical shape observed in depth profiling of delta dopant structures in semiconductors. Clearly, the depth profile at 100 K exhibits a much narrower peak than that at 300 K. The depth resolution was determined by the full width half maximum (FWHM) of the response function as suggested for inorganic depth profiling.[32] As listed in Table **5-1**, by performing the experiments at 100 K, the depth resolution was significantly improved to 20.7 nm compared to the value of 29.7 nm previously reported at 300 K using 40-keV C_{60}^{+} projectiles at a 40^0 incident angle.[31]

Table **5-1**: Depth resolution and Dowsett's fitting results of depth profiles of single delta layer sample under various experimental conditions.

Sample Temperature	Kinetic Energy	Incident Angle	FWHM (nm)	λ_g (nm)	λ_d (nm)	σ (nm)
300 K	40 keV	40^0	29.7±1.5	4.9±0.1	16.31.1	7.7±0.5
100 K	40 keV	40^0	20.7±0.8	4.9±0.1	8.9±1.2	5.9±0.1
100 K	40 keV	71^0	15.5±.	4.5±0.5	7.6±0.7	3.8±0.3
100 K	20 keV	40^0	16.0±1.0	3.0±0.2	7.7±0.8	4.4±0.2
100 K	20 keV	71^0	12.1±0.9	3.3±0.1	5.6±1.0	3.2±0.1

To quantitatively analyze the profile, Dowsett's empirical function[20,31] was applied to describe the measured signal response as Eq. **5.1**

$$R(z') = N\left[\left(1-erf\left(\xi_1\right)\right)\exp\left(\frac{z'}{\lambda_g}+\frac{\sigma^2}{2\lambda_g{}^2}\right)+\left(1+erf\left(\xi_2\right)\right)\exp\left(\frac{z'}{\lambda_d}-\frac{\sigma^2}{2\lambda_d{}^2}\right)\right] \quad \text{[Eq. 5.1]}$$

with $\xi_1 = \frac{1}{\sqrt{2}}\left(\frac{z'}{\sigma}+\frac{\sigma}{\lambda_g}\right)$ and $\xi_2 = \frac{1}{\sqrt{2}}\left(\frac{z'}{\sigma}-\frac{\sigma}{\lambda_d}\right)$. This function contains three fitting parameters, namely a leading edge growth length (λ_g), a trailing edge decay length (λ_d) and the standard deviation (σ) of a central Gaussian connecting the exponential rise and decay functions. The fitting results obtained from the single delta layer sample are listed in Table **5-1**. It is interesting to notice that, although the half width is smaller at low temperature, the exponentially leading edge exhibits the same slope at 100 K as at 300 K, which is depicted by the same value of λ_g = 4.9 nm at both temperatures. As discussed by Dowsett et al.,[20] the leading edge slope reflects influences of the escape depth of the detected sputtered particles in combination with secondary effects resulting in the release of analyte species through the surface such as segregation. Since these effects should certainly be temperature dependent, our results suggest that λ_g is mainly determined by the information depth of the (static) SIMS spectra, which itself must be largely temperature independent. Considering the monolayer thickness of the LB films used here to be 2.2 to 2.7 nm, the measured information depth is within the range of 1-2 monolayers, similar to what is found in inorganic depth profiling.[33]

The temperature has more significant effects on the trailing edge slope and the central Gaussian width. At 100 K, we obtain λ_d = 8.9 nm and σ = 5.9 nm , both smaller than the respective values of 16.3 nm and 7.7 nm observed at 300 K, making the

300 K profile more asymmetric than the low temperature profile. From the large data base available for inorganic depth profiling, it is known that the asymmetric peak broadening is mainly caused by bombardment induced interlayer mixing.[32] Apparently the largest influence is observed here for the trailing edge, which has been connected with the combined effects of collisional mixing and bombardment enhanced diffusion of analyte species into the underlying matrix.[20,34] Due to the strong temperature dependence, we believe the latter to significantly contribute to the measured decay length for the system studied here. These diffusion-like mixing effects appear to be strongly reduced at low temperature, thereby greatly improving the observed depth resolution.

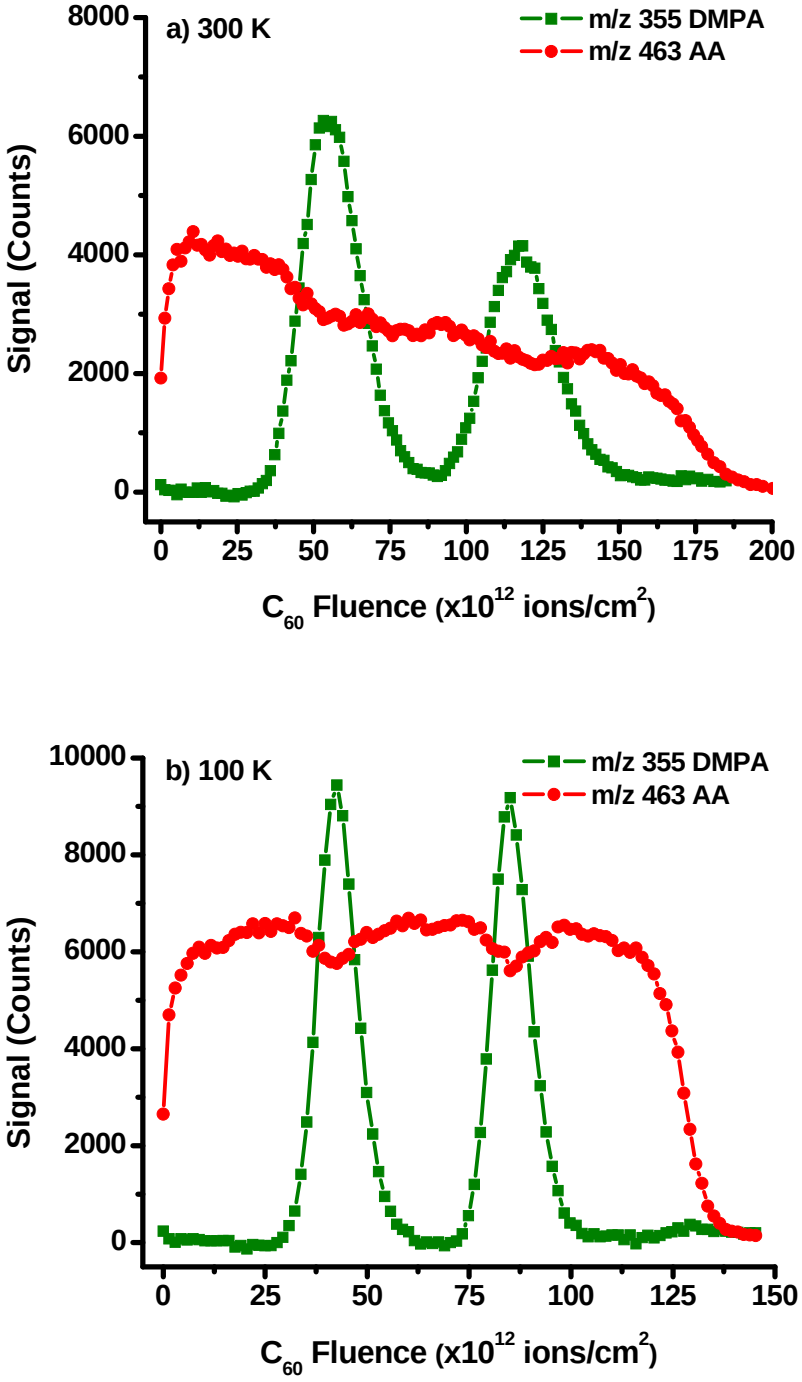

Figure **5-2**: Depth profiles of double delta layer sample at 300 K (a) and 100 K (b) with 40-keV C_{60}^{+} at a 40^{0} incident angle.

A sample with two identical delta layers at different depths was used to evaluate the damage accumulation and depth resolution degradation induced by ion beam erosion. The total thickness of this sample is 314 nm with two 4.4 nm DMPA bilayers located at 103 nm and 209 nm depth, respectively. Depth profiles obtained at 300 K and 100 K with 40-keV C_{60}^+ projectiles at a 40^0 incident angle are shown in Figure **5-2**. In both profiles, there is an initial rise of the AA matrix signal at m/z 463, which has been shown to be associated with the removal of surface contamination.[14] At 300 K, the AA signal never reaches a steady state and exhibits a continuous decay until the film is completely removed. A similar decay is found for the DMPA signals as well. For example, both the peak height and the integrated peak intensity of the signal at m/z 355 dropped by 35% at the second delta layer compared to the first delta layer. In addition to the secondary ion signal decay, the sputter yield is found to decrease with increasing primary ion fluence. With the known thickness of the AA matrix and the C_{60}^+ fluence needed to reach the respective DMPA signal maxima, we are able to calculate the average sputter yield on each AA block. The average sputter yield is 260 molecule equivalents/C_{60} on the top AA block, while 206 molecule equivalents/C_{60} is measured as the average sputter yield on the second one, decreased by ~20%. Both findings indicate accumulation of chemical damage during ion beam sputtering. The depth resolution measured on the two delta layers is 33.4 nm and 36.4 nm, respectively.

In contrast, the depth profile measured at 100 K shows an AA matrix signal which reaches a steady state and stays quite constant through the removal of the film except two dips at the position of the DMPA delta layers. At the same time, the signal from the DMPA layers is well maintained and the same peak heights and integral peak intensities

are observed for both delta layers. In addition, the primary ion fluence used to remove the same amount of AA matrix at a different depth appears to be the same during the erosion of the entire film. Hence, at 100 K, the sputter yield does not decrease with C_{60}^{+} ion fluence. Moreover, the depth resolution measured for the two delta layers is 21.6 nm and 21.3 nm, which agrees with the value obtained on the single delta layer sample under the same experimental conditions. These findings show that low temperature can effectively reduce the damage accumulation and eliminate its influence on the shape of depth profiling. At present, it not clear why this is so. The mechanisms behind ion bombardment induced chemical damage, its accumulation under repeated impact onto the same surface area and its influence on the sputter yield of an organic material are still largely unknown. An energetic C_{60} impact constitutes an immense local disturbance which almost instantaneously pushes the material far out of equilibrium. At this stage, the macroscopic sample temperature is most likely irrelevant. During the time *between* subsequent impacts, however, the material will undergo complex relaxation chemistry, which can spread into previously undamaged volume and lead to further damage there. For the well ordered LB films investigated here, one could, for instance, imagine cross-linking between neighbored molecules to effectively enhance the surface binding energy and reduce the sputter yield. Our data indicate that this chemical "afterglow" of an ion impact can be greatly reduced by lowering the sample temperature.

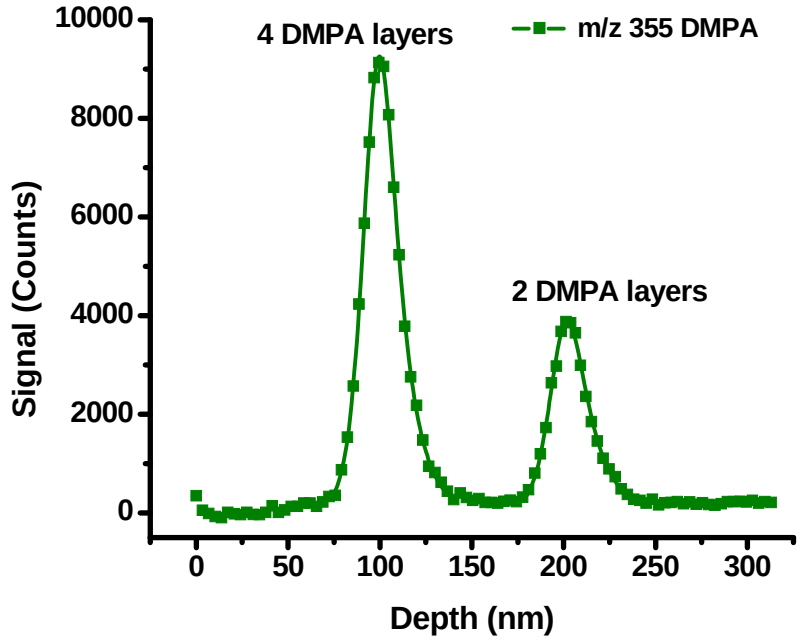

Figure **5-3**: Depth profiles of delta layer sample with 2 different delta layers at 100 K with 40-keV C_{60}^{+} at a 40^{0} incident angle.

Another LB multilayer film was constructed to check whether the observed depth resolution is affected by the thickness of the delta layer. This sample has two DMPA thin layers embedded in three thick AA films. The first DMPA layer is located at a depth of 100 nm and contains two bilayers (8.8 nm), while the second one is composed of one DMPA bilayer (4.4 nm) and is located at a depth of 200 nm below the surface. Using 40-keV C_{60}^{+} projectiles with a 40^{0} incident angle at 100 K, both DMPA layers gave about the same FWHM, 22.2 nm and 23.6 nm (Figure **5-3**), similar to the results acquired on all other delta layers with a single bilayer. It is evident that the FWHM is not affected by the layer thickness and therefore accurately represents the delta depth response function. On the other hand, the layer thickness does change the ion intensity. Since the 8.8 nm layer

contains twice as many molecules, the integrated peak intensities and the peak height are both doubled in the depth profile as expected.

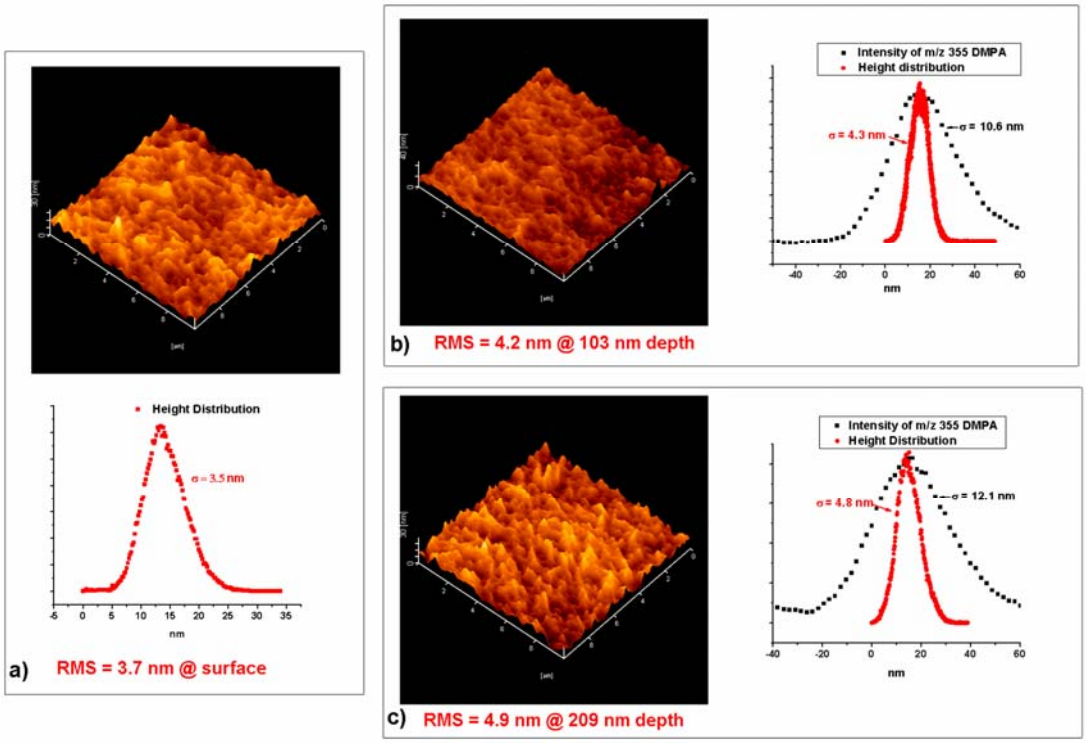

Figure **5-4**: (a) AFM image and height distribution extracted from AFM data of original surface of 314-nm LB film with two delta layers. (b-c) AFM image and SIMS profile of DMPA (m/z 355) as a function of depth compared with AFM height distribution when the film in (a) was eroded to a depth of 103 nm (b) and 209 nm (c).

5.3.2 Surface roughness

There are two theories which describe the depth resolution function of a sputter depth profile, such as Dowsett's function and the so-called MRI model.[20,32,35] In the MRI model, the achievable depth resolution is limited by mixing length (M), surface roughness (R) and information depth (I).[32] Studies on an Irganox delta layer sample have

shown that the depth resolution is purely determined by surface roughness.[19] In order to examine this issue for the system studied here, AFM was used to measure the surface roughness and its change after ion beam erosion to different depths at room temperature. As shown in Figure **5-4** (a), the original surface roughness of a freshly prepared 314 nm LB film is represented by an rms value of 3.7 nm. After etching to the first delta layer at a depth of 103 nm, the surface roughness is measured to be 4.2 nm. At the depth of 209 nm, the rms value obtained from the AFM image is 4.9 nm. Unlike the dramatic surface roughening observed for the Irganox system, the ion beam induced surface topography is obviously quite small for the LB sample and cannot serve as an explanation for the observed degradation of the depth resolution. An overlay of the sample surface height distribution extracted from the AFM data and the DMPA SIMS profile is shown in Figure **5-4** (b-c). It is clear that the measured depth response function is much broader than the height distribution profile, a finding which is in pronounced contrast with the data obtained from the Irganox film, where a complete match of both distributions was found. In particular, the standard deviation (σ) of the central Gaussian determined from the LB delta layer signal is more than two times larger than the standard deviation of the surface height distribution (i.e., the rms roughness value). Therefore, other factors must affect the depth resolution. In Dowsett's function, σ is interpreted as a convolution of delta layer peak broadening due to intrinsic layer thickness, ion beam induced surface roughening and interlayer mixing. As mentioned before, the asymmetric shape of the SIMS profiles indicates that mixing is playing an important role in the peak broadening. In any case, bombardment induced surface microtopography may in part be responsible for the relatively small peak width increase between the first and second delta layer in

Figure **5-2**, but is probably not the dominating factor determining the depth resolution observed for the LB system studied here. Instead, the depth resolution is mainly affected by ion beam induced mixing at the organic-organic interfaces.

5.3.3 Projectile kinetic energy and incident angle

Previous studies on alternating LB films illustrated that better depth resolution (i.e., smaller interface width) can be achieved by lowering the primary ion beam energy.[14] Using the LB delta layer we are able to directly measure the kinetic energy effects on the depth resolution. The depth profiles using 20- and 40-keV C_{60}^+ for both sputter erosion and data acquisition are shown in Figure **5-5** and the depth resolution measured by the FWHM of the DMPA signal response is listed in Table **5-1**. At a 40^0 incident angle, the depth resolution improves from 20.7 nm to 16.0 nm using a 20-keV C_{60}^+ beam. Using a glancing impact angle of the sputtering ion beam is another way to improve the depth resolution.[8] For 40-keV C_{60}^+ at 71^0 impact angle, we obtained a depth resolution of 15.5 nm (see Figure **5-5**). Molecular dynamics (MD) simulation has shown that the energy deposition is related to the incident angle of the projectiles.[36] Increasing incident angle results in a smaller altered layer thickness since the incident energy is deposited closer to the solid surface.[8] Combining lower beam energy and glancing angle, the FHWM on the LB delta layer was pushed to 12.1 nm with a 20-keV C_{60}^+ beam at a 71^0 incident angle and the sample cooled to 100 K.

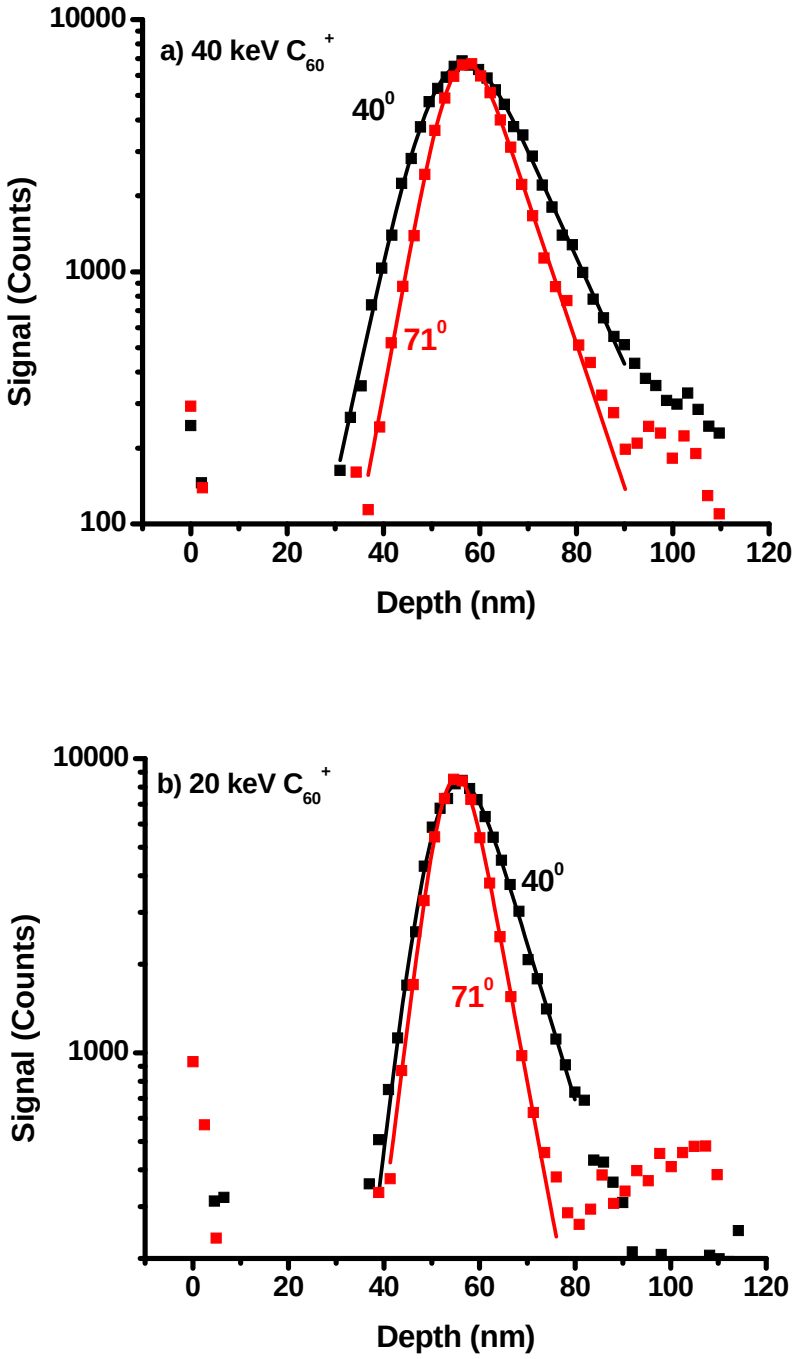

Figure **5-5**: Depth profiles of single delta layer sample at 100 K with 40-keV C_{60}^{+} (a) and 20-keV C_{60}^{+} (b) at 40^0 and 71^0 incident angles.

The listing of Dowsett's fitting parameters obtained under various experimental conditions in Table **5-1** illustrates how the kinetic energy and incident angle change the sputtering process. The kinetic energy has a direct influence on the crater depth produced by a single impact, and therefore the depth from which molecules contribute to a static SIMS spectrum changes as a function of the projectile impact energy. The higher the kinetic energy, the larger the information depth as the leading edge slope λ_g increases from 3 nm at 20 keV to 4-5 nm at 40 keV. No significant difference was observed for λ_g when the incident angle changed from 40^0 to 71^0, indicating that the information depth is largely independent of the impact angle. The trailing edge decay length λ_d as well as the central Gaussian width σ are affected by both the kinetic energy and incident angle. Since ion beam induced topography was low on this sample, smaller values of λ_d and σ indicate less mixing during the ion beam bombardment at lower energy and glancing angle.

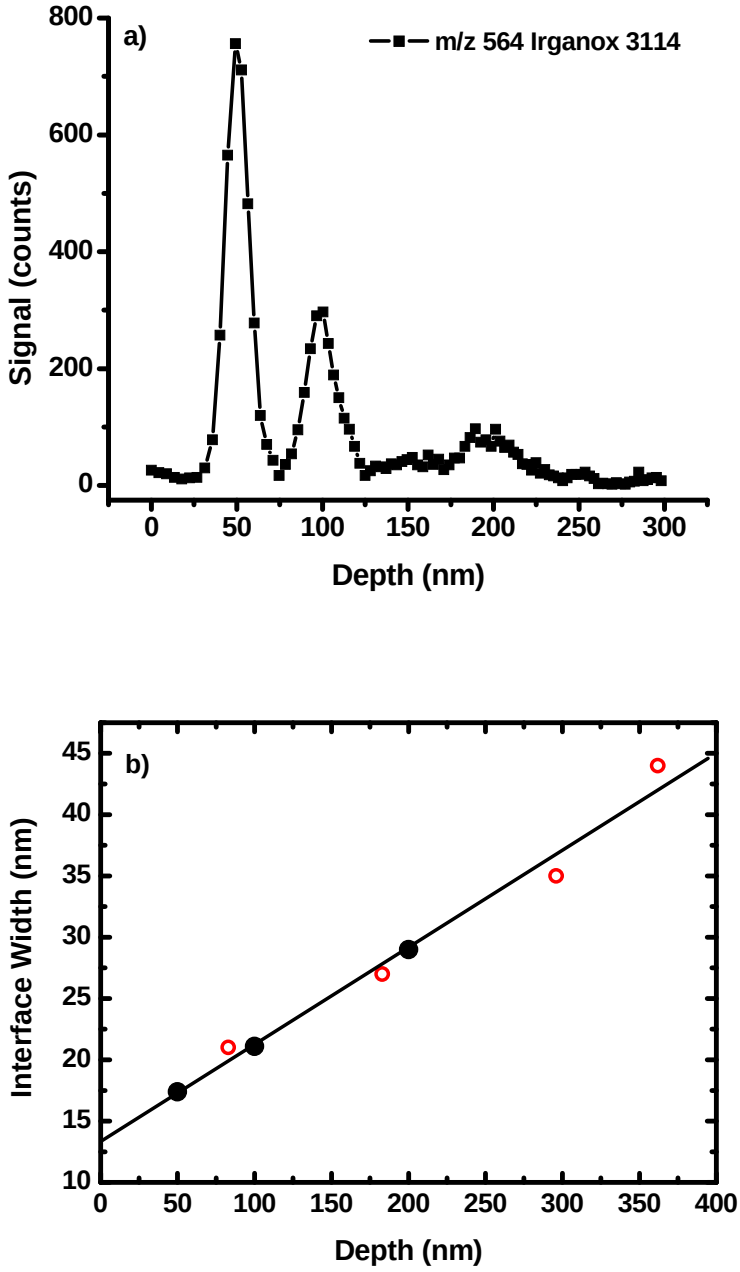

Figure **5-6**: Depth profile of an Irganox 1010/Irganox 3114 delta layer system[37] measured with a 40-keV, 40° C_{60}^{+} ion beam at room temperature (a). The lower panel (b) shows the depth resolution (FWHM) obtained for the first three Irganox 3114 delta layers (solid dots) along with literature values extracted from reference data[19] that was measured using 30-keV C_{60}^{3+} ions.

5.3.4 Material dependency

Two delta layer model systems have been established so far, namely the NPL Irganox delta layer and the LB delta layer presented here. As part of an interlaboratory study conducted under the auspices of VAMAS (Versailles Projects on Advanced Materials and Standards) TWA2, surface chemical analysis,[37] we analyzed the Irganox delta layer sample on the same instrument and under the same experimental conditions as used in this work. Using a 40-keV C_{60}^{+} beam at room temperature with a 40^{0} incident angle, the resulting depth profile is shown in Figure **5-6** (a). The depth resolution (FWHM) extracted for the first three Irganox 3114 delta layers is plotted as a function of depth in Figure **5-6** (b) along with reference data,[19] measured on a similar sample under 30-keV C_{60}^{3+} bombardment. It is seen that the observed depth resolution as well as its dependence on sputtered depth is well reproduced. The FWHM value measured for the first Irganox delta layer (~17 nm) is significantly smaller than that observed for the LB delta layer located at the same depth of 50 nm (29.7 nm). Apparently, the achieved depth resolution is not only dependent upon experimental conditions but also significantly depends on the type of analyzed material. LB multilayers are composed of long, well-organized linear molecules and have an open and ordered structure. MD simulations of sputtering of LB multilayers by C_{60} have shown that the primary energy of projectile fragments can be channeled by the geometrical structure of the AA overlayer due to the unique structure of LB films.[23] The penetration depth of C_{60} projectiles in LB films is 4 to 5 times larger than that in other materials, like molecular benzene[38,39] or polymer samples.[40,41] The experimental results are consistent with the MD simulation data, and it

is not surprising that the vapor deposited Irganox sample always gives better depth resolution than LB films under otherwise identical conditions.

5.4 Conclusions

We show that an organic delta layer system can successfully be constructed by LB techniques and used to investigate the fundamental aspects of molecular depth profiling. For the system studied here, the measured surface roughness is shown to be smaller than the measured interface width. Under these circumstances the results indicate that this width is controlled mainly by interface mixing induced by the bombardment and not by topography. This observation is especially important since it allows evaluation of the relative degree of ion beam mixing as the incident angle of the primary ion and the temperature of the sample are systematically varied.

The LB lipid bilayer is reminiscent of cellular membranes, although the precise structure is quite different since no membrane proteins are involved. Hence, this model study demonstrates that such structures are in principle identifiable in molecular depth profile experiments and therefore should provide a useful guide for future 3-D bioimaging experiments. Clearly, cryogenic conditions using 20-keV C_{60}^{+} bombardment at glancing angles yield the most reliable information.

5.5 Acknowledgement

The authors acknowledge the Lipid MAPS Consortium (GM069338-07) for financial support. Also additional financial support from the National Institutes of Health (2R01 EB002016-17), the National Science Foundation (# CHE-0908226) and the Department of Energy grant no. DE-FG02-06ER15803 is appreciated.

5.6 References

(1) Mahoney, C. M.; Roberson, S. V.; Gillen, G. *Anal. Chem.* **2004**, *76*, 3199.

(2) Cheng, J.; Winograd, N. *Anal. Chem.* **2005**, *77*, 3651.

(3) Sostarecz, A. G.; McQuaw, C. M.; Wucher, A.; Winograd, N. *Anal. Chem.* **2004**, *76*, 6651.

(4) Sostarecz, A. G.; Sun, S.; Szakal, C.; Wucher, A.; Winograd, N. *Appl. Surf. Sci.* **2004**, *231-2*, 179.

(5) Wucher, A.; Sun, S. X.; Szakal, C.; Winograd, N. *Anal. Chem.* **2004**, *76*, 7234.

(6) Wagner, M. S. *Anal. Chem.* **2005**, *77*, 911.

(7) Zheng, L. L.; Wucher, A.; Winograd, N. *J. Am. Soc. Mass Spectrom.* **2008**, *19*, 96.

(8) Kozole, J.; Wucher, A.; Winograd, N. *Anal. Chem.* **2008**, *80*, 5293.

(9) Fletcher, J. S.; Rabbani, S.; Henderson, A.; Blenkinsopp, P.; Thompson, S. P.; Lockyer, N. P.; Vickerman, J. C. *Anal. Chem.* **2008**, *80*, 9058.

(10) Nygren, H.; Hagenhoff, B.; Malmberg, P.; Nilsson, M.; Richter, K. *Microsc Res Techniq* **2007**, *70*, 969.

(11) Jones, E. A.; Lockyer, N. P.; Vickerman, J. C. *Anal. Chem.* **2008**, *80*, 2125.

(12) Mahoney, C. M.; Roberson, S.; Gillen, G. *Appl. Surf. Sci.* **2004**, *231-2*, 174.

(13) Mahoney, C. M.; Fahey, A. J.; Gillen, G. *Anal. Chem.* **2007**, *79*, 828.

(14) Zheng, L. L.; Wucher, A.; Winograd, N. *Anal. Chem.* **2008**, *80*, 7363.

(15) Cheng, J.; Wucher, A.; Winograd, N. *J. Phys. Chem. B* **2006**, *110*, 8329.

(16) Cheng, J.; Kozole, J.; Hengstebeck, R.; Winograd, N. *J. Am. Soc. Mass Spectrom.* **2007**, *18*, 406.

(17) Wucher, A.; Cheng, J.; Winograd, N. *J. Phys. Chem. C* **2008**, *112*, 16550.

(18) Shard, A. G.; Brewer, P. J.; Green, F. M.; Gilmore, I. S. *Surf. Interface Anal.* **2007**, *39*, 294.

(19) Shard, A. G.; Green, F. M.; Brewer, P. J.; Seah, M. P.; Gilmore, I. S. *J. Phys. Chem. B* **2008**, *112*, 2596.

(20) Dowsett, M. G.; Rowlands, G.; Allen, P. N.; Barlow, R. D. *Surf. Interface Anal.* **1994**, *21*, 310.

(21) Fine, J.; Navinsek, B. *Surf. Interface Anal.* **1995**, *23*, 391.

(22) Sjovall, P.; Rading, D.; Ray, S.; Yang, L.; Shard, A. G. *J. Phys. Chem. B* **2010**, *114*, 769.

(23) Paruch, R.; Rzeznik, L.; Czerwinski, B.; Garrison, B. J.; Winograd, N.; Postawa, Z. *J. Phys. Chem. C* **2009**, *113*, 5641.

(24) Sostarecz, A. G.; McQuaw, C. M.; Ewing, A. G.; Winograd, N. *J. Am. Chem. Soc.* **2004**, *126*, 13882.

(25) McQuaw, C. M.; Sostarecz, A. G.; Zheng, L. L.; Ewing, A. G.; Winograd, N. *Langmuir* **2005**, *21*, 807.

(26) McQuaw, C. M.; Sostarecz, A. G.; Zheng, L.; Ewing, A. G.; Winograd, N. *Appl. Surf. Sci.* **2006**, *252*, 6716.

(27) Zheng, L.; McQuaw, C. M.; Ewing, A. G.; Winograd, N. *J. Am. Chem. Soc.* **2007**, *129*, 15730.

(28) Baker, M. J.; Zheng, L.; Winograd, N.; Lockyer, N. P.; Vickerman, J. C. *Langmuir* **2008**, *24*, 11803.

(29) Zheng, L. L.; Wucher, A.; Winograd, N. *Appl. Surf. Sci.* **2008**, *255*, 816.

(30) Zheng, L.; Andreas, W.; Nicholas, W. *Surf. Interface Anal.* **2010** DOI: 10.1002/sia.3509.

(31) Lu, C. Y.; Wucher, A.; Winograd, N. *Surf. Interface Anal.* **2010** DOI: 10.1002/sia.3409.

(32) Hofmann, S. *Surf. Interface Anal.* **2000**, *30*, 228.

(33) Eckstein, W.; Biersack, J. *Nucl Instrum Meth B* **1984**, *2*, 550.

(34) Wittmaack, K. *J. Appl. Phys.* **1982**, *53*, 4817.

(35) Rar, A.; Hofmann, S.; Yoshihara, K.; Kajiwara, K. *Appl. Surf. Sci.* **1999**, *144-45*, 310.

(36) Ryan, K. E.; Smiley, E. J.; Winograd, N.; Garrison, B. J. *Appl. Surf. Sci.* **2008**, *255*, 844.

(37) Shard, A. G.; Foster, R.; Gilmore, I. S.; Lee, J. L. S.; Ray, S.; Yang, L. *Surf. Interface Anal.* **2010** DOI: 10.1002/sia.3268.

(38) Smiley, E. J.; Winograd, N.; Garrison, B. J. *Anal. Chem.* **2007**, *79*, 494.

(39) Ryan, K. E.; Garrison, B. J. *Anal. Chem.* **2008**, *80*, 6666.

(40) Delcorte, A.; Garrison, B. J. *Nucl Instrum Meth B* **2007**, *255*, 223.

(41) Delcorte, A.; Garrison, B. J. *J. Phys. Chem. C* **2007**, *111*, 15312.

Chapter 6

Investigations of Molecular Depth Profiling Using Dual Beams

6.1 Introduction

Secondary ion mass spectrometry (SIMS) is one of the mass spectrometry techniques using a desorption method to ionize solid materials. Upon the bombardment with an energetic ion beam, the analytes are desorbed from the sample surface and produce characteristic molecular and fragment ions. It is a destructive process and the sample is inevitably damaged. This effect is more obvious for organic materials under bombardment by traditional atomic projectiles. Therefore, the ion fluence is usually kept below the static limit to preserve the surface chemistry. When materials are bombarded by a high fluence of atomic primary ions, only elemental information is obtainable. Therefore, organic molecular depth profiling with atomic projectiles is impossible. However, cluster ions behave differently on a solid surface. Unlike atomic ions, which penetrate deep into the sample, a C_{60}^+ ion with high kinetic energy breaks into several carbon atoms upon the bombardment. Each carbon atom carries less energy than a buckyball and creates its own cascading event of moving atoms.[1] This unique physical property leads to energy deposition at the near-surface region and more efficient desorption of molecules, which have been observed by experiments and molecular dynamics (MD) simulation.[2-5] Cluster ions also produce less fragmentation of molecules, enhancing the ability to detect high mass molecular ions and improving the performance

of SIMS on organic materials. Most importantly, the chemical damage caused by cluster ions is much lower than that caused by atomic ions. The chemical damage can be removed by ion beam sputtering, which leaves low damage accumulation. Hence, the materials can be removed in a layer-by-layer fashion. Furthermore, molecular depth profiling is feasible to acquire in-depth chemical information, as has been successfully performed with the C_{60}^+ ion beam on various samples such as spin-coated trehalose films, vapor deposited cholesterol films, Langmuir-Blodgett (LB) multilayer films and Irganox films.[4,6-8]

Sputtering by C_{60}^+ also can be used to recover the molecular ion information from the sample damaged by atomic projectiles bombardment. Previous studies have shown that the molecular ion signal from histamine molecules embedded in an ice matrix exponentially decreases with Ga^+ bombardment, while sputtering with a high fluence of 20-keV C_{60}^+ can quickly restore the molecular ion signal.[9] Similar results have been confirmed on trehalose films doped with peptides.[10] These experimental results suggest that molecular depth profiling may be performed with dual beams, liquid metal ion source (LMIS) for sputtering or milling, and C_{60}^+ for damage removal and signal recovery. In this work, we use a LB multilayer thin film to further investigate the feasibility of the dual beam depth profiling on biological materials. A 402 nm LB thin film consisting of barium arachidate (AA) was sputtered first with an Au^+ beam. Then an depth profile experiment was performed on the same sample with a 40-keV C_{60}^+ beam rastered over a larger area covering the spot pre-bombarded by Au^+. An extremely low erosion rate by the Au^+ beam is found on LB film. The layer thickness altered by Au^+ bombardment is measured from the depth profiles obtained with C_{60}^+ projectiles. The

value is determined as ~90 nm, significantly larger than the value of ~50 nm obtained on a trehalose film pre-bombarded with a Ga^+ source. The results also show that the damage by Au^+ can be removed by C_{60}^+ sputtering and the molecular information can be restored.

6.2 Experimental Section

Arachidic acid, barium chloride (99.999%), copper (II) chloride, potassium hydrogen carbonate (99.7%) and all solvents were purchased from Sigma-aldrich (Allentown, PA.). All chemicals were used without any further purification. Water used in preparation of LB films was obtained from a Nanopure Diamond Life Science Ultrapure Water System (Barnstead International, Dubuque, IA) and had a resistivity of at least 18.2 MΩ·cm.

The preparation of the LB films has been described in detail elsewhere.[7] A single crystal (100) silicon wafer was used as the substrate for all LB films after cleaned with ozone for 10 min and rinsed with high purity water several times to ensure hydrophilicity of the Si/SiO_2 surface. The LB monolayer films of AA were prepared on a Kibron μTrough S-LB (Helsinki, Finland). 149 layers of AA monolayer were sequentially deposited on the Si substrate, resulting in a 402 nm thin film.

Sputter depth profiling was performed in a ToF-SIMS instrument equipped with a fullerene cluster ion source (IOG 40-60, Ionoptika; Southampton, U.K.) and a gold ion source (Ionoptika, Southampton, UK), directed at a 40^0 and 45^0 angle relative to the surface normal, respectively. Details of this instrumentation have been described elsewhere.[11] The sample stage can be cooled to 100 K by liquid nitrogen. All depth

profile experiments in this work were operated at 100 K. Au^+ sputtering was performed by a focused 15-keV Au^+ DC beam at an area of 180 μm × 265 μm. For imaging depth profiling with C_{60}^+, a 40-keV C_{60}^+ ion beam was operated in DC mode to erode through the film at an area of 380 μm × 480 μm covering the Au^+ sputtering area in several seconds intervals. Between erosion cycles, SIMS images with 256 × 256 pixels were acquired from the same area using the pulsed C_{60}^+ beam at an ion fluence of 10^{10} ions/cm^2. ToF mass spectra were retrospectively extracted from any area of interest inside the sputtered region using the image data. In order to monitor the erosion rate of C_{60}^+ projectiles at the Au^+ sputtered area, a wedge crater was created by the C_{60}^+ beam. The details about the wedge method can be found elsewhere.[12]

Film thickness and topography of the sputtered craters were characterized by a KLA-Tencor Nanopics 2100 atomic force microscope (AFM).

6.3 Results and Discussion

6.3.1 Erosion by a Au^+ beam

The erosion rate and sputter yield of Au^+ projectiles on the LB multilayer thin film are examined by etching the 402-nm AA film using a focused beam of 15-keV Au^+ with various fluences. The DC beam was rastered over four different areas of 180 μm × 265 μm with an Au^+ fluence of 3×10^{14} ions/cm^2, 6×10^{14} ions/cm^2, 1.2×10^{15} ions/cm^2, and 2.4×10^{15} ions/cm^2 respectively, resulting in four individual craters. Then the dimensions of the resulting craters were measured by AFM. Surprisingly, similar

shallow craters are observed from the AFM images of the different eroded areas. They all have about the same depth of ~10 nm, despite the ion fluence for sputtering ranges from 3×10^{14} ions/cm^2 to 2.4×10^{15} ions/cm^2.

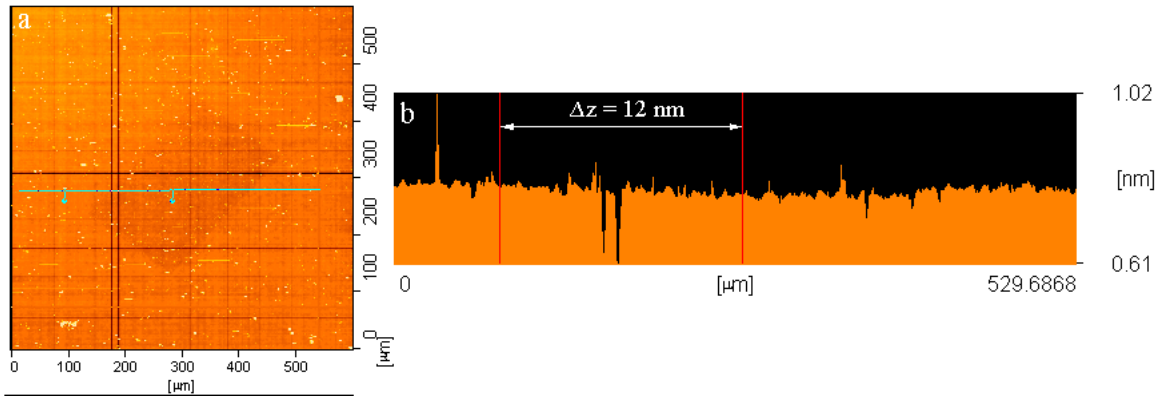

Figure **6-1**: AFM images of the AA film bombarded by 15-keV Au^+ with a fluence of 2.4×10^{15} ions/cm^2. The AFM image in (a) is a top view of the bombarded region of the film taken from a 600 µm × 600 µm field. The AFM image in (b) is a line-scan taken across the bombarded region of the film. The measured crater depth is ~12 nm.

The AFM topographical image of the crater created by Au^+ projectiles with a fluence of 2.4×10^{15} ions/cm^2 is shown in Figure **6-1** (a). The line scan in Figure **6-1** (b) demonstrates that the film is etched by no more than 12 nm (about the thickness of 4 monolayers). Based on the results obtained from these four craters, the sputter yield of Au^+ on AA multilayer film is estimated at the order of 10^{-8} molecules/ion, which is extremely low and indicates that the AA film can be barely sputtered by Au^+. Similar studies on spin-coated trehalose films have shown that each Au^+ impact is able to sputter away 1.5 trehalose molecular equivalents with a 25-keV Au^+ beam.[13] Using a 15-keV Ga^+ beam, there are six trehalose molecular equivalents removed per Ga^+ ion impact.[10] These values are much higher than the sputter yield of Au^+ projectiles on AA film.

Apparently, the sputter yield of atomic projectiles varies greatly for different materials. In focused ion beam (FIB) experiments, an atomic beam (usually Ga^+) is used for site specific sputtering or milling. It is generally believed that any material can be eroded by FIB. However, the system we used in this work seems to be an exception. The exact reason of the extremely low sputter yield of Au^+ projectiles on LB film is not fully understood so far. We speculate that it may be related to the unique structure of LB multilayer. MD simulation studies have revealed that C_{60}^+ projectiles can penetrate more than two times deeper into an AA overlayer than into a firmly-packed benzene film.[14] This could also be the same situation for Au^+. The open and well-oriented structure of the LB film may allow energetic Au^+ ions to travel deeper into the LB film. Most of the energies carried by the projectiles could be deposited at a deeper depth, resulting in low sputter efficiency. One might expect to observe more chemical damage underneath the sample surface. This hypothesis was examined by the following depth profile experiments with a C_{60}^+ beam.

6.3.2 Depth profiling with C_{60}^+ beam

Imaging depth profile experiments with C_{60}^+ were performed over the four regions pre-bombarded by Au^+. The first total ion SIMS image of the C_{60}^+ depth profile analysis is shown in Figure **6-2** (c). The area pre-bombarded by 3×10^{14} Au^+/cm^2 can be easily recognized by the rectangular shadow in the center. Outside the central shadow is undamaged AA film. By selecting pixels at region **a** (as shown in Figure **6-2**(c)) from the image data, we are able to extract mass spectral information and construct the depth

profile of the undamaged AA film (see Figure **6-2** (a)). The depth profile of the Au^+ pre-bombarded film is obtained in a similar way by extracting the mass spectral information from region **b** (see Figure **6-2** (b)). Signals at m/z 463 and m/z 309 represent the molecular ion and the fragment ion of AA, respectively. For a better comparison, the signals shown in these figures are normalized by pixel numbers.

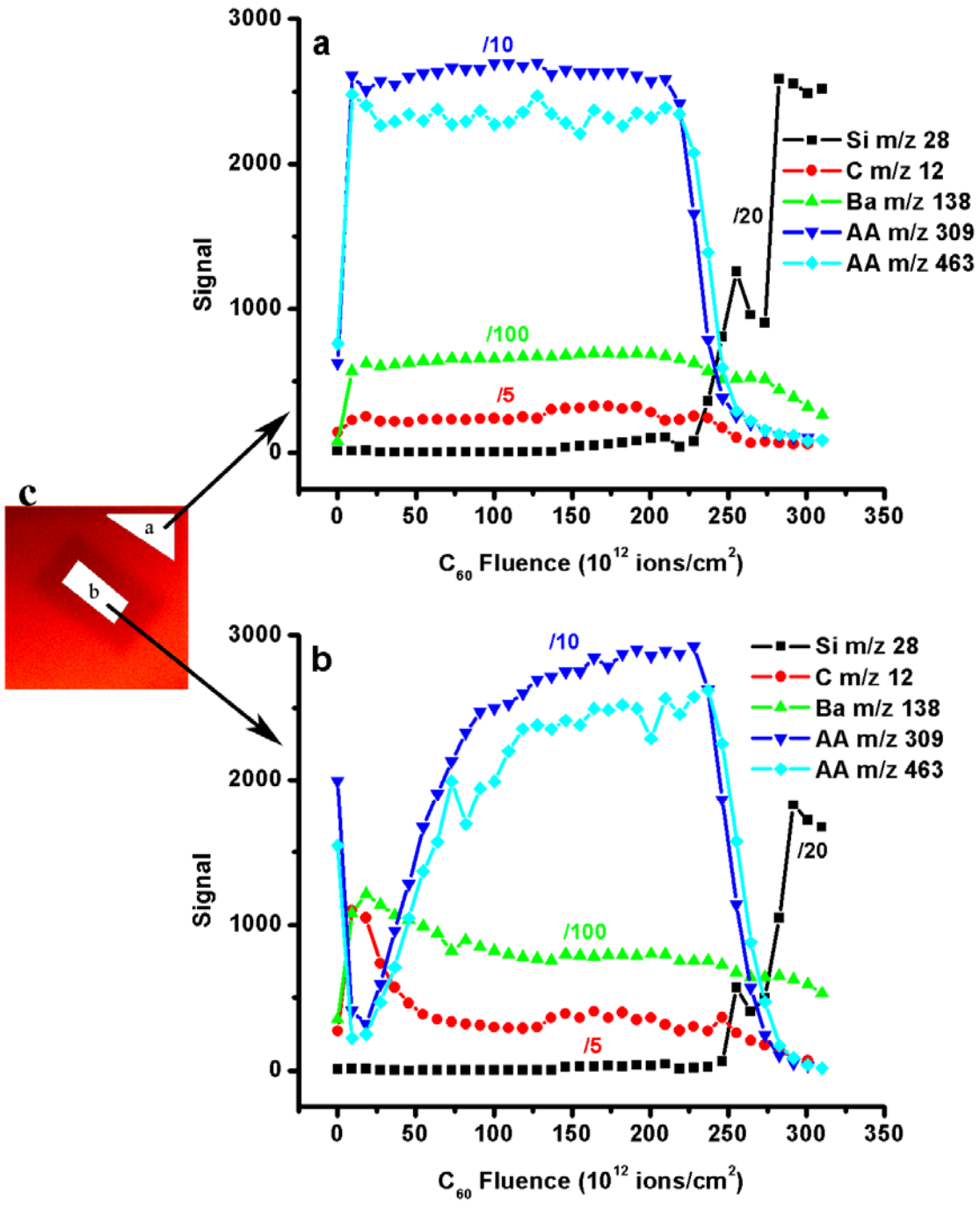

Figure **6-2**: Depth profiles of (a) undamaged AA film and (b) AA film pre-bombarded by 3×10^{14} Au^{+}/cm^{2}, extracted from corresponding regions shown in (c) total ion mass spectral image.

As expected, the results obtained from region **a** exhibits the typical shape of the depth profile of intact AA film, which has been observed before.[15] After the initial rise due to removal of impurities at the surface, the signals of m/z 463 and m/z 309 reach their steady state and remain constant during the erosion of the entire film, and then start to drop while approaching the interface to Si substrate. The position of the interface to the underlying substrate can be identified by the point where the AA signal drops to 50% of its maximum. Hence, the erosion rate and sputter yield of the intact AA film can be calculated from the depth profile at region **a** with the known film thickness, the erosion time, and the ion fluence required to remove the entire film. Mass spectral information subtracted from region **b** illustrates the depth profile of the Au^+ pre-bombarded film. It starts with fairly low signal intensities of m/z 463 and m/z 309 in the beginning, except the first data point due to the ionization effect on the sample surface. On the other hand, higher intensities of small fragment ions in low mass region such as C^+ at m/z 12 and Ba^+ at m/z 138 are detected at the same C_{60}^+ fluence. This indicates the first few monolayers of AA are damaged by Au^+ bombardment, resulting in extensive fragmentation of AA molecules. As more C_{60}^+ fluence applied, the intensities of C^+ and Ba^+ decrease while the signals of m/z 463 and m/z 309 keep increasing until they reached the same level as in the undamaged AA film. Then they stay constant, which suggests the C_{60}^+ beam is able to sputter away the damage layer and recover the molecular ion information from the underlying intact AA layers.

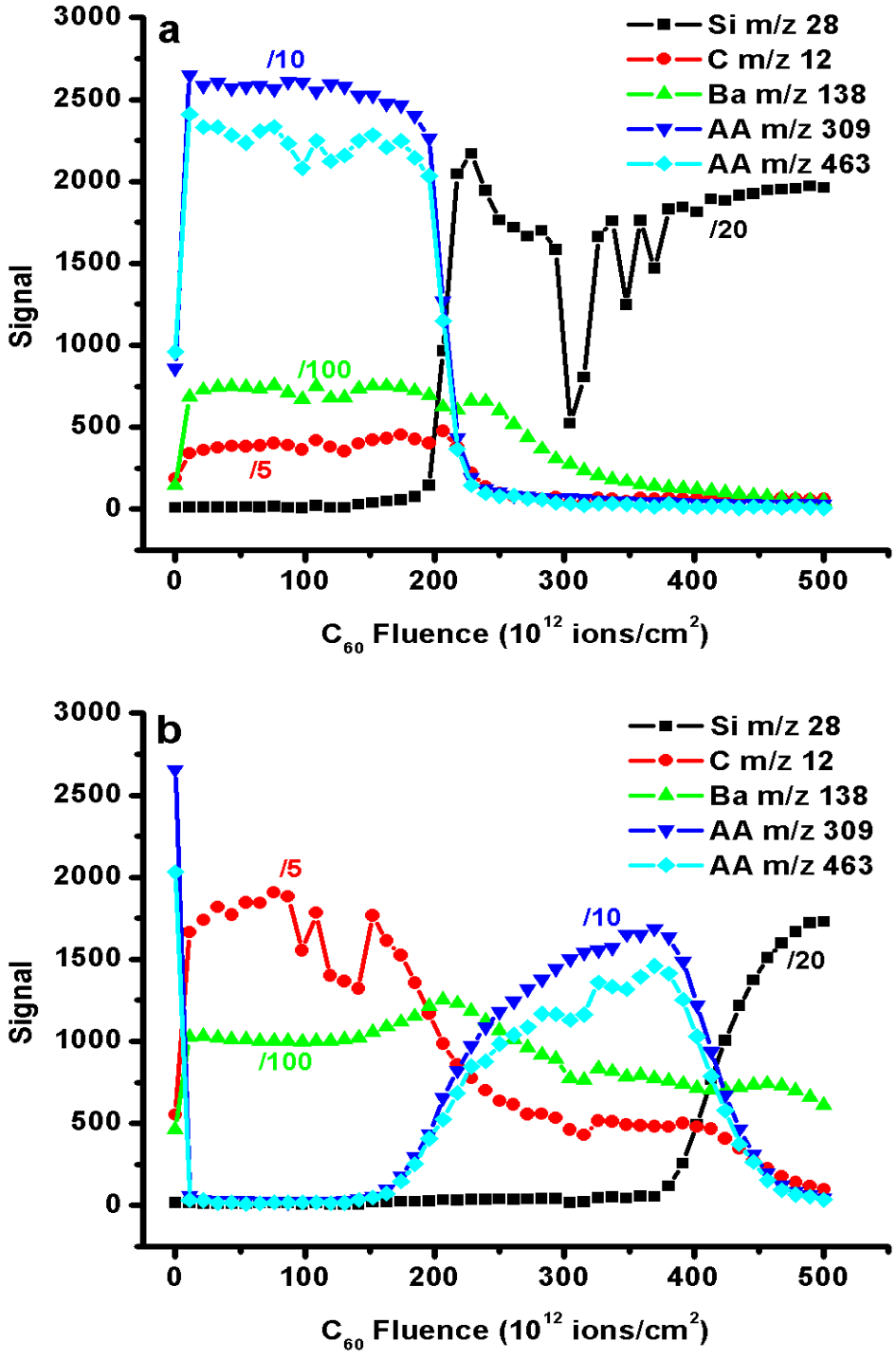

Figure **6-3**: Depth profiles of (a) undamaged AA film and (b) AA film pre-bombarded by 6×10^{14} Au^{+} ions/cm^2.

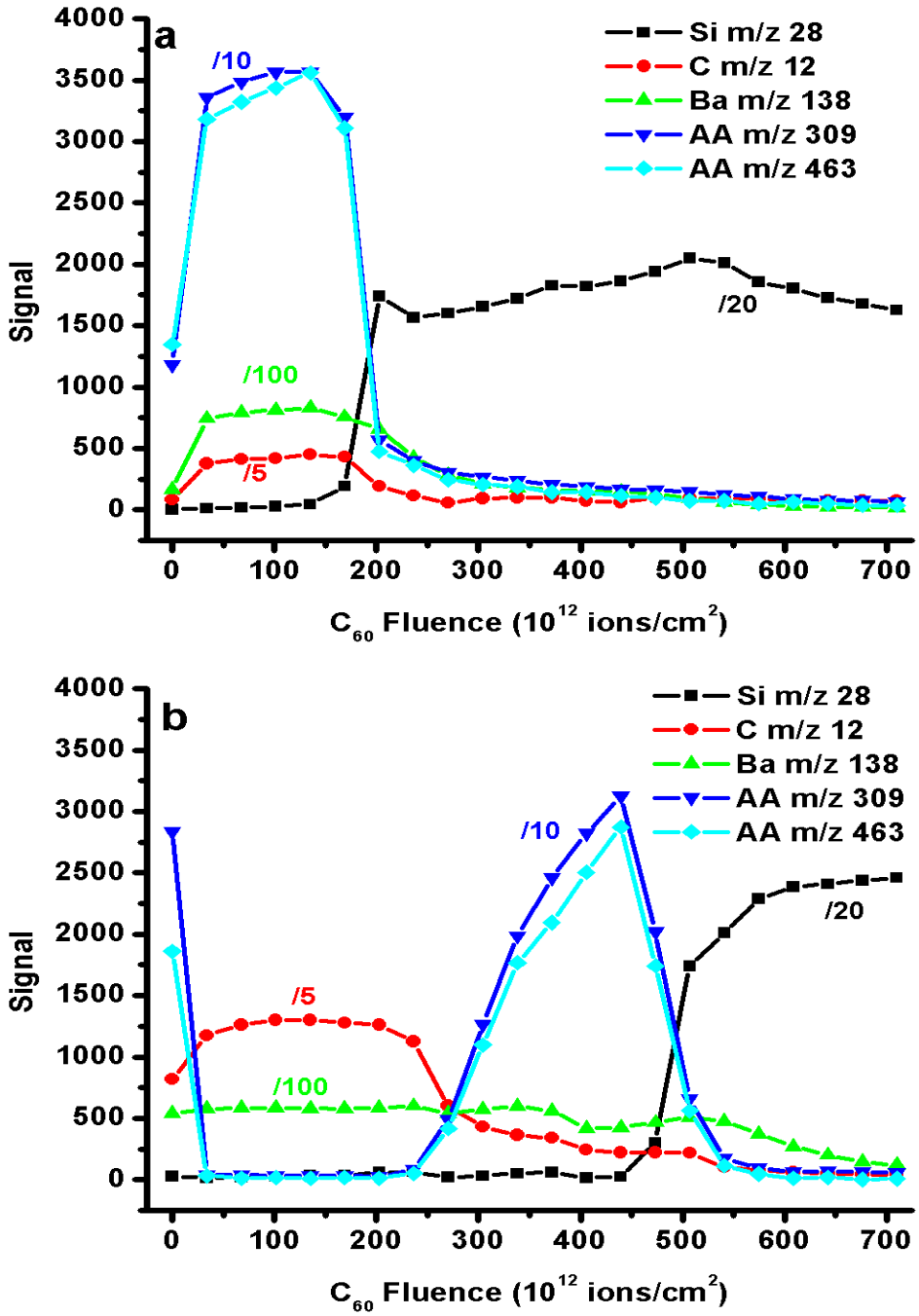

Figure **6-4**: Depth profiles of (a) undamaged AA film and (b) AA film pre-bombarded by 1.2×10^{15} Au^{+} ions/cm^2.

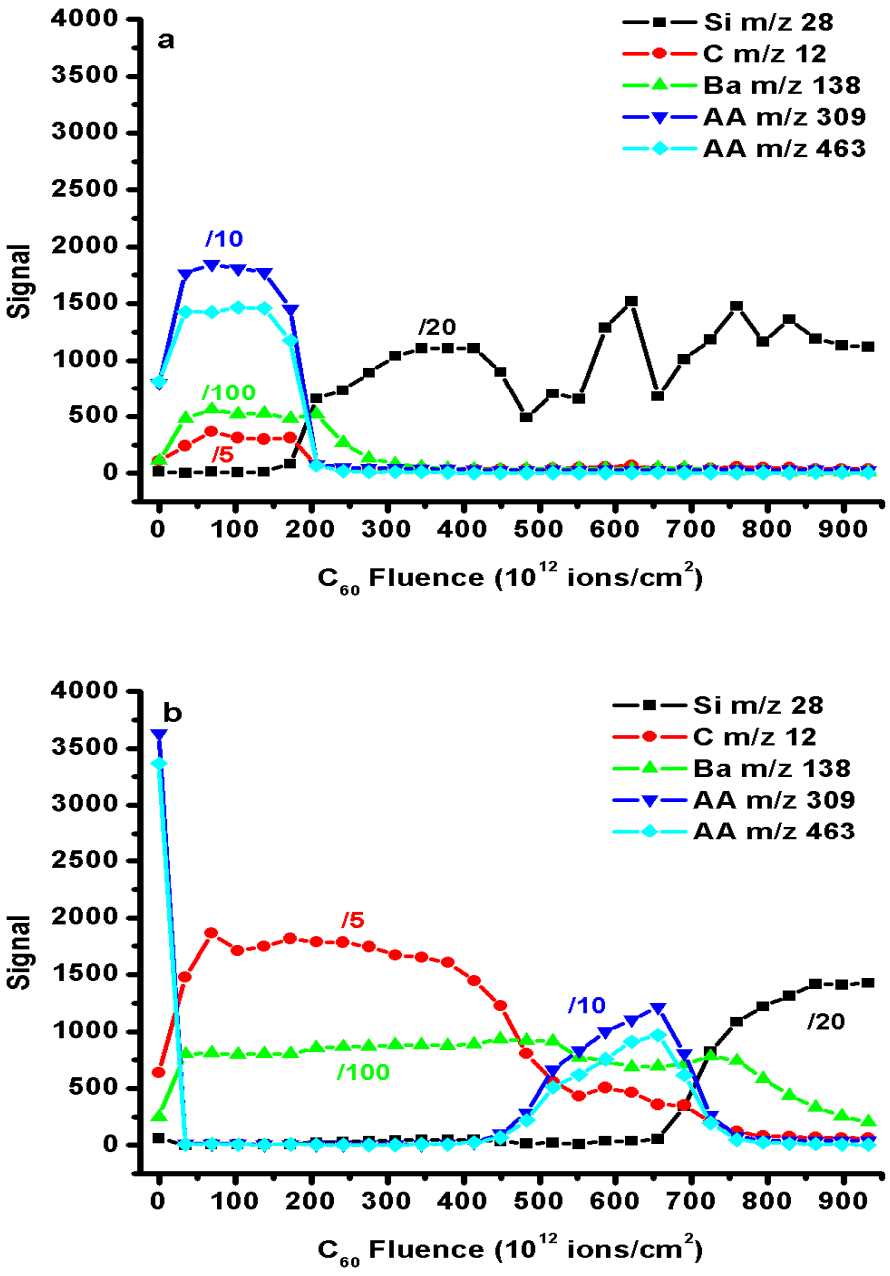

Figure **6-5**: Depth profiles of (a) undamaged AA film and (b) AA film pre-bombarded by 2.4×10^{15} Au^{+} ions/cm^2.

The depth profiles obtained over another three areas pre-bombarded with different fluences of Au^+ reveal more damage in the AA film. The secondary ion signals have been plotted versus C_{60}^+ fluence at the area pre-bombarded with 6×10^{14} Au^+/cm^2, 1.2×10^{15} Au^+/cm^2, and $2.4 \times 10^{15} Au^+/cm^2$, as shown in Figure **6-3**, Figure **6-4**, and Figure **6-5,** respectively. The C_{60}^+ fluence required to remove the damage layer increases with the Au^+ fluence used for the pre-bombardment. In order to convert the C_{60}^+ fluence to a depth scale, a protocol was introduced: a linear interpolation of the erosion rate between the completely damaged AA film and the undamaged AA film. The momentary erosion rate $\dot{z}$ of the interface between the completely damaged AA film and the undamaged AA film is calculated as Eq. **6.1**

$$\dot{z} = \dot{z}_{Au}\left(1 - \frac{I_{AA}}{I_{AA}^{\max}}\right) + \dot{z}_{AA}\frac{I_{AA}}{I_{AA}^{\max}} \qquad \text{[Eq. 6.1]}$$

where $I_{AA}^{\max}$ denotes the AA molecular ion signal of the undamaged AA film at the steady state measured from region **a**. Assuming the erosion rate of the completely damaged AA film $\dot{z}_{Au}$ is a fraction of the erosion rate of the undamaged AA film $\dot{z}_{AA}$, we obtain an expression $\dot{z}_{Au} = \alpha \cdot \dot{z}_{AA}$, and Eq. **6.2**

$$\sum \dot{z}\Delta t = \sum\left[\alpha\left(1 - \frac{I_{AA}}{I_{AA}^{\max}}\right) + \frac{I_{AA}}{I_{AA}^{\max}}\right]\dot{z}_{AA}\Delta t \qquad \text{[Eq. 6.2]}$$

$\sum \dot{z}\Delta t$ is the film thickness and $\dot{z}_{AA}$ can be calculated from the depth profile at region **a**. Therefore, α can be determined using Eq. **6.2**, and then $\dot{z}_{Au}$ is able to be obtained to calculate the erosion depth.

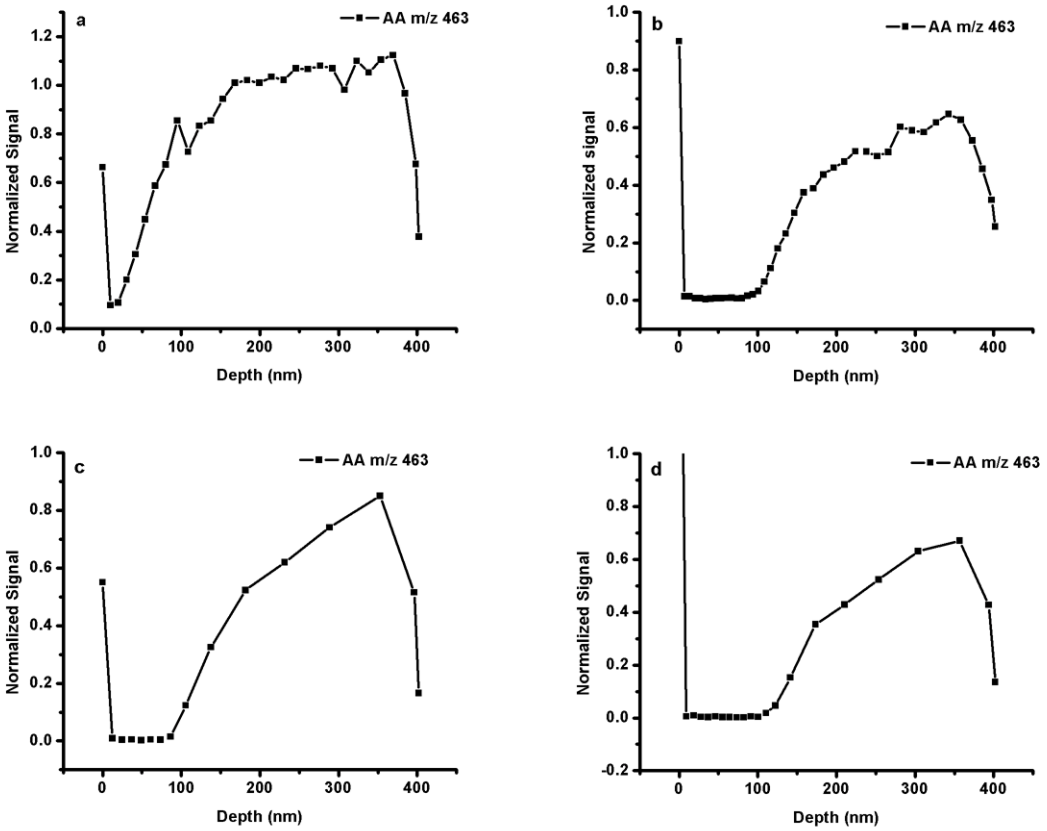

Figure **6-6**: Depth profiles of AA film pre-bombarded by (a) 3×10^{14} Au^+/cm^2, (b) 6×10^{14} Au^+/cm^2, (c) 1.2×10^{15} Au^+/cm^2, and (d) 2.4×10^{15} Au^+/cm^2.

The resulting depth profiles are plotted in a depth scale in Figure **6-6**. They reveal unique information about the thickness of the surface layer influenced by Au^+ bombardment. In Figure **6-6** (a), an Au^+ fluence of 3×10^{14} ions/cm^2 was applied for Au^+ bombardment and the film appears to be partially damaged. A distinct damaged layer is observed after bombardment with a higher Au^+ fluence, as shown in Figure **6-6** (b-d), from which we can directly measure the altered layer thickness caused by Au^+ bombardment. An altered layer thickness of ~90 nm is determined from the depth profiles in Figure **6-6** (b-d). A value of ~50 nm is the first reported altered layer

thickness in an organic overlayer caused by metal ion bombardment. This was measured on a trehalose film bombarded by 15-keV Ga^+.[10] The ~90 nm altered layer thickness for 15-keV Au^+ on LB overlayer is quite large. Since these two different values were acquired with the same kinetic energy of the projectiles, one might speculate that the large altered layer thickness could be related to the different types of materials and/or the different projectiles. It is quite possible that the well-oriented structure of LB film is responsible for the largely altered layer thickness value. Its open structure allows the projectiles to penetrate further into the sample, thus causing more damage at a deeper depth. Unfortunately, no secondary ion signal can be detected from the Au^+ ions embedded in the AA film. We are not able to examine the implantation of Au^+ because of its high ionization energy and the interference from an AA fragment ion at m/z 197. If that is the case, it will also explain the low sputter yield of Au^+ projectiles on LB films. To examine the influence of different atomic projectiles on the LB overlayer, more experiments using Ga^+ projectiles need to be done in the future.

6.3.3 Investigation of erosion rate by wedge method

It has been noticed that the C_{60}^+ fluence required to remove the damaged layer is related to the Au^+ fluence used for the pre-bombardment. A wedge-shaped erosion pattern was employed here to monitor the erosion rate on the altered layer caused by Au^+.

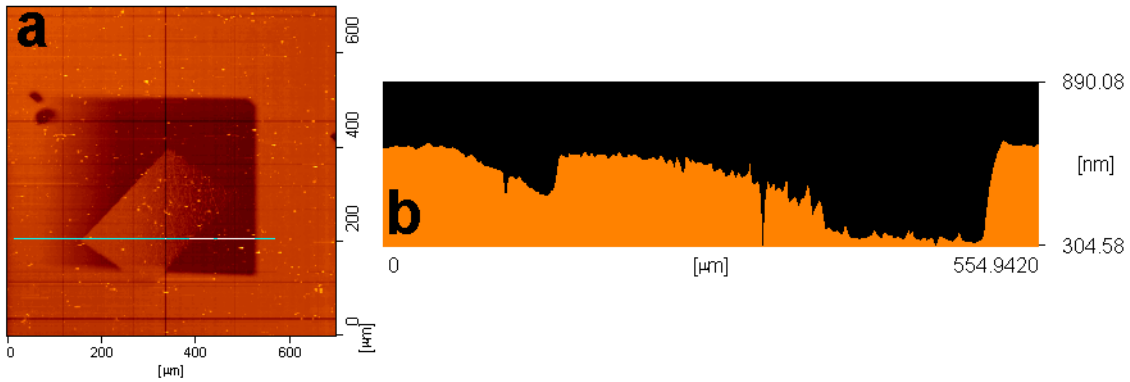

Figure **6-7**: (a) AFM topography image of the wedge crater surface. The horizontal white line in (a) denotes the position of the line scan profile shown in (b).

As shown in Figure **6-7** (a), a crater of 480 µm × 380 µm was created by a focused C_{60}^+ beam over the region pre-bombarded by 2.4×10^{15} Au^+/cm^2. The crater area was evenly divided into 256 scanning frames along the x axis and each frame received a linearly-increased C_{60}^+ fluence. More specifically, zero fluence of C_{60}^+ was applied on the first frame at the left edge and 4.4×10^{14} C_{60}^+/cm^2 was put on the 256th frame at the right edge. Therefore, the *n* frame in-between received $(4.4 \times 10^{14})/(n\text{-}1)$ C_{60}^+/cm^2. The topological information of the resulting wedge crater can be acquired by AFM to provide the fundamental parameters of molecular depth profiling such as erosion rate and surface roughness at different depths.[12] The AFM topography image in Figure **6-7** (a) shows the wedge crater surface. A rectangular-shaped island is found at the area pre-bombarded by Au^+. Its brighter color represents a higher sample height in the Au^+ pre-bombarded film than in the undamaged AA film within the same scanning frame, which also indicates that less materials are sputtered away from the altered layer than from the undamaged AA film under the same C_{60}^+ fluence.

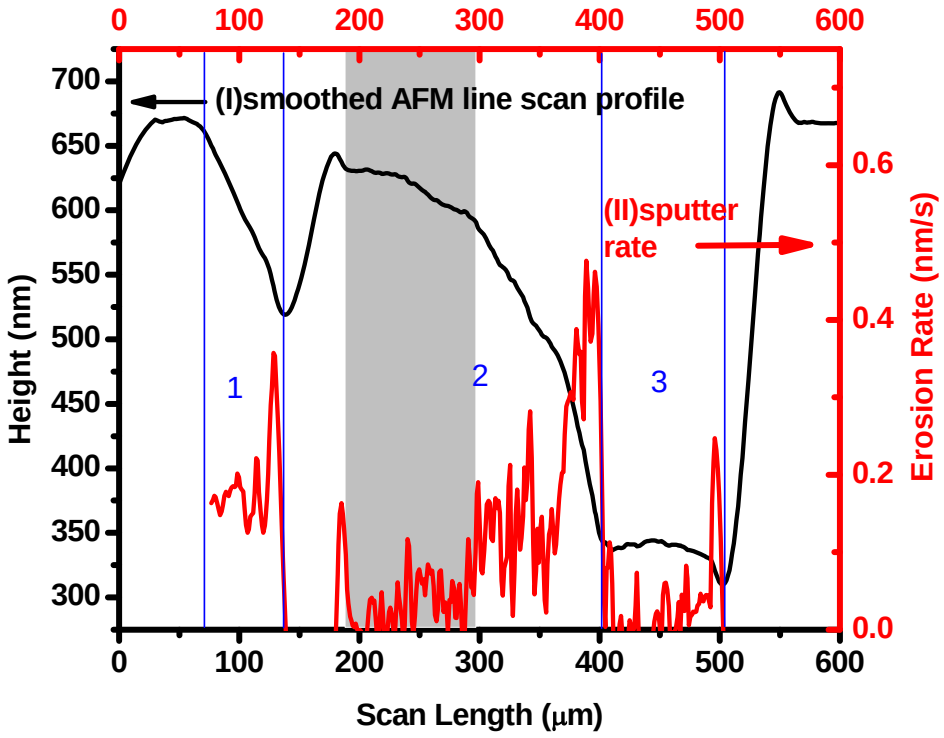

Figure **6-8**: Smoothed AFM line scan profile of Figure **6-7**(b) is plotted as black curve (I). The erosion rate is shown in red curve (II). The grey shadow denotes the area eroded within ~90 nm by C_{60}^{+}. Intact AA film is at region 1 and 3, and Au+ pre-bombarded film is at region 2.

Figure **6-7** (b) is a line scan of the AFM image and characterizes the eroded depth of the wedge crater at each pixel along the x axis. After the smoothing process, we obtained a smoothed line-scan profile, shown as plot (I) in Figure **6-8**. The instant erosion rate at each pixel can be calculated from the smoothed line-scan profile. The erosion rate profile (plot (II) in Figure **6-8**) consists of three distinct regions. Region **1** is corresponding to the intact AA film, where a constant erosion rate is observed. At region **3**, the LB film has been almost removed and the erosion rate on Si substrate is extremely low. The most interesting part is region **2**. It covers the Au^{+} pre-bombarded area and

exhibits a variation of the sputter rate. At the near surface region (as shown in the shadow in Figure **6-8**), the erosion rate is extremely low (almost zero), then it gradually goes up when the eroded depth is over ~100 nm. It is important to point out that the region with the lowest erosion rate is almost the same as the location of the Au^+ altered layer. Why the altered layer has a low erosion rate is not clear so far. A possible reason is that the sample damage and/or Au^+ implantation change the film composition and C_{60}^+ projectiles have low sputter efficiency on Au^+ implanted film.

6.4 Conclusions

In summary, we have examined the possibility of depth profiling on LB thin films using Au^+ and C_{60}^+ sources. Although the Ga^+ beam has been widely used in FIB experiments to erode various materials, Au^+, as another type of atomic beam, behaves quite differently on a LB thin film. Bombardment by Au^+ projectiles shows extremely low sputter efficiency and results in significant chemical damage on the AA LB film. Sputtering with a C_{60}^+ beam is an effective way to remove the damage caused by Au^+ and to recover the molecular ion information. The altered layer thickness of Au^+ bombardment appears to be ~90 nm based on the measurement on the C_{60}^+ depth profiles, much larger than the value obtained from another organic film. That indicates that the altered layer thickness might be dependent on the material type. As we know so far, some materials are more difficultly sputtered by a C_{60}^+ beam, such as polymers of polystyrene type. Atomic projectiles may erode the materials which C_{60}^+ can not, but it always causes severe chemical damage. The dual beam sputtering strategy is a possible

solution to acquire in-depth chemical information from materials which can not be sputtered by C_{60}^+, with an atomic ion beam for erosion and a C_{60}^+ beam for damage removal and molecular information acquisition. The LB film is not suitable for erosion by metal ion projectiles and the capability of this method needs to be further investigated on other types of organic materials in the future.

6.5 Acknowledgement

Financial support from the National Institute of Health under grant no. 2R01 EB002016-17, the National Science Foundation under grant no. CHE-0908226 and the Department of Energy grant no. DE-FG02-06ER15803 are acknowledged.

6.6 References

(1) Winograd, N. *Anal. Chem.* **2005**, *77*, 142a.

(2) Postawa, Z.; Ludwig, K.; Piaskowy, J.; Krantzman, K.; Winograd, N.; Garrison, B. J. *Nucl Instrum Meth B* **2003**, *202*, 168.

(3) Postawa, Z.; Czerwinski, B.; Szewczyk, M.; Smiley, E. J.; Winograd, N.; Garrison, B. J. *Anal. Chem.* **2003**, *75*, 4402.

(4) Cheng, J.; Winograd, N. *Anal. Chem.* **2005**, *77*, 3651.

(5) Ryan, K. E.; Garrison, B. J. *Anal. Chem.* **2008**, *80*, 6666.

(6) Kozole, J.; Wucher, A.; Winograd, N. *Anal. Chem.* **2008**, *80*, 5293.

(7) Zheng, L. L.; Wucher, A.; Winograd, N. *J. Am. Soc. Mass Spectrom.* **2008**, *19*, 96.

(8) Shard, A. G.; Green, F. M.; Brewer, P. J.; Seah, M. P.; Gilmore, I. S. *J. Phys. Chem. B* **2008**, *112*, 2596.

(9) Wucher, A.; Sun, S. X.; Szakal, C.; Winograd, N. *Anal. Chem.* **2004**, *76*, 7234.

(10) Wucher, A.; Cheng, J.; Winograd, N. *Anal. Chem.* **2007**, *79*, 5529.

(11) Braun, R. M.; Blenkinsopp, P.; Mullock, S. J.; Corlett, C.; Willey, K. F.; Vickerman, J. C.; Winograd, N. *Rapid Commun. Mass Spectrom.* **1998**, *12*, 1246.

(12) Mao, D.; Wucher, A.; Winograd, N. *Anal. Chem.* **2010**, *82*, 57.

(13) Cheng, J.; Wucher, A.; Winograd, N. *J. Phys. Chem. B* **2006**, *110*, 8329.

(14) Paruch, R.; Rzeznik, L.; Czerwinski, B.; Garrison, B. J.; Winograd, N.; Postawa, Z. *J. Phys. Chem. C* **2009**, *113*, 5641.

(15) Zheng, L. L.; Wucher, A.; Winograd, N. *Anal. Chem.* **2008**, *80*, 7363.

Chapter 7

Finale

7.1 Conclusions and Future Directions

The advent of commercially available cluster ion beams has expanded the applications of time-of-flight secondary ion mass spectrometry (ToF-SIMS) in the characterization of organic and biological materials. This thesis is focused on understanding the fundamentals of molecular depth profiling using ToF-SIMS and a C_{60}^+ ion source. The ultimate goal is to maximize the performance of C_{60}-SIMS in 3-dimensional (3-D) imaging for complex materials.

Although many successful examples have demonstrated the feasibility of molecular depth profiling with C_{60}^+ projectiles on diverse materials, understanding of ionization effects associated with complicated biological samples is necessary. The investigation of peptide doped trehalose films illustrates that water content aid in the formation of protonated molecular species. Salts, commonly present in biological samples, affect the ionization of organic molecules differently based on their basicity.

Molecular depth profiling is an emerging research area in the SIMS community. Results obtained from the Irganox delta layer system are reliable and repeatable. Another delta layer system is constructed by LB techniques using lipids and fatty acids. In this thesis work, this system is used to investigate the depth resolution in biological materials. Since the ion beam induced mixing at organic-organic interfaces mainly controls the

achievable depth resolution, 3-D imaging of biological samples are suggested to be carried at cryogenic temperature with low energy C_{60}^+ projectiles at a glancing incident angle.

The success of molecular depth profiling on buried lipid bilayers encourages the further exploration of 3-D mass spectral imaging on biological samples. In the future, a more complex model of a liposome can be adopted to demonstrate the strength of 3-D imaging with C_{60}-SIMS. Liposomes are small artificial vesicles of spherical shape that can be produced from phospholipids and cholesterol.[1] The liposome model has the essential structure and skeleton of a single cell. Since they are made of lipid bilayers similar to cell membranes, liposomes have been used as models for the study of cells.[2-4] Moreover, small molecules such as peptides can be encapsulated inside to form a 3-D structure. Giant liposomes formed by a double-emulsion technique[5] can also serve as a good model to verify the applicability of 3-D mass spectral imaging on single cells. To preserve the integrity of liposomes in vacuum, the sample will be processed in a frozen-hydrated state. This is also favorable since cryogenic temperatures are optimal experimental conditions for C_{60}^+ depth profiling. The wedge method is also preferred to illustrate the 3-D structure of liposome with respect to the time efficiency.[6]

The possibility of dual-beam sputtering is investigated in Chapter 6. The sputter yield of Au^+ projectiles appears to be extremely low on LB film. To understand this phenomenon, the same system needs to be tested with another atomic ion source, such as Ga^+. The altered layer thickness of LB multilayer film by Au^+ bombardment is approximately 90 nm, indicating a deeper penetration depth of atomic projectiles compared to other organic films. Although the expected erosion by Au^+ is not achieved,

C_{60}^+ projectiles have been shown to be able to restore the molecular information from the LB film damaged by Au^+. The dual-beam strategy is particularly useful for the 3-D characterization of organic materials which can not be sputtered by C_{60}^+, i.e. polystyrene. It will be worthwhile to investigate this matter in the future.

Research efforts have been continuously devoted to the renovation and development of SIMS instruments. Recently novel SIMS instruments, a hybrid-quadrupole orthogonal ToF mass spectrometer equipped with a C_{60} ion source[7-10] and the J105 3-D Chemical Imager[11-13] have been built based on a new method of ToF analysis. In both instruments, the mass spectrometer is decoupled from the sputtering process, which enable a DC primary cluster ion beam to be used. The DC beam provides rapid data acquisition with simultaneous high mass resolution and high spatial resolution. The J105 has a shaped-field buncher combined with a nonlinear reflectron which allows for the inclusion of a collision cell and an intermediate ToF selection gate. With this setup, the mass spectral analysis can be operated in both ms-ms mode and traditional ToF-MS mode. The automatic sample entry system of J105 is equipped with a novel freeze-fracture device and specifically suited for the biological or organic samples in aqueous suspension. In the future, the application of these new instruments will enhance the performance of 2-D and 3-D mass spectral imaging analysis of single cells.

7.2 References

(1) Bangham, A. D.; Standish, M. M.; Watkins, J. C. *J. Mol. Biol.* **1965**, *13*, 238.

(2) Cans, A. S.; Wittenberg, N.; Karlsson, R.; Sombers, L.; Karlsson, M.; Orwar, O.; Ewing, A. *Proc. Natl. Acad. Sci. U. S. A.* **2003**, *100*, 400.

(3) Edidin, M. *Annu. Rev. Biophys. Biomol. Struct.* **2003**, *32*, 257.

(4) Oberholzer, T.; Luisi, P. L. *J Biol Phys* **2002**, *28*, 733.

(5) Zhan, W.; Bard, A. J. *Anal. Chem.* **2006**, *78*, 726.

(6) Mao, D.; Wucher, A.; Winograd, N. *Anal. Chem.* **2010**, *82*, 57.

(7) Carado, A.; Kozole, J.; Passarelli, M.; Winograd, N.; Loboda, A.; Wingate, J. *Appl. Surf. Sci.* **2008**, *255*, 1610.

(8) Carado, A.; Kozole, J.; Passarelli, M.; Winograd, N.; Loboda, A.; Bunch, J.; Wingate, J.; Hankin, J.; Murphy, R. *Appl. Surf. Sci.* **2008**, *255*, 1572.

(9) Carado, A.; Passarelli, M. K.; Kozole, J.; Wingate, J. E.; Winograd, N.; Loboda, A. V. *Anal. Chem.* **2008**, *80*, 7921.

(10) Passarelli, M. K.; Winograd, N. *Surf. Interface Anal.* **2010**, in press.

(11) Hill, R.; Blenkinsopp, P.; Thompson, S.; Vickerman, J.; Fletcher, J. S. *Surf. Interface Anal.* **2010**, in press.

(12) Rabbani, S.; Fletcher, J. S.; Lockyer, N. P.; Vickerman, J. C. *Surf. Interface Anal.* **2010**, in press.

(13) Fletcher, J. S.; Lockyer, N. P.; Vickerman, J. C. *Surf. Interface Anal.* **2010**, in press.

VITA

Caiyan Lu

Caiyan Lu was born in Zhengzhou, Henan Province, China to Xianying Li and Chuanyin Lu. She attended Nankai University in Tianjin in 1997 and earned a Bachelor of Science degree in Chemistry in 2001 and a Master of Science degree in Analytical Chemistry in 2004. In August of 2004, she began her graduate study in Chemistry at the Pennsylvania State University where she joined the research group of Professor Nicholas Winograd. She studied in the area of analytical chemistry and received her Doctorate of Philosophy in December, 2010.